Mechanical Behavior of Triaxial Woven Fabric (TWF) Composites

Qi Zhao

A Thesis

in

The Department

of

Mechanical & Industrial Engineering

Presented in Partial Fulfilment of the Requirements

for the Degree of Doctor of Philosophy at

Concordia University

Montreal, Quebec, Canada

November 2003

Your file Votre référence
ISBN: 0-612-90406-7
Our file Notre référence
ISBN: 0-612-90406-7

CONCORDIA UNIVERSITY
SCHOOL OF GRADUATE STUDIES

This is to certify that the thesis prepared

By: **Qi Zhao**

Entitled: **Mechanical Behavior of Triaxial Woven Fabric (TWF) Composites**

and submitted in partial fulfillment of the requirements for the degree of

DOCTOR OF PHILOSOPHY (Mechanical Engineering)

complies with the regulations of the University and meets the accepted standards with respect to originality and quality.

Signed by the final examining committee:

Dr. W. Atwood — Chair

Dr. F. Ko — External Examiner

Dr. H.K. Ha — External to Program

Dr. R. Ganesan — Examiner

Dr. M. Pugh — Examiner

Dr. S.V. Hoa — Thesis Supervisor

Approved by Dr. K. Demirli, Graduate Program Director, Mechanical Engineering

MAR 11 2004

Dr. N. Esmail, Dean
Faculty of Engineering & Computer Science

Abstract

Mechanical Behavior of Triaxial Woven Fabric (TWF) Composites

Qi Zhao, Ph.D.

Concordia University, 2003

This study is to explore the mechanical behavior of TWF composites. It covers following five aspects:

- Two finite element models (Superelement 1 and Superelement 2) were developed for prediction of mechanical behavior of TWF composites. Superelement 1 is a 15-node superelement constructed of six identical 8-node 3D isoparametric elements and three identical 4-node 2D isoparametric laminate elements. Superelement 2 is similar to the first element except that this element takes into account the geometric and material properties of the twisted yarns. The assembly is done by the pseudo element technique suggested herein and the static condensation procedure. Superelement 1 can be used for the vibration analysis with some economy of computer space and time. Superelement 2 can be used for detailed stress analysis and for strength prediction. Although these two elements are developed for the TWF composites, they can be applicable for analytical models for other materials and structures made of other types of textile composites.

- A series of experiments were done to obtain the tensile elastic constants of the TWF composites done by another person. Finite element models (Superelement 1 and Superelement 2) developed for the TWF composites were used to provide results for comparison with experiments. The effects of sizes and aspect ratios of TWF panels on their Young's modulus and Poisson's ratio are studied.

- Thermal deformation behavior of TWF composites is modeled using Superelement 2. Thermal deformation behavior and Thermal Expansion Coefficients (TECs) of the TWF composites are evaluated. Effects of the aspect ratios and size of the panels on the TECs are studied.

- The mechanical behavior of a sector of the reflector subjected to uniform pressure is studied by modeling several different-scale sectors using Super-finite elements.

- Progressive failure of TWF composite panels subjected to uni-axial extension is studied numerically and experimentally. TWF panel is discretized respectively using linear and nonlinear Super-Finite-Elements proposed here. Tensor polynomial progressive failure procedure is employed with maximum stress, Hoffman and Tsai-Wu critera. Two displacement-loading cases were considered. The first and ultimate failure loads, maximum extension displacement, locations and modes of failure are estimated and compared well with experimental data.

Acknowledgements

I would like to gratefully express my thanks and appreciation to my thesis supervisor Dr. S. V. Hoa, for his invaluable support and assistance through this study. I am also grateful to him for careful reading and minute criticism of this thesis.

Also, I would like to thank Mr. Paul Ouellette for his work on the experiments.

In particular, the financial support from the Natural Sciences and Engineering Research Council Canada, EMS Technologies, and Canadian Space Agency are appreciated. The technical guidance of personnel at EMS Technologies is also appreciated.

Finally, I wish to express my gratitude to my wife Lei Tian and my daughter Hanqing Zhao for their moral support and understanding.

Table of Contents

List of Figures

List of Tables

List of Symbols

ξ, η, ζ	natural coordinates
x, y, z	element Cartesian coordinates
X_s, Y_s, Z_s	superelement Cartesian coordinates
X_f, Y_f, Z_f	fabric Cartesian coordinates
s, t, r	material principal axes at a point
u, v, w	displacements
σ_{ij}	stresses
ε_{ij}	strains
[q]	stiffness matrix of unidirectional lamina
[Q]	stiffness matrix in element coordinates
[N]	shape function matrix
[M]	mass matrix of finite element
[K]	stiffness matrix of finite element
[T]	transformation matrix
{f}	node force matrix of finite element

$\{d\}$	node displacement matrix of finite element in element coordinates
$\{\bar{d}\}$	node displacement matrix of finite element in superelement coordinates
$\|J\|$	determinant of Jacobian matrix
T_i	component of external force
ρ	mass density
α_{ij}	direction angle of element and superelement coordinates

Chapter 1

Introduction

Textile composites are a class of advanced composites of using textile fabrics (preforms) as reinforcements [1]. They have the potential for improved inter-laminar fracture toughness and impact damage tolerance because of the interlacing. Also, since fiber performs can be fabricated using automated textile equipment, there is the potential for reduced cost. Based on the textile processing techniques, textile composites can be classified as shown in Figure 1.1 [2].

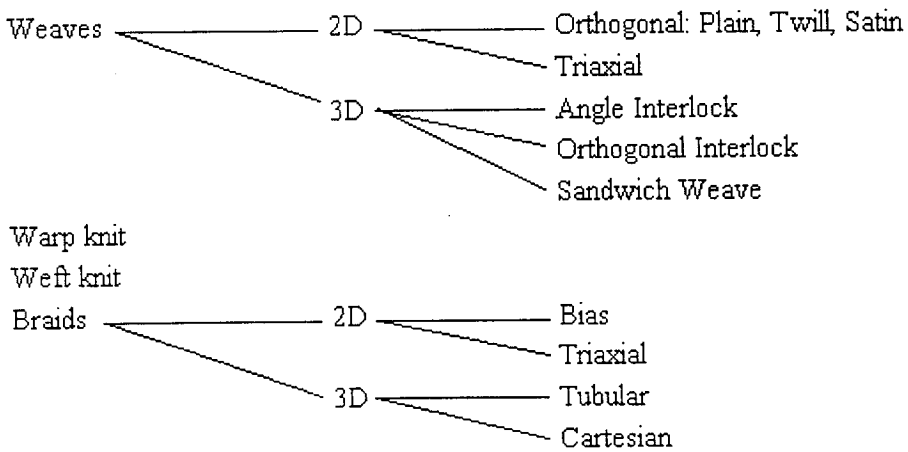

Figure 1.1: Classification of textile composites

Among the different types of textile composites, composites made from Triaxial Woven Fabric (TWF) offer many interesting characteristics. The preform is composed of three sets of yarns, which intersect and interlace with each other at 60^0 angles, shown in Figure 1.2. Due to the presence of the three yarns along these directions, the TWFs have more isotropic responses to both tensile and shear deformations compared with biaxial woven fabrics. In addition, the TWFs are stiffer and easier to handle and have the ability to maintain structural integrity. Therefore, the TWF composites are attractive for many industrial applications.

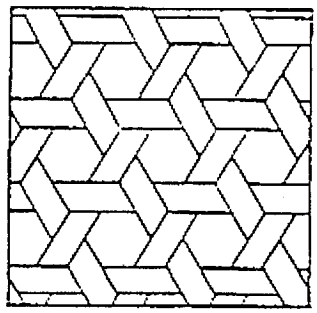

Figure 1.2: Triaxial woven fabric

Laminates made of TWF can consist of many layers of the preform fabric impregnated with resins. In this case, solid laminates can be made and the hole between the yarns as shown in Figure 1.2 are covered. The analysis for this type of laminate may not be much different from that of laminates made up by other types of weaves such as plain weave or satin weaves. There are also applications where only a single layer of the fabric is used to make the laminate, yielding a structure as shown in Figure 1.2. One example application

is the communication satellite. The reason for this construction is due to lightweight, and also due to the facility to allow the air to escape through the holes during launching. This air escape reduces significantly the air impact, which significantly reduces the loading on the structure. Although there is a lot of research work on mechanical behavior of textile composites, this single layer material receives less attention than other textile composites. There is only little research work concerning this material. We know little or even nothing about its thermo-elastic properties and the effects of various parameters (size, aspect ratio and temperature, etc.) on the thermo-elastic properties. It is therefore necessary to study the mechanical behavior of the TWF composites for better application.

Over the past twenty years, many researchers have spent effort in developing models for the prediction of properties of textile composites. A variety of analysis for predicting effective properties and stress distributions of plain weaves has been proposed. The analyses varied both in terms of how faithfully the architecture is modeled and in terms of the assumed variation of the stresses and displacements within the material.

In the 1980s, Ishikawa and Chou presented three analytical 1-D elastic models for the thermo-mechanical modeling of 2-D woven fabric composites [3-8]. These models are known as the mosaic model, the fiber undulation model and the bridging model. The classical lamination theory forms the basic analytical tool for these developments [9]. The mosaic model in Refs [3,4] represents a woven material by an array of rectangular parallelpiped ("brick") elements and ignores the undulated regions of the yarns. The fiber undulation model in Ref. [5] assumes that the material consists of a collection of laminates arranged in series. Fiber undulation is modeled in one direction only. These

models are labeled 1-D models because they only consider the undulation of the yarns in the loading direction. Notice the total absence of any geometric analysis. That is, the actual yarn cross-sectional shape or the presence of a gap between adjacent yarns is not considered. Therefore, no predictions are made for the out-of-plane yarn orientation and the fiber volume fraction. Moreover, these models consider balanced closed weaves only, whereas in practice the fabric can be unbalanced and open. Since the classical laminated plate theory is the basis of each model only the in-plane elastic properties are predicted.

Two-dimensional versions of "modified laminate theory" have been developed by Raju [10], N.Naik, Shembekar & Ganesh [11-13]. These analyses in Refs [10-13] approximate a weave by a collection of cross-ply laminates. However, the fabric geometry was not described adequately. The mechanical properties in the lateral direction (z) could not be correctly modeled. Refs [11-14] propose various methods to obtain the effective properties of this collection of "laminates". Refs [15,16] extend the thermo-elastic models of N. Naik et al to include the prediction of failure in plain weave composites under on-axis static tensile loading. In R.Naik [17], the woven composite was analyzed by discretely modeling each yarn in the unit cell with a flattened lenticular cross-section and sinusoidal undulation at each yarn cross-over point. The 3-dimensional stiffness matrix was computed by discretizing the yarn path into piecewise straight yarn slices and then using a stress averaging technique. Composite strength was calculated by using a beam-on-elastic foundation model for each yarn undulation together with an incremental progressive damage algorithm. However, it is questionable that the calculation of local stress fields in yarn and matrix slices in this strength model is based on the isostrain assumption

Three-dimensional analyses that account for the fiber architecture in a "smeared" fashion have been proposed in Refs [18-20]. These typically do not model the interface between fiber bundles and the matrix pockets with precision. Instead, effective properties at a quadrature point (during numerical integration) are obtained by homogenizing the properties of the materials near the quadrature points. Hahn and Pandy [21] present a thermo-elastic model for non-hybrid plain fabric composites. This model is essentially an extension of the 2-D models of N. Naik. The geometric model accounts for the undulation of warp and weft yarns, the actual yarn cross-section and the presence of a gap between adjacent yarns. The yarn undulations are sinusoidal and described with shape functions. The gap between two neighboring yarns, however, is introduced by terminating the yarn at the start of the gap. Hence, for large gaps the yarn cross-section becomes quasi-rectangular, which is not realistic. Also, this model uses isostrain assumption. The isostrain assumption is not capable of accurately predicting all 3-D elastic constants and of solving stress analysis problem accurately [22].

The correct laminate theory [23-26] considers that the material consists of the union of unidirectional layers whose directions respect the typical axes of real material. Under these conditions, it is possible to apply the traditional laminar theory, which, however, has been corrected with coefficients related to the average value of fiber waving angle; this angle is experimentally determined by using micro-photographs taken on various fabric sections.

The FGM (fiber geometric model) analytical model [27-31] is widely used to foresee composite fabric characteristics. This model considers the fibers and matrix as a group of

rectilinear bars with various spatial orientations. Once the whole group of bars has been characterized, the composite global stiffness matrix, therefore all elastic constants, are obtained by adding the contributions of single bars that should have transverse isotropy. In the calculation of axial stiffness, some errors are found for small braiding angle values.

There is an application procedure that adopts a sub-structuring on material volumes considered homogeneous [32-37]. By using analytical methods such as FGM, volumes having different properties (fiber and matrix) are transformed into an element with homogeneous properties. The solution of the global structure can be obtained through a FEM analysis utilizing single cells as the elements. It is difficult to evaluate the elastic properties with this method, when components have very different elastic moduli.

A variation to the previous method divides the structure into meso-volumes [38-41] and each one of these volumes contains several single cells, the elastic properties of which are calculated through the FGM method. Meso-volume approach gives a more general tool for the analysis of the structures than the approach with single cells. The test pieces that can not be decomposed into single cells may be analyzed. However, the use of this method may cause errors in the global analysis, due to the introduction of sub-elements and fictitious subdivisions.

The approach with macro-elements is based on the use of finite element [42-44]. The finite element formulation implicitly takes into account the composite micro-geometry and the mechanical properties of fiber and matrix, without a precise correspondence with the spatial position of fabric components. This is in contrast with the usual choices to decompose the structure into several elements to have a more precise consideration of

microstructure, or with the choice to use average properties for every element. However, the result is a lower number of elements required for material discretization. This method gives good results in the prediction of fabric global movements and deformation, whereas it is not effective in calculating deformations and tensions inside the elements.

Another numerical approach is called global-local approach with finite elements [45-49]. It makes a distinction between three levels: in one level the structure is assumed homogeneous; in another level micro-structural components appears well differentiated between each other, a different discretization is used according to the degree of homogeneity. The reliability of a method depends on the choice of procedures in discretization at the different levels.

Paumelle, Hassim and Lene [50,51] developed a finite element method for analyzing plain weave fabric composite structures. The periodic medium homogenization method is implemented. Basically, by applying periodic boundary conditions on the surface of the unit cell and by solving six elementary loading conditions on the unit cell, the complete set of elastic moduli of the homogenized structure can be computed. At the same time, the method provides a good approximation of the local distribution of force and stress fields acting in the composite components and at their interface. These microscopic stress fields give a strong indication of the type of damage that will occur. But this approach requires large computer calculation power and memory because of the 3-D nature and the complexity of the yarn architecture. Also, a correct finite element model includes the generation of the fabric geometry and the finite element mesh of nodes and elements. Most of the time spent is related to the creation and the verification of a correct geometric

model [52]. Moreover, there are major problems in analyzing and interpreting the results in a 3-D domain of a rather complex geometry [53].

Blackketter [54] constructed a simplified 3-D unit cell of a single ply non-hybrid plain weave graphite/epoxy composite to model damage propagation in 2-D woven composites. Twenty node isoparametric hexahedron elements were used in generating the finite element meshes. Limits on element refinement were imposed by the computational time required for solution.

Recently, Verpoest and co-workers [55] have used the method of cells to model the microstructures of textile composites. This method examines the different segments of the microstructures of the textile composites. This method is similar to the finite element approach except that cells are used instead of finite elements, which requires a computer program to include the many elements in the unit cell.

In 1993, Fujita, Hamada and Maekawa [56,57] investigated the tensile properties and fracture behavior of carbon fiber TWF composites without open holes using experimentation and FE analysis. In this FE model, beam elements were used to discretize each yarn, and short beam elements of resin were placed at the crossovers to represent the bonding interface between the two interlacing yarns and to assure load transfer from one yarn to the other. In 1999, Dano, Gendron and Picard [58] applied this model to investigate the elastic properties of a carbon fiber TWF composite. However, there are some problems in application of this model, such as how to suitably determine geometric and bending stiffness of the beam. Also, this model is simple and cannot reflect the complex real deformation of the TWF composites.

For triaxial composites, Sheng and Hoa [59,60] proposed an equivalent energy model for the determination of elastic constants. Yong and Hoa [61,62] also proposed an equivalent energy approach for the determination of elastic constants of three-directional braided composites. Xu, Ganesan and Hoa [63] studied the buckling of triaxial composites using nonlinear beam elements.

In conclusion, the current models for 2-D woven fabric composites all have limited applicability, in that either they are not sufficiently accurate to predict the local stress fields in yarn and matrix phases, or they are not computationally efficient. Furthermore, the approaches mentioned above by previous investigations [3-58] were designed to model textile composites without open holes. As such they are not efficient for the case of textile composites. The investigations in [59-63] were mainly averaging techniques that can predict the apparent Young's moduli well. However there is still uncertainty in the prediction for shear values. In addition they cannot determine the stresses required for failure prediction. The response to these needs gave the motivation for this work. The objective of this work is to provide techniques for the accurate determination of elastic properties and stresses within the triaxial composites. For this, special purposed super finite elements were developed. These elements are then used to model the triaxial composite structure subject to different loading conditions.

In this study, mechanical behavior of TWF composites is explored. It covers following five aspects:

Firstly, two finite element models (Superelement 1 and Superelement 2) are developed for prediction of mechanical behavior of TWF composites. Superelement 1 is a 15-node

superelement constructed of six identical 8-node 3D isoparametric elements and three identical 4-node 2D isoparametric laminate elements. Superelement 2 is similar to the first element except that this element takes into account the geometric and material properties of the twisted yarns. The assembly is done by the pseudo element technique suggested herein and the static condensation procedure. The availability of these elements allows for the analysis of complex structures of the triaxial fabric. Superelement 1 can be used for the vibration analysis with some economy of computer space and time. Superelement 2 can be used for detailed stress analysis and for strength prediction. Although these two elements are developed for the TWF composites, they can be applicable for analytical models for other materials and structures made of other types of textile composites [88].

Secondly, a series of experiments were done to obtain the tensile elastic constants of the TWF composites. Finite element models (Superelement 1 and Superelement 2) developed for the TWF composites were also used to provide results for comparison with experiments. The effects of sizes and aspect ratios of TWF panels on their Young's modulus and Poisson's ratio are studied [89].

Thirdly, thermal deformation behavior of TWF composites is modeled using Superelement 2. Thermal deformation behavior and Thermal Expansion Coefficients (TECs) of the TWF composites are evaluated. Effects of the aspect ratios and size of the panels on the TECs are studied [91].

Fourthly, the mechanical behavior of a sector of the reflector subjected to uniform pressure is studied by modeling several different-scale sectors using Super-finite elements [90].

Fifthly, progressive failure of TWF composite panels subjected to uni-axial extension is studied numerically and experimentally. In numerical study, TWF panel is discretized respectively using linear and nonlinear Super-Finite-Elements proposed here. Tensor polynomial progressive failure procedure is employed with maximum stress criterion, Hoffman criterion and Tsai-Wu criterion. Two displacement-loading cases are considered. The first and ultimate failure loads, maximum extension displacement, locations and modes of failure are estimated and compared with experimental data [92].

Chapter 2

Development of finite element models

In this chapter, the development of two super finite elements is presented. Superelement 1 is a 15-node superelement which is composed of two types of elements. The first type, called element E1, is an 8-node 3D isoparametric elements. There are six elements E1 in the superelement 1. The second type, called element E2, is a 4-node 2D-isoparametric laminate elements. There are three elements E2 in the superelement 1. The assembly of these two types of elements (E1 and E2) to make the superelement is done by the pseudo element technique suggested herein and the static condensation procedure.

Superelement 1 does not take the twist in the yarn into consideration. To improve the element connection and to fully consider the characteristics of geometric and material properties of twisted yarn, superelement 2 is developed. Superelement 2 is similar to superelement 1 except that elements E1 are replaced by element E11, which is a 16-node isoparametric 3D elements. Element E11 takes the twist of the yarn into account.

Superelement 1 does not take as much computer space and time and can be used for problems such as vibration study. Superelement 2 takes more computer space and time but can produce more accurate stresses. Detailed development of these elements is shown below.

2.1 Superelement 1

The TWF composite is composed of three sets of yarns, which intersect and interlace with each other at 60^0 angles. As shown in Figure 2.1, the entire fabric can actually be obtained by assembling many unit cells. There are many ways to identify a unit cell in the structure of Figure 2.1. One type of unit cell is shown in Figure 2.2 (a). Repeating the unit cells can reproduce the fabric. Figure 2.2 (b) shows the procedure of reproduction of 4 (unit cell) by 4 (unit cell) fabric. In Figure 2.2 (a), W_1 is the yarn width, W_2 is the larger bridging distance between two yarns, W_3 is the smaller bridging distance (W_3 can be calculated from W_1 and W_2, $W_3 = W_2 - 2\times W_1\tan(\pi/6)$), t_y is the yarn thickness and t_r is the resin layer thickness. These four geometry parameters (W_1, W_2, t_y, and t_r) were measured from the microscopic photograph of the TWF composites. With these four geometry parameters, the geometry of the unit cell can be determined. The volume and weight of the unit cell is also calculated approximately as

$$V_{cell} = 6w_1(w_2 + w_3)t_y/2 + 3w_1^2(2t_y + t_r)/\sin(\pi/3)$$

$$G_{cell} = 6w_1(w_2 + w_3)t_y\rho_y/2 + 3w_1^2(2t_y\rho_y + t_r\rho_r)/\sin(\pi/3)$$

where ρ_y is the density of the yarn of TWF composites and ρ_r is the density of the resin.

This unit cell is also used as a superelement in the finite element development. Close examination of figure 2.2 shows that there are two types of structures in the unit cell. One type of structure has only one yarn thickness (labeled E1 in the figure) and the other type

has two-yarn thickness (labeled E2). Finite element E1 is developed to model the structure with one yarn thickness and element E2 is developed to model the two-yarn thickness structure. There are six of E1 elements, and three of E2 elements in the unit cell (superelement). The E2 structure has three layers. The top and bottom layers consist of yarn materials. The orientation of the fibers in the top tow is different from the orientation of fibers in the bottom tow. In between the top and bottom yarns is the matrix material. As can be seen from the cross section view of the unit cell, structure E1 changes elevation as it bridges the two structures E2. Note also that due to the trapezoidal shape of E1, there is a twist in the yarn in E1 (Figure 2.3). Element E1 will involve composite lamina characteristics. Element E2 will be developed based on the general layerwise laminate theory [64,65] and has the ability to solve for interlaminar stresses and for boundary stress distribution with consideration of transverse deformation. The suitable displacement fields will be assumed in element E2 which can fully describe the real stress fields in composite laminated plate, i.e., stress fields associated with thickness direction are allowed to be discontinuous between laminae.

The superelement 1 is developed by assembling the six elements E1 and the three elements E2. These superelements are then assembled to make the structure of the triaxial composites. As can be seen, the TWF composite will have complex stress and deformation status because of the weaving structure and material anisotropic characteristics. Even when the TWF composite is subjected to pure tension, the yarn will bear a combination of tensile, compression, shear, bending and torsion. The pure and torsion shear will exist at the crossing areas between yarns and will play an important

role in fabric failure. The above-mentioned factors will have to be taken into account in the development of finite element model.

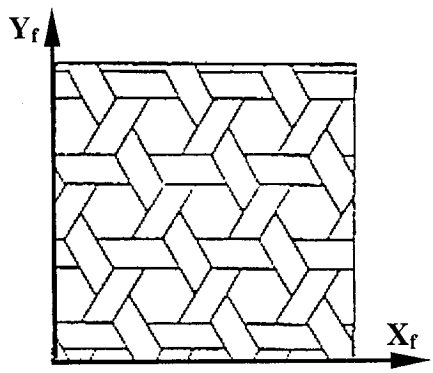

Figure 2.1: Triaxial woven fabric

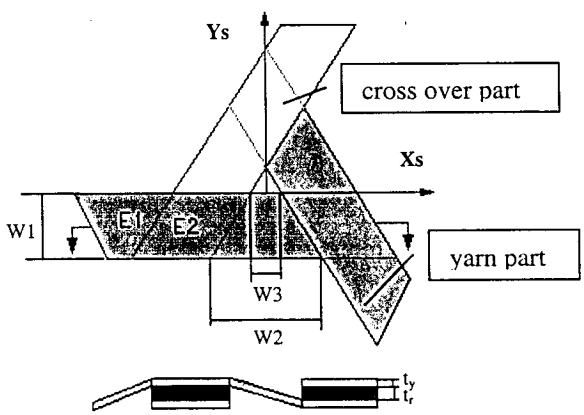

Figure 2.2 (a): A unit cell (superelement)

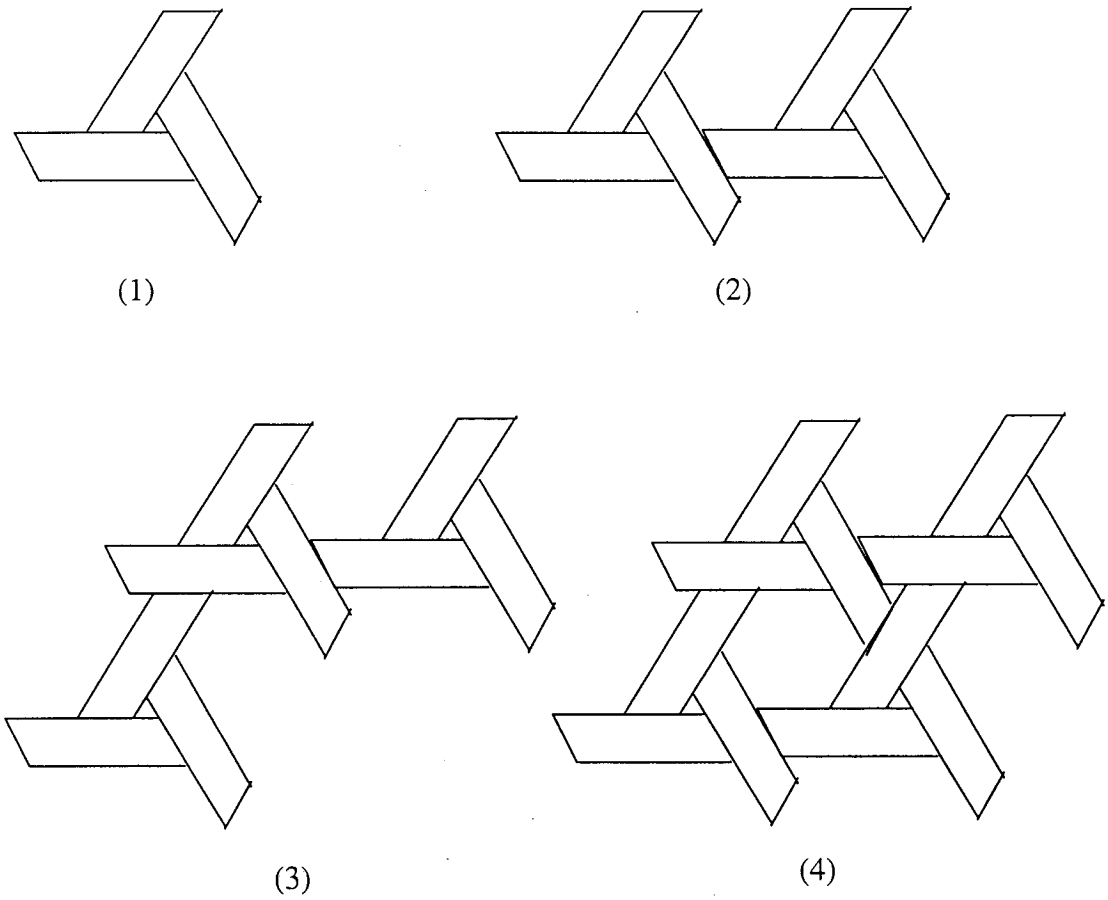

Figure 2.2 (b): Repeating unit cells into a fabric

2.1.1 Element E1

Before stating the development of element E1, the geometry of the single yarn (tow) part is firstly analyzed. The yarn part is bridging between the top layer of one crossover part to the bottom layer of another crossover part. Referring to Figure 2.3, the elevation difference between points 5 and 6 is the same as the elevation difference between points 8 and 7. However, since the length of the element segment 56 is shorter than the length of

element segment 78, the angle of elevation α is greater than the angle of elevation β. As such, the top and bottom surfaces of the element shown in Figure 2.3 are not flat. Rather they are curves, indicating the twist that exists in the element. For the development of element E1, this twist is neglected for simplification.

The material properties of the single yarn part vary at different points of the part. The stress-strain relations in common Cartesian coordinate system x,y,z (Figure 2.3) can be written as:

$$\sigma_{ij} = Q_{ijkl}(x,y,z)\varepsilon_{kl}, \quad (i,j,k,l = x,y,z)$$

An approximation is required to obtain the material properties for the single yarn part. The yarn part can be considered as to consist of many same-thickness strips along the y direction and that are parallel to xz plane. In each strip the fibers are parallel to the top and bottom lines of this strip, analogous to an unidirectional lamina. The orientation of the fibers can be different from one strip to another. However, since the rate of twist (α-β) of the yarn part is small, the value of Q_{ijkl} approaches closely that of q_{ijkl} which is evaluated at the strip (y=0) of yarn part. Therefore, as a first approximation, we have $Q_{ijkl} = q_{ijkl}$.

With Q_{ijkl} simplified as above, an 8-node 3D isoparametric element is applied directly on the yarn part, the procedure of which can be seen below.

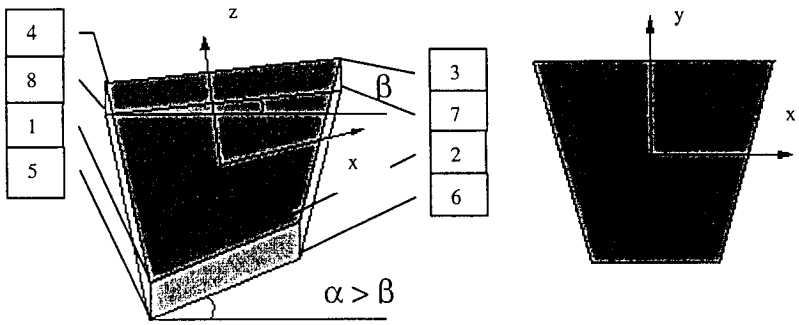

Figure 2.3: Geometry and coordinate of yarn part

The displacement field and geometry of the element are given respectively by

$$\begin{Bmatrix} u \\ v \\ w \end{Bmatrix} = \sum_{i=1}^{8} N_i(\xi,\eta,\zeta) \begin{Bmatrix} u_i \\ v_i \\ w_i \end{Bmatrix} = [N]\{d_{el}\} \tag{2.1.1}$$

$$\begin{Bmatrix} x \\ y \\ z \end{Bmatrix} = \sum_{i=1}^{8} N_i(\xi,\eta,\zeta) \begin{Bmatrix} x_i \\ y_i \\ z_i \end{Bmatrix} \tag{2.1.2}$$

where ξ, η and ζ are natural coordinates. The shape functions in terms of the natural coordinates are

$$N_i(\xi,\eta,\zeta) = \frac{1}{8}(1+\xi\xi_i)(1+\eta\eta_i)(1+\zeta\zeta_i), \quad (i = 1,2,\cdots,8) \tag{2.1.3}$$

And u_i, v_i and w_i are nodal displacements of node i in the element Cartesian coordinate system. The number of nodes is shown in Figure 2.3. Nodal displacement vector is

$$\{d_{el}\} = [\ u_1, u_2, u_3, u_4, v_1, v_2, v_3, v_4, w_1, w_2, w_3, w_4, u_5, u_6, u_7, u_8, v_5, v_6, v_7, v_8, w_5, w_6, w_7, w_8\ ]^T \tag{2.1.4}$$

The strain-displacement relations can be expressed as

$$\begin{Bmatrix} \varepsilon_{xx} \\ \varepsilon_{yy} \\ \varepsilon_{zz} \\ \varepsilon_{yz} \\ \varepsilon_{xz} \\ \varepsilon_{xy} \end{Bmatrix} = \begin{Bmatrix} u_{,x} \\ v_{,y} \\ w_{,z} \\ v_{,z} + w_{,y} \\ u_{,z} + w_{,x} \\ u_{,y} + v_{,x} \end{Bmatrix} = [B]\{d_{el}\} \tag{2.1.5}$$

The equilibrium equations are derived using the principle of virtual displacements in the absence of body forces as:

$$\int_{Ve} \sigma_{ij}\delta\varepsilon_{ij}dv = \int_{Se} T_i\delta u_i ds - \int_{Ve} \rho\ddot{u}_i\delta u_i dv \qquad (i, j = x, y, z) \tag{2.1.6}$$

Substitution of Eq. (2.1.1) and Eq. (2.1.5) into Eq.(2.1.6) yields,

$$\left(\int_{-1}^{1}\int_{-1}^{1}\int_{-1}^{1} \rho[N]^T[N]|J|d\xi d\eta d\zeta\right)\{\ddot{d}_{el}\} + \left(\int_{-1}^{1}\int_{-1}^{1}\int_{-1}^{1} [B]^T[Q][B]|J|d\xi d\eta d\zeta\right)\{d_{el}\} = \left(\int_{Se} [N]^T \begin{Bmatrix} T_1 \\ T_2 \\ T_3 \end{Bmatrix} ds\right) \tag{2.1.7}$$

Eq. (2.1.7) is written in short form as

$$[M_{el}]\{\ddot{d}_{el}\} + [K_{el}]\{d_{el}\} = \{f_{el}\} \tag{2.1.8}$$

where

$$[M_{el}]=\left(\int_{-1}^{1}\int_{-1}^{1}\int_{-1}^{1}\rho[N]^T[N]|J|d\xi d\eta d\zeta\right)$$

$$[K_{el}]=\left(\int_{-1}^{1}\int_{-1}^{1}\int_{-1}^{1}[B]^T[Q][B]|J|d\xi d\eta d\zeta\right)$$

$$\{f_{el}\}=\left(\int_{Se}[N]^T\begin{Bmatrix}T_1\\T_2\\T_3\end{Bmatrix}ds\right)$$

and ρ is the mass density of the yarn. T_i is the component of external force. $|J|$ is the determinant of Jacobian matrix as follows

$$|J|=\begin{vmatrix}x_{,\xi} & x_{,\eta} & x_{,\zeta}\\ y_{,\xi} & y_{,\eta} & y_{,\zeta}\\ z_{,\xi} & z_{,\eta} & z_{,\zeta}\end{vmatrix}$$

Before assembling into the superelement, Eq.(2.1.8) needs to be transformed into an equation in the superelement coordinate system $OX_sY_sZ_s$. The transformation matrix can be sought as follows. Assume that the direction angles of element coordinates xyz and superelement coordinates $X_sY_sZ_s$ can be expressed as

$$[\alpha_{ij}]=\begin{bmatrix}\cos^{-1}(\bar{x}_0\cdot\bar{X}_{s0}) & \cos^{-1}(\bar{x}_0\cdot\bar{Y}_{s0}) & \cos^{-1}(\bar{x}_0\cdot\bar{Z}_{s0})\\ \cos^{-1}(\bar{y}_0\cdot\bar{X}_{s0}) & \cos^{-1}(\bar{y}_0\cdot\bar{Y}_{s0}) & \cos^{-1}(\bar{y}_0\cdot\bar{Z}_{s0})\\ \cos^{-1}(\bar{z}_0\cdot\bar{X}_{s0}) & \cos^{-1}(\bar{z}_0\cdot\bar{Y}_{s0}) & \cos^{-1}(\bar{z}_0\cdot\bar{Z}_{s0})\end{bmatrix} \qquad (2.1.9)$$

where $\bar{X}_{s0} = (1,0,0)$, $\bar{Y}_{s0} = (0,1,0)$ and $\bar{Z}_{s0} = (0,0,1)$ are the unit vectors of superelement coordinates. $\bar{x}_0, \bar{y}_0$ and $\bar{z}_0$ are the unit vectors of element coordinates. They all are expressed in the axes of the superelement coordinate system.

We can easily obtain transformation of nodal displacements in two coordinate systems

$$\{d_{e1}\} = [T_{e1}]\{\bar{d}_{e1}\} = \begin{bmatrix} [T_e] & 0 \\ 0 & [T_e] \end{bmatrix} \{\bar{d}_{e1}\} \tag{2.1.10}$$

where $\{\bar{d}_{e1}\}$ represents node displacement vector in the superelement coordinate system.

$$[T_e] = \begin{bmatrix} [C_{11}] & [C_{12}] & [C_{13}] \\ [C_{21}] & [C_{22}] & [C_{23}] \\ [C_{31}] & [C_{32}] & [C_{33}] \end{bmatrix}$$

$$[C_{ij}] = \begin{bmatrix} \cos(\alpha_{ij}) & 0 & 0 & 0 \\ 0 & \cos(\alpha_{ij}) & 0 & 0 \\ 0 & 0 & \cos(\alpha_{ij}) & 0 \\ 0 & 0 & 0 & \cos(\alpha_{ij}) \end{bmatrix}$$

Using Eq. (2.1.10), the FE equation of element E1 in superelement coordinate system can be obtained as

$$([T_{e1}]^T [M_{e1}][T_{e1}])\{\ddot{\bar{d}}_{e1}\} + ([T_{e1}]^T [K_{e1}][T_{e1}])\{\bar{d}_{e1}\} = [T_{e1}]^T \{f_{e1}\} \tag{2.1.11}$$

2.1.2 Element E2

The crossover part is the 3 layers laminate with internal resin layer. A 4-node 2D-

isoparametric laminated element of 3 layers is applied for crossover parts. This element is a 3D element. 2D-isoparametric refers to 2D-isoparametric technique used in xy plane integration of finite element formula, see Eqs (2.1.23). There are 12 DOFs at each node, numbering of which is shown in Figure 2.4. The internal layer is an isotropic resin layer that can be used to simulate the relation between yarns at crossovers. Formulae of element E2 are derived using the general layer-wise laminate theory by Reddy [64,65]. This theory accounts for a desired degree of approximation of the displacements through the laminate thickness, allowing for piecewise representation of displacements through individual laminae and allowing for possible discontinuities in the slopes of the deflections at the interfaces of two individual laminae [66-70]. Since the displacements are expressed in this theory as product of functions of variables x and y and functions of variable z (see Eqs (2.1.12)), the 3D integration of elastic energy can be changed into product of 1D integration and 2D integration. That can reduce calculation greatly in numerical integration. The formulae of 4-node 2D-isoparametric laminated element are derived below.

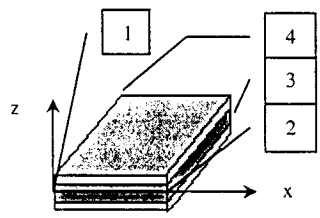

Figure 2.4: Geometry and coordinate of crossover part

Assuming that displacement field has following forms

$$\begin{aligned} u_x(x,y,z) &= U_j(x,y)\Phi_j(z) \\ u_y(x,y,z) &= V_j(x,y)\Phi_j(z) \qquad (j=1,2,3,4) \\ u_z(x,y,z) &= W_j(x,y)\Phi_j(z) \end{aligned} \tag{2.1.12}$$

where the tensor summation convention is used here and in following derivation. Repeating indices implies summation. $\Phi_j(z)$ are linear global interpolation functions associated with the jth node along thickness and are given by

$$\Phi_j(z) = \begin{cases} \varphi_2^{(j-1)}(z) = (z - z_{j-1})/(z_j - z_{j-1}), & z_{j-1} \le z \le z_j \\ \varphi_1^{(j)}(z) = (z - z_{j+1})/(z_j - z_{j+1}), & z_j \le z \le z_{j+1} \end{cases} \tag{2.1.13}$$

where $\varphi_m^{(k)}$ are local linear Lagrange interpolation functions associated with node m of the kth layer.

The strain-displacement relations and constitutive equations are given respectively by

$$\varepsilon_{ij} = \frac{1}{2}(u_{i,j} + u_{j,i}) \tag{2.1.14}$$

$$\sigma_{ij} = Q_{ijkl}\varepsilon_{kl} \tag{2.1.15}$$

where subscript ',' denotes the derivative with respect to x_j.

The equilibrium equations are derived using the principle of virtual displacements

$$\int_{Ve} \sigma_{ij}\delta\varepsilon_{ij}dv = \int_{Se} T_i\delta u_i ds - \int_{Ve} \rho\ddot{u}_i\delta u_i dv \qquad (i,j = x,y,z) \tag{2.1.16}$$

Substitution of Eqs (2.1.14) and (2.1.15) into Eq (2.1.16) leads to

$$\int_{Ve}\frac{1}{2}\sigma_{ij}\delta(u_{i,j}+u_{j,i})dv=\int_{Se}T_i\delta u_i ds-\int_{Ve}\rho\ddot{u}_i\delta u_i dv \qquad (i,j=x,y,z)\ (2.1.17)$$

Substituting Eq. (2.1.12) into Eq. (2.1.17) leads to long and complex equations. One term, as an example, is derived as follows.

$$\int_{Ve}\sigma_{xx}\delta u_{x,x}dv=\int_{Ve}\sigma_{xx}\delta\left(\frac{\partial U_j(x,y)}{\partial x}\Phi_j(z)\right)dv=\int_{Ve}\sigma_{xx}\frac{\partial\delta U_j(x,y)}{\partial x}\Phi_j(z)dv$$

$$=\int_{\Omega e}\frac{\partial\delta U_j(x,y)}{\partial x}\left(\int_{-h/2}^{h/2}\sigma_{xx}\Phi_j(z)dz\right)d\Omega=\int_{\Omega e}\frac{\partial\delta U_j(x,y)}{\partial x}\left(\sum_{t=1}^{3}\int_{z_t}^{z_{t+1}}\sigma_{xx}\Phi_j(z)dz\right)d\Omega=\int_{\Omega e}\frac{\partial\delta U_j(x,y)}{\partial x}N_{xx}^{j}d\Omega$$

In the above, t denotes the layer number. Z_t (t=1,2,3) is z coordinate between layers.

To aid in the presentation of the governing equation (2.1.17), the following are defined:

$$I^{jm}=\sum_{t=1}^{3}\left[\int_{z_t}^{z_{t+1}}(\rho\Phi_j\Phi_m)dz\right]$$

$$N_{kl}^{j}=\sum_{t=1}^{3}\left[\int_{z_t}^{z_{t+1}}(\sigma_{kl}\Phi_j)dz\right] \qquad (2.1.18)$$

$$\tilde{N}_{kl}^{j}=\sum_{t=1}^{3}\left[\int_{z_t}^{z_{t+1}}\left(\sigma_{kl}\frac{\partial\Phi_j}{\partial z}\right)dz\right]$$

Substituting Eqs. (2.1.12), (2.1.14) and (2.1.15) into Eqs. (2.1.17) yields

$$N_{kl}^{j} = A_{klxx}^{jm}\frac{\partial U_m}{\partial x} + A_{klyy}^{jm}\frac{\partial V_m}{\partial y} + B_{klzz}^{jm}W_m + B_{klyz}^{jm}V_m + A_{klyz}^{jm}\frac{\partial W_m}{\partial y} +$$
$$B_{klxz}^{jm}U_m + A_{klxz}^{jm}\frac{\partial W_m}{\partial x} + A_{klxy}^{jm}\frac{\partial U_m}{\partial y} + A_{klxy}^{jm}\frac{\partial V_m}{\partial x}$$
$$\tilde{N}_{kl}^{j} = C_{klxx}^{jm}\frac{\partial U_m}{\partial x} + C_{klyy}^{jm}\frac{\partial V_m}{\partial y} + D_{klzz}^{jm}W_m + D_{klyz}^{jm}V_m + C_{klyz}^{jm}\frac{\partial W_m}{\partial y} + \qquad (2.1.19)$$
$$D_{klxz}^{jm}U_m + C_{klxz}^{jm}\frac{\partial W_m}{\partial x} + C_{klxy}^{jm}\frac{\partial U_m}{\partial y} + C_{klxy}^{jm}\frac{\partial V_m}{\partial x}$$

where

$$A_{klrs}^{jm} = \sum_{t=1}^{3}\left[\int_{z_t}^{z_{t+1}}\left(Q_{klrs}^{(t)}\Phi_j\Phi_m\right)dz\right]$$

$$B_{klrs}^{jm} = \sum_{t=1}^{3}\left[\int_{z_s}^{z_{t+1}}\left(Q_{klrs}^{(t)}\Phi_j\frac{d\Phi_m}{dz}\right)dz\right]$$

$$C_{klrs}^{jm} = \sum_{t=1}^{3}\left[\int_{z_t}^{z_{t+1}}\left(Q_{klrs}^{(t)}\frac{d\Phi_j}{dz}\Phi_m\right)dz\right]$$

$$D_{klrs}^{jm} = \sum_{t=1}^{3}\left[\int_{z_t}^{z_{t+1}}\left(Q_{klrs}^{(t)}\frac{d\Phi_j}{dz}\frac{d\Phi_m}{dz}\right)dz\right] \qquad (2.1.20)$$

where j,m=1,2,3,4, and k, l, r, s = x, y, z

Substitution of Eq (2.1.12) into Eq (2.1.17), followed by integration with respect to the thickness coordinate z, yields

$$
\begin{aligned}
&\int_{\Omega e}\left[I^{jm}\ddot{U}_m\delta U_j + I^{jm}\ddot{V}_m\delta V_j + I^{jm}\ddot{W}_m\delta W_j\right]d\Omega + \\
&\int_{\Omega e}\left[\, N^j_{xx}\frac{\partial\delta U_j}{\partial x} + N^j_{yy}\frac{\partial\delta V_j}{\partial y} + N^j_{zz}\frac{\partial\delta W_j}{\partial z} + \left(\tilde{N}^j_{yz}\delta V_j + N^j_{yz}\frac{\partial\delta W_j}{\partial y}\right)\right. \\
&\left. + \left(\tilde{N}^j_{xz}\delta U_j + N^j_{xz}\frac{\partial\delta W_j}{\partial x}\right) + \left(N^j_{xy}\frac{\partial\delta U_j}{\partial y} + N^j_{xy}\frac{\partial\delta V_j}{\partial x}\right)\right]d\Omega \\
&= \int_{Su}\left[T_1\Phi_j\delta U_j + T_2\Phi_j\delta V_j + T_3\Phi_j\delta W_j\right]dS
\end{aligned}
\tag{2.1.21}
$$

where Ω_e represents the 2D projection of element E2 onto the xy plane shown in Figure 2.4.

Substituting Eq. (2.1.19) into Eq. (2.1.21) yields

$$
\begin{aligned}
&\sum_{j=1}^{4}\sum_{m=1}^{4}\int_{\Omega e}\left[\delta U_j \quad \delta V_j \quad \delta W_j\right]\begin{Bmatrix} I^{jm}\ddot{U}_m \\ I^{jm}\ddot{V}_m \\ I^{jm}\ddot{W}_m \end{Bmatrix}d\Omega + \sum_{j=1}^{4}\sum_{m=1}^{4}\int_{\Omega e}\left(\delta\{\overline{U}_j\}\right)^T\left[H^{jm}\right]\{\overline{U}_m\}d\Omega \\
&\qquad = \sum_{j=1}^{4}\int_{Su}\left[\delta U_j \quad \delta V_j \quad \delta W_j\right]\begin{Bmatrix} T_1\Phi_j \\ T_2\Phi_j \\ T_3\Phi_j \end{Bmatrix}d\Omega
\end{aligned}
\tag{2.1.22}
$$

where

$$
\left[H^{jm}\right] = \begin{bmatrix}
A^{jm}_{xxxx} & A^{jm}_{xxyy} & B^{jm}_{xxzz} & B^{jm}_{xxyz} & A^{jm}_{xxyz} & B^{jm}_{xxxz} & A^{jm}_{xxxz} & A^{jm}_{xxxy} & A^{jm}_{xxxy} \\
A^{jm}_{yyxx} & A^{jm}_{yyyy} & B^{jm}_{yyzz} & B^{jm}_{yyyz} & A^{jm}_{yyyz} & B^{jm}_{yyxz} & A^{jm}_{yyxz} & A^{jm}_{yyxy} & A^{jm}_{yyxy} \\
C^{jm}_{zzxx} & C^{jm}_{zzyy} & D^{jm}_{zzzz} & D^{jm}_{zzyz} & C^{jm}_{zzyz} & D^{jm}_{zzxz} & C^{jm}_{zzxz} & C^{jm}_{zzxy} & C^{jm}_{zzxy} \\
C^{jm}_{yzxx} & C^{jm}_{yzyy} & D^{jm}_{yzzz} & D^{jm}_{yzyz} & C^{jm}_{yzyz} & D^{jm}_{yzxz} & C^{jm}_{yzxz} & C^{jm}_{yzxy} & C^{jm}_{yzxy} \\
A^{jm}_{yzxx} & A^{jm}_{yzyy} & B^{jm}_{yzzz} & B^{jm}_{yzyz} & A^{jm}_{yzyz} & B^{jm}_{yzxz} & A^{jm}_{yzxz} & A^{jm}_{yzxy} & A^{jm}_{yzxy} \\
C^{jm}_{xzxx} & C^{jm}_{xzyy} & D^{jm}_{xzzz} & D^{jm}_{xzyz} & C^{jm}_{xzyz} & D^{jm}_{xzxz} & C^{jm}_{xzxz} & C^{jm}_{xzxy} & C^{jm}_{xzxy} \\
A^{jm}_{xzxx} & A^{jm}_{xzyy} & B^{jm}_{xzzz} & B^{jm}_{xzyz} & A^{jm}_{xzyz} & B^{jm}_{xzxz} & A^{jm}_{xzxz} & A^{jm}_{xzxy} & A^{jm}_{xzxy} \\
A^{jm}_{xyxx} & A^{jm}_{xyyy} & B^{jm}_{xyzz} & B^{jm}_{xyyz} & A^{jm}_{xyyz} & B^{jm}_{xyxz} & A^{jm}_{xyxz} & A^{jm}_{xyxy} & A^{jm}_{xyxy} \\
A^{jm}_{xyxx} & A^{jm}_{xyyy} & B^{jm}_{xyzz} & B^{jm}_{xyyz} & A^{jm}_{xyyz} & B^{jm}_{xyxz} & A^{jm}_{xyxz} & A^{jm}_{xyxy} & A^{jm}_{xyxy}
\end{bmatrix}
$$

$$\{\overline{U}_j\}=\left[\frac{\partial U_j}{\partial x},\frac{\partial V_j}{\partial y},W_j,V_j,\frac{\partial W_j}{\partial y},U_j,\frac{\partial W_j}{\partial x},\frac{\partial U_j}{\partial y},\frac{\partial V_j}{\partial x}\right]^T$$

Since element E2 is a parallel quadrilateral, 2D isoparametric element technique is applied to produce shape functions. Let

$$\begin{aligned} U_j &= S^i(\xi,\eta)u_j^i \\ V_j &= S^i(\xi,\eta)v_j^i \qquad (i=1,2,3,4) \\ W_j &= S^i(\xi,\eta)w_j^i \end{aligned} \tag{2.1.23}$$

$$\begin{aligned} x &= S^i(\xi,\eta)x^i \\ y &= S^i(\xi,\eta)y^i \end{aligned} \tag{2.1.24}$$

where $S^i(\xi,\eta)$ are shape functions. I is the node number of element E2, j the layer number. (x^i,y^i) denotes the coordinates of node I in the coordinate system of element E2.

Let

$$\{\overline{V}_j\}=[U_j,V_j,W_j]^T \tag{2.1.25}$$

$$\{\Delta_j\}=[u_j^1,u_j^2,u_j^3,u_j^4,v_j^1,v_j^2,v_j^3,v_j^4,w_j^1,w_j^2,w_j^3,w_j^4]^T \tag{2.1.26}$$

Using Eqs. (2.1.23 to 2.1.26) leads to

$$\{\overline{U}_j\}=[S]\{\Delta_j\} \tag{2.1.27}$$

$$\{\overline{V}_j\}=[R]\{\Delta_j\} \tag{2.1.28}$$

where

$$[S]=\begin{bmatrix} \frac{\partial S^1}{\partial x} & \frac{\partial S^2}{\partial x} & \frac{\partial S^3}{\partial x} & \frac{\partial S^4}{\partial x} & 0 & 0 & 0 & 0 & 0 & 0 & 0 & 0 \\ 0 & 0 & 0 & 0 & \frac{\partial S^1}{\partial y} & \frac{\partial S^2}{\partial y} & \frac{\partial S^3}{\partial y} & \frac{\partial S^4}{\partial y} & 0 & 0 & 0 & 0 \\ 0 & 0 & 0 & 0 & 0 & 0 & 0 & 0 & S^1 & S^2 & S^3 & S^4 \\ 0 & 0 & 0 & 0 & S^1 & S^2 & S^3 & S^4 & 0 & 0 & 0 & 0 \\ 0 & 0 & 0 & 0 & 0 & 0 & 0 & 0 & \frac{\partial S^1}{\partial y} & \frac{\partial S^2}{\partial y} & \frac{\partial S^3}{\partial y} & \frac{\partial S^4}{\partial y} \\ S^1 & S^2 & S^3 & S^4 & 0 & 0 & 0 & 0 & 0 & 0 & 0 & 0 \\ 0 & 0 & 0 & 0 & 0 & 0 & 0 & 0 & \frac{\partial S^1}{\partial x} & \frac{\partial S^2}{\partial x} & \frac{\partial S^3}{\partial x} & \frac{\partial S^4}{\partial x} \\ \frac{\partial S^1}{\partial y} & \frac{\partial S^2}{\partial y} & \frac{\partial S^3}{\partial y} & \frac{\partial S^4}{\partial y} & 0 & 0 & 0 & 0 & 0 & 0 & 0 & 0 \\ 0 & 0 & 0 & 0 & \frac{\partial S^1}{\partial x} & \frac{\partial S^2}{\partial x} & \frac{\partial S^3}{\partial x} & \frac{\partial S^4}{\partial x} & 0 & 0 & 0 & 0 \end{bmatrix}$$

$$[R]=\begin{bmatrix} S^1 & S^2 & S^3 & S^4 & 0 & 0 & 0 & 0 & 0 & 0 & 0 & 0 \\ 0 & 0 & 0 & 0 & S^1 & S^2 & S^3 & S^4 & 0 & 0 & 0 & 0 \\ 0 & 0 & 0 & 0 & 0 & 0 & 0 & 0 & S^1 & S^2 & S^3 & S^4 \end{bmatrix}$$

Finally, Eq. (2.1.22) can be expressed as the following matrix form

$$\left(\int_{-1}^{1}\int_{-1}^{1}\begin{bmatrix} [R]^T[I^{11}][R] & [R]^T[I^{12}][R] & [R]^T[I^{13}][R] & [R]^T[I^{14}][R] \\ & [R]^T[I^{22}][R] & [R]^T[I^{23}][R] & [R]^T[I^{24}][R] \\ & & [R]^T[I^{33}][R] & [R]^T[I^{34}][R] \\ \text{Symmetric} & & & [R]^T[I^{44}][R] \end{bmatrix}|J|d\xi d\eta\right)\begin{Bmatrix} \ddot{\Delta}_1 \\ \ddot{\Delta}_2 \\ \ddot{\Delta}_3 \\ \ddot{\Delta}_4 \end{Bmatrix}+$$

$$\left(\int_{-1}^{1}\int_{-1}^{1}\begin{bmatrix} [S]^T[H^{11}][S] & [S]^T[H^{12}][S] & [S]^T[H^{13}][S] & [S]^T[H^{14}][S] \\ & [S]^T[H^{22}][S] & [S]^T[H^{23}][S] & [S]^T[H^{24}][S] \\ & & [S]^T[H^{33}][S] & [S]^T[H^{34}][S] \\ \text{Symmetric} & & & [S]^T[H^{44}][S] \end{bmatrix}|J|d\xi d\eta\right)\begin{Bmatrix} \Delta_1 \\ \Delta_2 \\ \Delta_3 \\ \Delta_4 \end{Bmatrix} \quad (2.1.29)$$

$$=\left(\int_{Su}\begin{Bmatrix} [R]^T\{F_1\} \\ [R]^T\{F_2\} \\ [R]^T\{F_3\} \\ [R]^T\{F_4\} \end{Bmatrix}ds\right)$$

where $[I^{ij}] = \begin{bmatrix} I^{ij} & 0 & 0 \\ 0 & I^{ij} & 0 \\ 0 & 0 & I^{ij} \end{bmatrix}$

Eq. (2.1.29) can be written in short form as

$$[M_{e2}]\{\ddot{d}_{e2}\} + [K_{e2}]\{d_{e2}\} = \{f_{e2}\} \tag{2.1.30}$$

where

$$[M_{e2}] = \left(\int_{-1}^{1}\int_{-1}^{1} \begin{bmatrix} [R]^T[I^{11}][R] & [R]^T[I^{12}][R] & [R]^T[I^{13}][R] & [R]^T[I^{14}][R] \\ & [R]^T[I^{22}][R] & [R]^T[I^{23}][R] & [R]^T[I^{24}][R] \\ & & [R]^T[I^{33}][R] & [R]^T[I^{34}][R] \\ \textit{Symmetric} & & & [R]^T[I^{44}][R] \end{bmatrix} |J| d\xi d\eta \right)$$

$$[K_{e2}] = \left(\int_{-1}^{1}\int_{-1}^{1} \begin{bmatrix} [S]^T[H^{11}][S] & [S]^T[H^{12}][S] & [S]^T[H^{13}][S] & [S]^T[H^{14}][S] \\ & [S]^T[H^{22}][S] & [S]^T[H^{23}][S] & [S]^T[H^{24}][S] \\ & & [S]^T[H^{33}][S] & [S]^T[H^{34}][S] \\ \text{Symmetric} & & & [S]^T[H^{44}][S] \end{bmatrix} |J| d\xi d\eta \right)$$

$$\{f_{e2}\} = \left(\int_{Su} \begin{Bmatrix} [R]^T\{F_1\} \\ [R]^T\{F_2\} \\ [R]^T\{F_3\} \\ [R]^T\{F_4\} \end{Bmatrix} ds \right)$$

And $\{F_i\} = [T_i\Phi_j, T_2\Phi_j, T_3\Phi_j]^T$. T_i (I = 1, 2, 3) is component of external force. $|J|$ is the determinant of 2D Jacobian matrix as follows

$$|J| = \begin{vmatrix} x_{,\xi} & x_{,\eta} \\ y_{,\xi} & y_{,\eta} \end{vmatrix}$$

In the same way as element E1, before assembling to superelement, we need to seek the transformation matrix to transform Eq.(2.1.30) into an equation in the superelement coordinate system $OX_sY_sZ_s$. Assume that the direction angles of element coordinates xyz and superelement coordinates $X_sY_sZ_s$ can be given by

$$[\alpha_{ij}]=\begin{bmatrix}\cos^{-1}(\bar{x}_0\cdot\bar{X}_{s0}) & \cos^{-1}(\bar{x}_0\cdot\bar{Y}_{s0}) & \cos^{-1}(\bar{x}_0\cdot\bar{Z}_{s0})\\ \cos^{-1}(\bar{y}_0\cdot\bar{X}_{s0}) & \cos^{-1}(\bar{y}_0\cdot\bar{Y}_{s0}) & \cos^{-1}(\bar{y}_0\cdot\bar{Z}_{s0})\\ \cos^{-1}(\bar{z}_0\cdot\bar{X}_{s0}) & \cos^{-1}(\bar{z}_0\cdot\bar{Y}_{s0}) & \cos^{-1}(\bar{z}_0\cdot\bar{Z}_{s0})\end{bmatrix} \tag{2.1.31}$$

where $\bar{X}_{s0}=(1,0,0)$, $\bar{Y}_{s0}=(0,1,0)$ and $\bar{Z}_{s0}=(0,0,1)$ are the unit vectors of superelement coordinates. $\bar{x}_0, \bar{y}_0$ and $\bar{z}_0$ are the unit vectors of element coordinates.

Transformation of node displacements under two coordinate systems can be given by

$$\{d_{e2}\}=[T_{e2}]\{\bar{d}_{e2}\}=\begin{bmatrix}[T_e] & 0 & 0 & 0\\ 0 & [T_e] & 0 & 0\\ 0 & 0 & [T_e] & 0\\ 0 & 0 & 0 & [T_e]\end{bmatrix}\{\bar{d}_{e2}\} \tag{2.1.32}$$

where $\{\bar{d}_{e2}\}$ represents node displacements in the superelement coordinate systems.

$$[T_e]=\begin{bmatrix}[C_{11}] & [C_{12}] & [C_{13}]\\ [C_{21}] & [C_{22}] & [C_{23}]\\ [C_{31}] & [C_{32}] & [C_{33}]\end{bmatrix}$$

$$[C_{ij}]=\begin{bmatrix}\cos(\alpha_{ij}) & 0 & 0 & 0\\ 0 & \cos(\alpha_{ij}) & 0 & 0\\ 0 & 0 & \cos(\alpha_{ij}) & 0\\ 0 & 0 & 0 & \cos(\alpha_{ij})\end{bmatrix}$$

Finally, the FE equation of element E2 under $OX_sY_sZ_s$ can be given using Eq.(2.1.32) by

$$([T_{e2}]^T[M_{e2}][T_{e2}])\{\ddot{\bar{d}}_{e2}\}+([T_{e2}]^T[K_{e2}][T_{e2}])\{\bar{d}_{e2}\}=[T_{e2}]^T\{f_{e2}\} \tag{2.1.33}$$

Before assembly to a superelement, for convenience to assemble, the DOFs of each node will be grouped together. The DOFs order of Eq.(2.2.22) will be arranged according to the following

$$\hat{d}_{e2}=[\nabla^1,\ \nabla^2,\ \nabla^3,\ \nabla^4]^T \tag{2.1.34}$$

where $\nabla^i=[u_1^i,u_2^i,u_3^i,u_4^i,v_1^i,v_2^i,v_3^i,v_4^i,w_1^i,w_2^i,w_3^i,w_4^i]$. ∇^i is the DOFs vector of node i.

Element E2 built using the general layer-wise laminate theory is really a 3D laminate element. It can be thought of as a combination of 3 overlapped 8-node 3D linear elements with 3 DOFs at each node, as shown in Figure 2.5. 4 nodes distributed along the thickness direction at a corner of the overlapped elements are viewed as a node of element E2. In this way, the 3 overlapped elements can form an element E2 with 4 imaging nodes, 12 DOFs at each node.

In this assembly procedure, the use of the imaginary node helps in facilitating the the assembly of the elements within the plane of the structure (i.e., without having to take into account the nodes in the third direction during the assembly process).

The above assembly procedure, however, does not produce any economy in the numerical calculation. This is because in order to determine the stiffness matrix for the element, full integration for the 3 directions has to be done. In order to reduce the amount

of numerical integration, layer-wise procedure as proposed by Reddy [64,65] is used. In this procedure, the shape function is assumed to be a product of two functions: f(x,y) and g(z). By this separation, the integration effect is reduced significantly.

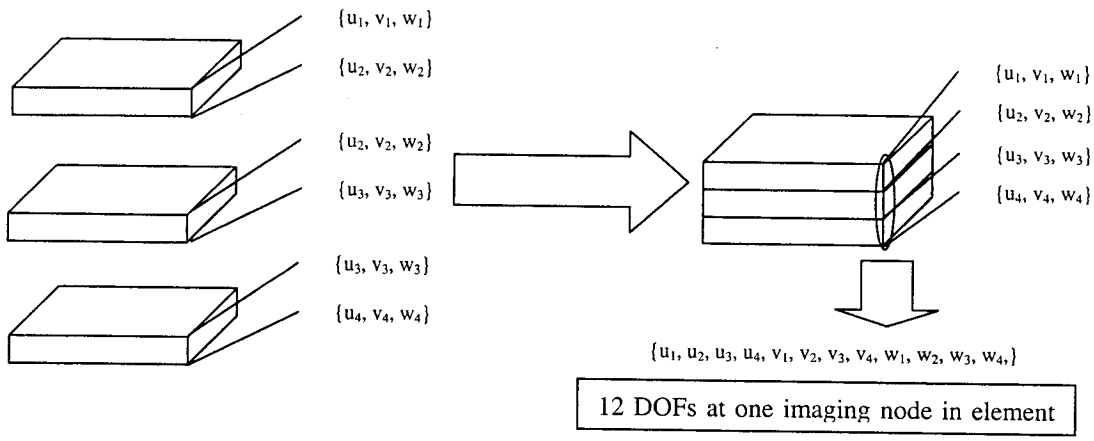

Figure 2.5: Combination of 3 overlapped 8-node linear elements into E2

2.1.3 Assemblage of elements into superelement

As stated before, element E1 is an 8-node 3D element with 3 DOFs of each node (u,v,w), and element E2 is a 4-node 2D-isoparametric laminated element with 12 DOFs of each node. How are they assembled into a superelement? The pseudo element technique is presented herein for the assemblage of elements. First of all, E1 element will be expanded into a pseudo element like element E2 by artificially adding pseudo DOFs and by rearranging all the DOFs of E1. Figure 2.6 shows element E1 in an imaginary box that looks like element E2. The element in this figure is similar to the element in Figure 2.4 if the empty space is included. This modified element E1 is called the pseudo element. The

nodes of this element are called the pseudo nodes and the degrees of freedom (DOFs) of this element are called the pseudo DOFs.

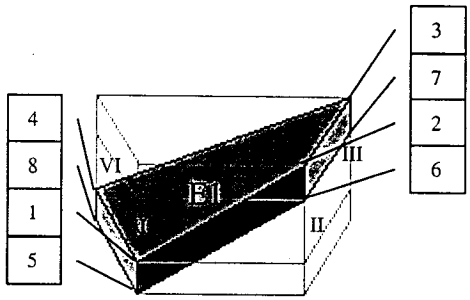

Figure 2.6: Pseudo element

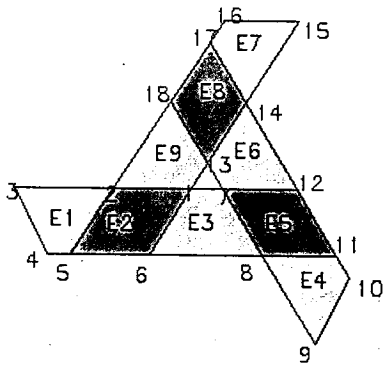

Figure 2.7: Assemblage of elements

The following is an example of how to add the pseudo DOFs to form the pseudo node 1 of pseudo element. Refer to equation (2.1.34) for element E2. Along the same sequence shown in Equation (2.1.34), the sequence of the DOFs at node i of the pseudo element E1 can be written as: $[0, 0, u_1, u_5, 0, 0, v_1, v_5, 0, 0, w_1, w_5]^T$ where 0 represents pseudo DOF. Similarly for node II of the pseudo element, the sequence of DOFs can be written as: $[u_2, u_6, 0, 0, v_2, v_6, 0, 0, w_2, w_6, 0, 0]$. According to this way, stiffness matrix of element E1

is expanded. The elements at rows and columns in expanded stiffness matrix and load vector of pseudo element corresponding to the pseudo DOFs are placed with zeros. They have following form.

$$\begin{bmatrix}
0 & 0 & 0 & 0 & 0 & 0 & 0 & 0 & 0 & 0 & 0 & 0 & \cdots \\
0 & 0 & 0 & 0 & 0 & 0 & 0 & 0 & 0 & 0 & 0 & 0 & \cdots \\
0 & 0 & k_{1,1} & k_{1,13} & 0 & 0 & k_{1,5} & k_{1,17} & 0 & 0 & k_{1,9} & k_{1,21} & \cdots \\
0 & 0 & k_{13,1} & k_{13,13} & 0 & 0 & k_{13,5} & k_{13,17} & 0 & 0 & k_{13,9} & k_{13,21} & \cdots \\
0 & 0 & 0 & 0 & 0 & 0 & 0 & 0 & 0 & 0 & 0 & 0 & \cdots \\
0 & 0 & 0 & 0 & 0 & 0 & 0 & 0 & 0 & 0 & 0 & 0 & \cdots \\
0 & 0 & k_{5,1} & k_{5,13} & 0 & 0 & k_{5,5} & k_{5,17} & 0 & 0 & k_{5,9} & k_{5,21} & \cdots \\
0 & 0 & k_{17,1} & k_{17,13} & 0 & 0 & k_{17,5} & k_{17,17} & 0 & 0 & k_{17,9} & k_{17,21} & \cdots \\
0 & 0 & 0 & 0 & 0 & 0 & 0 & 0 & 0 & 0 & 0 & 0 & \cdots \\
0 & 0 & 0 & 0 & 0 & 0 & 0 & 0 & 0 & 0 & 0 & 0 & \cdots \\
0 & 0 & k_{9,1} & k_{9,13} & 0 & 0 & k_{9,5} & k_{9,17} & 0 & 0 & k_{9,9} & k_{9,21} & \cdots \\
0 & 0 & k_{21,1} & k_{21,13} & 0 & 0 & k_{21,5} & k_{21,17} & 0 & 0 & k_{21,9} & k_{21,21} & \cdots \\
\vdots & \vdots & \vdots & \vdots & \vdots & \vdots & \vdots & \vdots & \vdots & \vdots & \vdots & \vdots & \cdots
\end{bmatrix}
\begin{Bmatrix}
0 \\ 0 \\ u_1 \\ u_5 \\ 0 \\ 0 \\ v_1 \\ v_5 \\ 0 \\ 0 \\ w_1 \\ w_5 \\ \vdots
\end{Bmatrix}
=
\begin{Bmatrix}
0 \\ 0 \\ f_1 \\ f_{13} \\ 0 \\ 0 \\ f_5 \\ f_{17} \\ 0 \\ 0 \\ f_9 \\ f_{21} \\ \vdots
\end{Bmatrix}$$

where details on stiffness matrix of element E1 can be referred in the DOFs order of Eq. (2.1.4).

As such, this pseudo element has 4 nodes with 12 DOFs at each node like E2 element. The pseudo variables will correspond to zero stiffness. Secondly, the superelement can be thought of as being constructed of one kind of element E2 and the assemblage is conducted according to the usual assembling method with the element and node number shown in Figure 2.7. In addition, there is another advantage in this method, replacing 3D node numbering by 2D node numbering in assemblage of superelements into the TWF composites. This will greatly reduce the work and the complexity of FE assemblage procedure.

After the assemblage, the superelement has 18 nodes with 12 DOFs at each node and has a sum of 216 DOFs, 36 DOFs of which are pseudo DOFs located at nodes 3,4,9,10,15 and 16.

Note that pseudo DOFs on boundaries of the TWF composites will lead to singularity of stiffness matrix and must be removed before solution. Pseudo DOFs within the TWF composites are not a concern because they will disappear automatically after assemblage.

2.1.4 Condensation of DOFs within superelement

In Figure 2.7, nodes 1, 7 and 13 are located within the superelement. The DOFs on these internal nodes are not coupled with the DOFs of other superelements after assemblage into the TWF composites. These internal DOFs should be condensed to make the superelement model more efficient. In this study, the 36 DOFs on internal nodes 1,7 and 13 can be eliminated by the static condensation procedure [71] as follows:

Let the equations $[K]\{d\}=\{f\}$ represent the superelement equations. The DOFs $\{d\}$ can be partitioned so that $\{d\}=[d_r \;\; d_c]^T$, where $\{d_r\}$ are boundary DOFs to be retained and $\{d_c\}$ are internal DOFs to be eliminated by condensation. Thus $[K]\{d\}=\{f\}$ becomes

$$\begin{bmatrix} k_{rr} & k_{rc} \\ k_{cr} & k_{cc} \end{bmatrix} \begin{Bmatrix} d_r \\ d_c \end{Bmatrix} = \begin{Bmatrix} f_r \\ f_c \end{Bmatrix} \tag{2.1.35}$$

The lower partition is solved for $\{d_c\}$

$$\{d_c\} = -[k_{cc}]^{-1}([k_{cr}]\{d_r\} - \{f_c\}) \tag{2.1.36}$$

Next, $\{d_c\}$ is substituted into the upper partition of Eqs. (2.1.35). Thus

$$\underbrace{([k_{rr}]-[k_{rc}][k_{cc}]^{-1}[k_{cr}])}_{\text{condensed } [k]}\{d_r\}=\underbrace{\{f_r\}-[k_{rc}][k_{cc}]^{-1}[f_c]}_{\text{condensed } \{f\}} \tag{2.1.37}$$

The superelement is now treated in standard fashion; that is, the condensed [k] and the condensed {f} are assembled into the structure, boundary conditions are imposed, and structural DOFs {D} are computed. Thus $\{d_r\}$ becomes known, and $\{d_c\}$ follows from Eq. (2.1.36).

Finally, Superelement 1 becomes a 15-node superelement with 12 DOFs of each node.

2.2 Superelement 2

As stated in section 2.1, the yarn part is a twisted lamina and has complex geometric and material properties. In Superelement 1, as a first approximation, the yarn part is simply modeled by an 8-node 3D isoparametric element (named E1) with the average modulus Q_{ijkl}. Obviously, this model has some difference from the real yarn part. First, the connection between E1 and E2 forms an angle and easily leads to stress concentration. Second, since there are different material properties at different points on the twisted yarn part, the average modulus used in Superelement 1 can also result in some errors. Hence it is necessary to improve Superelement 1 and to develop a new FE model.

In Superelement 2, to take into account the twisted characteristics of the yarn part, a 16-node 3D isoparametric element (named E11) is developed for the yarn part to improve

the connection. The material properties at any point of yarn part are formulated by space projection technique and used in element E11. Hence this model can reflect more truly the characteristics of the geometry and material properties of the yarn part and give more accurate results.

2.2.1 Transformation of coordinates at any point on a single yarn part

Since the single yarn part is a twisted unidirectional lamina, its material properties vary at different points of the yarn part. Hence it is necessary to set up constitutive equations of the yarn part before deriving FE formulas of element E11.

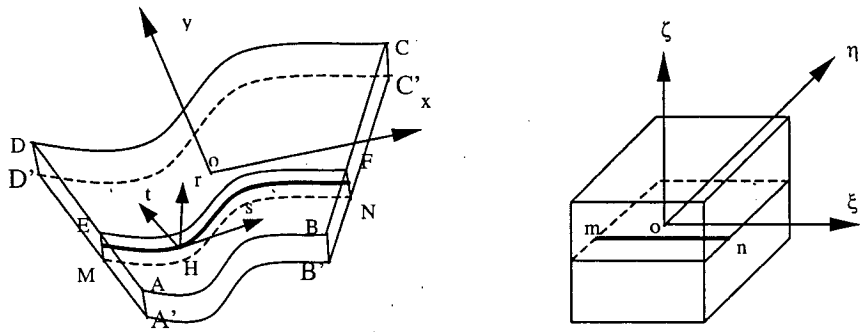

(a) Yarn part (E11)

(b) Unit cube

Figure 2.8: Projection of unit cube into yarn part

Assume that a single yarn part can be obtained by projection of a unit cube in space Oξη ζ into space oxyz, as shown in Figure 2.8. The geometry of the yarn part can be described using the following equations

$$
\begin{aligned}
x &= x(\xi,\eta,\zeta) \\
x &= y(\xi,\eta,\zeta) \\
z &= z(\xi,\eta,\zeta)
\end{aligned}
\tag{2.2.1}
$$

With the coordinates of 16 nodes shown in Figures 2.9 and the shape functions of Eqs (2.2.9), above equations are easily set up using Eq. (2.2.7). Naturally, the curved mid-plane of the yarn part can be formed from projection of the mid-plane $\xi\eta$ of the cube (ζ =0) and expressed by

$$
\begin{aligned}
x &= x(\xi,\eta,\zeta = 0) \\
y &= y(\xi,\eta,\zeta = 0) \\
z &= z(\xi,\eta,\zeta = 0)
\end{aligned}
\tag{2.2.2}
$$

For a lamina, one of its material principal axes is along fiber direction and the other two lie in the cross section of the lamina perpendicular to the fiber direction. The orientation of the material principal axes at each point of the lamina is same. For the yarn part, it is a twisted lamina in the TWF composites and its mid-plane is a trapezoid curved plane. Hence the orientation of its material principal axes is different at each point of the yarn part. That leads to the fact that there are different material properties at different points of the yarn part.

Consider the material principal axes s, t and r of point H on the mid-plane, shown in Figure 2.8 (a). Axis s coincides with the tangent of the fiber MN at point H. Axis r is normal to the mid-plane at point H and axis t can be determined from axes s and r, using the right hand rule. Since the width of the yarn part is basically same, front and rear planes AA'BB' and CC'DD' can be thought of as being parallel. So the fiber MN

through point H would lie in a cross-section plane EE'FF' through point H, which is parallel to two side planes AA'BB' and CC'DD'. That means that the line mn (Figure 2.8 (b)) mapped into fiber MN (Figure 2.8 (a)) is parallel with natural axis ξ. Accordingly, the material principal axes s, t, r at point H on the mid-plane can be given as follows:

Two tangent vectors of mid-plane of the yarn part at point H along natural axes ξ, η

$$\begin{aligned} \bar{a}_\xi &= (x_{,\xi}(\zeta = 0), y_{,\xi}(\zeta = 0), z_{,\xi}(\zeta = 0)) \\ \bar{b}_\eta &= (x_{,\eta}(\zeta = 0), y_{,\eta}(\zeta = 0), z_{,\eta}(\zeta = 0)) \end{aligned} \tag{2.2.3}$$

Note that $\bar{a}_\xi$ and $\bar{b}_\eta$ are not perpendicular to each other.

Unit vector of axis s : $\bar{s}_0 = \dfrac{\bar{s}}{|\bar{s}|}, \qquad \bar{s} = \bar{a}_\xi$

Unit vector of axis r :

$$\bar{r}_0 = \frac{\bar{r}}{|\bar{r}|}, \qquad \bar{r} = \bar{a}_\xi \times \bar{b}_\eta = \begin{vmatrix} \bar{i} & \bar{j} & \bar{k} \\ a_{\xi 1} & a_{\xi 2} & a_{\xi 3} \\ b_{\eta 1} & b_{\eta 2} & b_{\eta 3} \end{vmatrix}$$

Unit vector of axis t :

$$\bar{t}_0 = \frac{\bar{t}}{|\bar{t}|}, \qquad \bar{t} = \bar{r} \times \bar{s} = \begin{vmatrix} \bar{i} & \bar{j} & \bar{k} \\ r_1 & r_2 & r_3 \\ s_1 & s_2 & s_3 \end{vmatrix}$$

With the material principal axes s, t, r of point H, the direction angles of axes (s, t, r) of point H and element coordinate axes (x, y, z) can be determined by

$$[\alpha_{ij}] = \begin{bmatrix} \cos^{-1}(\bar{s}_0 \cdot \bar{x}_0) & \cos^{-1}(\bar{s}_0 \cdot \bar{y}_0) & \cos^{-1}(\bar{s}_0 \cdot \bar{z}_0) \\ \cos^{-1}(\bar{t}_0 \cdot \bar{x}_0) & \cos^{-1}(\bar{t}_0 \cdot \bar{y}_0) & \cos^{-1}(\bar{t}_0 \cdot \bar{z}_0) \\ \cos^{-1}(\bar{r}_0 \cdot \bar{x}_0) & \cos^{-1}(\bar{r}_0 \cdot \bar{y}_0) & \cos^{-1}(\bar{r}_0 \cdot \bar{z}_0) \end{bmatrix} \tag{2.2.4}$$

where unit vectors of axes x,y,z are denoted by

$$\bar{x}_0 = (1 \quad 0 \quad 0), \quad \bar{y}_0 = (0 \quad 1 \quad 0), \quad \bar{z}_0 = (0 \quad 0 \quad 1)$$

Strain transformation matrix between these two coordinate systems can be written as

$$\{\varepsilon_{str}\} = [T]\{\varepsilon_{xyz}\}$$

$$[T] = \begin{bmatrix} c_{11}^2 & c_{12}^2 & c_{13}^2 & c_{12}c_{13} & c_{11}c_{13} & c_{11}c_{12} \\ c_{21}^2 & c_{22}^2 & c_{23}^2 & c_{22}c_{23} & c_{21}c_{23} & c_{21}c_{22} \\ c_{31}^2 & c_{32}^2 & c_{33}^2 & c_{32}c_{33} & c_{31}c_{33} & c_{31}c_{32} \\ 2c_{21}c_{31} & 2c_{22}c_{32} & 2c_{23}c_{33} & (c_{22}c_{33}+c_{23}c_{32}) & (c_{21}c_{33}+c_{23}c_{31}) & (c_{21}c_{32}+c_{22}c_{31}) \\ 2c_{11}c_{31} & 2c_{12}c_{32} & 2c_{13}c_{33} & (c_{12}c_{33}+c_{13}c_{32}) & (c_{11}c_{33}+c_{13}c_{31}) & (c_{11}c_{32}+c_{12}c_{31}) \\ 2c_{11}c_{21} & 2c_{12}c_{22} & 2c_{13}c_{23} & (c_{12}c_{23}+c_{13}c_{22}) & (c_{11}c_{23}+c_{13}c_{21}) & (c_{11}c_{22}+c_{12}c_{21}) \end{bmatrix}$$

where $c_{ij} = \cos(\alpha_{ij})$.

Finally, 6 by 6 constitutive matrix at point H in element coordinates oxyz can be obtained as

$$[Q] = [T]^T[q][T] \tag{2.2.5}$$

where [q] is the constitutive matrix of unidirectional lamina made up from the yarn. It should be noted that [q] remains the same from point to point in the twisted yarn, whereas [Q] changes from point to point. The determination of [Q] can be done at as many points

as one wishes. However, for the numerical solution here, the determination of [Q] is done at the Gauss integration points.

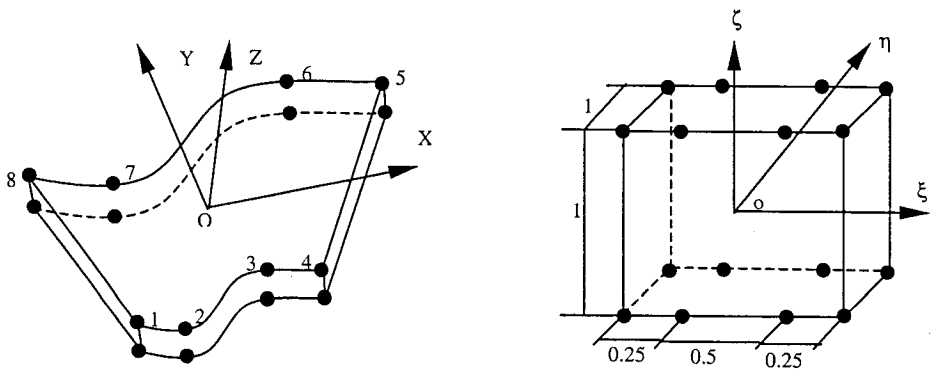

(a) Yarn part (E11) (b) Unit cube

Figure 2.9: Projection of unit cube into yarn part

2.2.2 Element E11

With [Q] from equation (2.2.5), a 16-node 3D isoparametric element is set up for the yarn part, as shown in Figure 2.9. Details about its formulas can be seen below.

The displacement field and geometry of the element are given respectively by

$$\begin{Bmatrix} u \\ v \\ w \end{Bmatrix} = \sum_{i=1}^{16} N_i(\xi,\eta,\zeta) \begin{Bmatrix} u_i \\ v_i \\ w_i \end{Bmatrix} = [N]\{d\} \tag{2.2.6}$$

$$\begin{Bmatrix} x \\ y \\ z \end{Bmatrix} = \sum_{i=1}^{16} N_i(\xi,\eta,\zeta) \begin{Bmatrix} x_i \\ y_i \\ z_i \end{Bmatrix} \tag{2.2.7}$$

where ξ, η and ζ are natural coordinates. u_i, v_i, and w_i are nodal displacements of node i in the element Cartesian coordinate system. The number of nodes is shown in Figure 2.9 (a).

$$\{d\} = [u_1, v_1, w_1, u_2, v_2, w_2, \cdots\cdots, u_{16}, v_{16}, w_{16}]^T \tag{2.2.8}$$

The shape functions in terms of the natural coordinates are given by

$$N_1(\xi,\eta,\zeta) = \frac{1}{6}(\xi+\frac{1}{2})(\xi-\frac{1}{2})(\xi-1)(\eta-1)(\zeta+1)$$

$$N_2(\xi,\eta,\zeta) = -\frac{1}{3}(\xi+1)(\xi-\frac{1}{2})(\xi-1)(\eta-1)(\zeta+1)$$

$$N_3(\xi,\eta,\zeta) = \frac{1}{3}(\xi+1)(\xi+\frac{1}{2})(\xi-1)(\eta-1)(\zeta+1)$$

$$N_4(\xi,\eta,\zeta) = -\frac{1}{6}(\xi+1)(\xi+\frac{1}{2})(\xi-\frac{1}{2})(\eta-1)(\zeta+1)$$

$$N_9(\xi,\eta,\zeta) = -\frac{1}{6}(\xi+\frac{1}{2})(\xi-\frac{1}{2})(\xi-1)(\eta-1)(\zeta-1)$$

$$N_{10}(\xi,\eta,\zeta) = \frac{1}{3}(\xi+1)(\xi-\frac{1}{2})(\xi-1)(\eta-1)(\zeta-1)$$

$$N_{11}(\xi,\eta,\zeta) = -\frac{1}{3}(\xi+1)(\xi+\frac{1}{2})(\xi-1)(\eta-1)(\zeta-1)$$

$$N_{12}(\xi,\eta,\zeta) = \frac{1}{6}(\xi+1)(\xi+\frac{1}{2})(\xi-\frac{1}{2})(\eta-1)(\zeta-1)$$

$$N_8(\xi,\eta,\zeta) = -\frac{1}{6}(\xi+\frac{1}{2})(\xi-\frac{1}{2})(\xi-1)(\eta+1)(\zeta+1)$$

$$N_7(\xi,\eta,\zeta) = \frac{1}{3}(\xi+1)(\xi-\frac{1}{2})(\xi-1)(\eta+1)(\zeta+1)$$

$$N_6(\xi,\eta,\zeta) = -\frac{1}{3}(\xi+1)(\xi+\frac{1}{2})(\xi-1)(\eta+1)(\zeta+1)$$

$$N_5(\xi,\eta,\zeta) = \frac{1}{6}(\xi+1)(\xi+\frac{1}{2})(\xi-\frac{1}{2})(\eta+1)(\zeta+1)$$

$$
\begin{aligned}
N_{16}(\xi,\eta,\zeta) &= \frac{1}{6}(\xi+\frac{1}{2})(\xi-\frac{1}{2})(\xi-1)(\eta+1)(\zeta-1) \\
N_{15}(\xi,\eta,\zeta) &= -\frac{1}{3}(\xi+1)(\xi-\frac{1}{2})(\xi-1)(\eta+1)(\zeta-1) \\
N_{14}(\xi,\eta,\zeta) &= \frac{1}{3}(\xi+1)(\xi+\frac{1}{2})(\xi-1)(\eta+1)(\zeta-1) \\
N_{13}(\xi,\eta,\zeta) &= -\frac{1}{6}(\xi+1)(\xi+\frac{1}{2})(\xi-\frac{1}{2})(\eta+1)(\zeta-1)
\end{aligned}
\tag{2.2.9}
$$

and (x_i, y_i, z_i) are coordinates of node i in the element coordinate system. The coordinates of node 1, 4, 5, 8, 9, 12, 13 and 16 are obtained easily in terms of superelement geometric parameters, shown in Figures 2.9 (a) and 2.2. The coordinates of node 2, 3, 6, 7, 10,11,14 and 15 can be obtained using following procedure. The coordinates of node 2, 3 should be chosen so as to make curve 1234 become a segment of the curve of sine function **sin(t)** $(-\pi/4 \leq t \leq \pi/4)$ and to make curve 1234 tangent to corresponding lines at the connection nodes with element E2, as shown in Figure 2.10. The coordinates of other nodes can be determined in the same way.

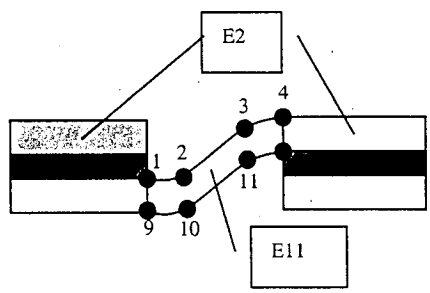

Figure 2.10: Connection of E11 and E2

The strain-displacement relations are given by

$$\begin{Bmatrix} \varepsilon_{xx} \\ \varepsilon_{yy} \\ \varepsilon_{zz} \\ \varepsilon_{yz} \\ \varepsilon_{xz} \\ \varepsilon_{xy} \end{Bmatrix} = \begin{Bmatrix} u_{,x} \\ v_{,y} \\ w_{,z} \\ v_{,z} + w_{,y} \\ u_{,z} + w_{,x} \\ u_{,y} + v_{,x} \end{Bmatrix} = [B]\{d\} \tag{2.2.10}$$

The equilibrium equations are derived using the principle of virtual displacements in the absence of body forces and specified tractions

$$\int_{Ve} \sigma_{ij}\delta\varepsilon_{ij}dv = \int_{Se} T_i\delta u_i ds - \int_{Ve} \rho\ddot{u}_i\delta u_i dv \qquad (i,j = x,y,z) \tag{2.2.11}$$

Substitution of Eq. (2.2.6) into Eq.(2.2.10) and (2.2.11) yields,

$$\left(\int_{-1-1-1}^{1\,1\,1}\int \rho[N]^T[N]|J|d\xi d\eta d\zeta\right)\{\ddot{d}\} + \left(\int_{-1-1-1}^{1\,1\,1}\int \rho[B]^T[Q][B]|J|d\xi d\eta d\zeta\right)\{d\} = \left(\int_{Se}[N]^T\begin{Bmatrix} T_1 \\ T_2 \\ T_3 \end{Bmatrix} ds\right) \tag{2.2.12}$$

Eq. (2.2.12) can be written in short form

$$[M_{el}]\{\ddot{d}_{el}\} + [K_{el}]\{d_{el}\} = \{f_{el}\} \tag{2.2.13}$$

where T_i is component of external force. $|J|$ is the determinant of Jacobian matrix as before.

Before assembling into superelement, Eq.(2.2.13) should also be transformed into the equation in superelement coordinate system $OX_sY_sZ_s$. Assume that the direction angles of element and superelement coordinate systems can be given by

$$[\alpha_{ij}]=\begin{bmatrix}\cos^{-1}(\bar{x}_0\cdot\bar{X}_{s0}) & \cos^{-1}(\bar{x}_0\cdot\bar{Y}_{s0}) & \cos^{-1}(\bar{x}_0\cdot\bar{Z}_{s0})\\ \cos^{-1}(\bar{y}_0\cdot\bar{X}_{s0}) & \cos^{-1}(\bar{y}_0\cdot\bar{Y}_{s0}) & \cos^{-1}(\bar{y}_0\cdot\bar{Z}_{s0})\\ \cos^{-1}(\bar{z}_0\cdot\bar{X}_{s0}) & \cos^{-1}(\bar{z}_0\cdot\bar{Y}_{s0}) & \cos^{-1}(\bar{z}_0\cdot\bar{Z}_{s0})\end{bmatrix} \tag{2.2.14}$$

where $\bar{X}_{s0}=(1,0,0)$, $\bar{Y}_{s0}=(0,1,0)$ and $\bar{Z}_{s0}=(0,0,1)$ are the unit vectors of superelement coordinates. $\bar{x}_0,\bar{y}_0$ and $\bar{z}_0$ are the unit vectors of element coordinates.

Transformation of node displacements in two coordinate systems is given by

$$\{d_{e1}\}=[T_{e1}]\{\bar{d}_{e1}\}=\text{diagon}[[C]]_{48\times48}\{\bar{d}_{e1}\} \tag{2.2.15}$$

where $\{\bar{d}_{e1}\}$ represents node displacements under superelement coordinate systems.

$$[C]=\begin{bmatrix}\cos(\alpha_{11}) & \cos(\alpha_{12}) & \cos(\alpha_{13})\\ \cos(\alpha_{21}) & \cos(\alpha_{22}) & \cos(\alpha_{23})\\ \cos(\alpha_{31}) & \cos(\alpha_{32}) & \cos(\alpha_{33})\end{bmatrix}$$

Using Eq. (2.2.15), the FE equation of element E11 under superelement coordinate system can be given by

$$([T_{e1}]^T[M_{e1}][T_{e1}])\{\ddot{\bar{d}}_{e1}\}+([T_{e1}]^T[K_{e1}][T_{e1}])\{\bar{d}_{e1}\}=[T_{e1}]^T\{f_{e1}\} \tag{2.2.15}$$

2.2.3 Assemblage of elements into superelement and DOFs condensation

Six 16-node 3D isoparametric elements E11 and three 4-node 2D-isoparametric laminated elements E2 will be assembled to a superelement (Superelement 2) by the pseudo element technique. As we know, element E2 has 4 nodes, each of which has 12

DOFs, arranged in following order, [u_1, u_2, u_3, u_4, v_1, v_2, v_3, v_4, w_1, w_2, w_3, w_4]. Element E11 has 16 nodes, each of which has 3 DOFs in following order, [u_1, v_1, w_1] for node 1. We shall now apply the concept of the pseudo element technique. The DOFs of E11 will be arranged in new order to make E11 be 8-node pseudo element, each node has 12 DOFs, 6 DOFs of which are pseudo DOFs that are added in the same order as the node numbering in element E2. Of the 8 nodes, 4 are at the corners and the other 4 are on the sides of the element. For example, in element E11, node 1 has following DOFs, [0, 0, u_1, u_9, 0, 0, v_1, v_9, 0, 0, w_1, w_9]. For node 4, we have [u_4, u_{12}, 0, 0, v_4, v_{12}, 0, 0, w_4, w_{12}, 0, 0]. For node 5, we have [u_5, u_{13}, 0, 0, v_5, v_{13}, 0, 0, w_5, w_{13}, 0, 0], and for node 8, we have [0, 0, u_8, u_{16}, 0, 0, v_8, v_{16}, 0, 0, w_8, w_{16}] etc. So the stiffness matrix of element E11 is expanded from 48 by 48 matrix to 96 by 96 matrix. Therefore, in assemblage of superelement, node numbering can be performed in 2 dimensions and elements E11 and E2 can be easily assembled into a superelement.

After assemblage, this superelement has 42 nodes and 504 DOFs, shown in Figure 2.11. However some nodes or DOFs can be removed by condensation technique. Nodes within superelement, 1, 2, 3, 15, 16, 17, 29, 30, 31, and nodes on boundary of element E11, 5, 6, 9, 10, 13, 14, 19, 20, 23, 24, 27, 28, 33, 34, 37, 38, 41, 42, have nothing to do with connection with other elements. Therefore, above 27 nodes or 324 DOFs were eliminated by the static condensation procedure as stated before. Finally, a superelement Superelement 2 is constructed with 15 nodes or 180 DOFs. That will reduce calculation greatly in analysis of the TWF composites.

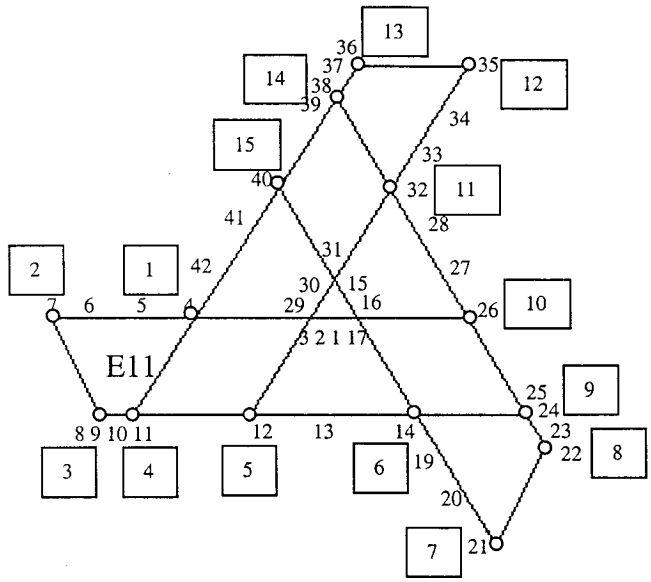

Figure2.11: Assemblage of Superelement 2

2.3 Conclusions

Two finite element models (Superelement 1 and Superelement 2) have been developed for prediction of mechanical behavior of TWF composites. Superelement 1 is a 15-node superelement constructed of six identical 8-node 3D isoparametric elements and three identical 4-node 2D-isoparametric laminate elements. Superelement 2 is similar to the first element except that this element takes into account the geometric and material properties of the twisted yarns. The assembly is done by the pseudo element technique suggested herein and static condensation procedure. The availability of these elements allows for the analysis of complex structures of the triaxial fabric. Superelement 1 can be used for the vibration analysis with some economy of computer space and time. Superelement 2 can be used for detailed stress analysis and for strength prediction. Though these two models are developed for the TWF composites, the ideas of their construction

can be applicable for analytical models and other kinds of elements used for other kinds of textile composites. The core of these ideas is the space projection technique, i.e., any complex geometric object can be formed from simply geometric object through the projection of one space to another space. For the TWF composites, the twisted yarn can be formed using the space projection from simple unidirectional lamina. Also the complex constitutive relation of the yarn can be obtained easily in same way. Their application provides the ability to analyze the textile composites with complex geometric and constitutive relation.

Valuation and application of Superelement 1 and Superelement 2 in mechanical behavior of the TWF composites will be presented in a subsequent chapter.

Chapter 3

Verification of the Finite Element Models and Elastic Constants of TWF Composites

Two elaborate finite element models are developed for the TWF composites and these are presented in Chapter 1. This chapter presents examples using the finite elements developed and experimental work to obtain results for comparison purposes. Some examples are provided for the verification of the accuracy and usefulness of these finite elements. One example deals with the TWF specimens subjected to loading along an axial yarn direction. The other example deals with other TWF specimens subjected to loading transverse to the axial yarn direction. Effects of the width and length of the sample are examined. The experimental work itself required special consideration. Non-contact laser extensometer method was used for the deformation measurement. The significance and meaning of the results are discussed.

3.1 Experimental Work

Most of the experimental work [72] was carried out by Mr. Paul Ouellette. It is presented here for comparison and research integration. Simple sheets of TWF composites (fabric

and cured resin) were supplied from YLA Corporation. Table 3.1 lists the geometric parameters of the unit cell measured from the microscopic photographs of the TWF composites. Table 3.2 gives the fiber and matrix properties for the fiber volume fraction V_f = 0.695. Table 3.3 shows the effective elastic properties of the impregnated yarn obtained by using the composite Strength-Of-Materials approach [73].

Table 3.1: Geometric parameters of the TWF

(measured on the samples supplied from YLA Corporation)

Geometric parameters	Values
Yarn thickness t_y (mm)	0.07
Resin thickness t_r (mm)	0.001
Yarn width W1 (mm)	0.85
Larger bridging distance W2 (mm)	1.10
*Smaller bridging distance W3 (mm)	0.1185
*Unit cell's height W4 (mm)	2.755
*Unit cell's width W5 (mm)	3.182
Fabric areal density (g/cm^2)	0.0158

* The starred quantity can be calculated using the non-starred quantities, which are measured.

Table 3.2: Elastic properties of fibers & matrix

(provided from the manufacturer specification sheet)

Material	E_L (GPa)	E_T (GPa)	G_{LT} (GPa)	G_{TT} (GPa)	v_{LT}	ρ (gm/cm^3)
Carbon Fiber	500.0	40.0	24.0	14.3	0.26	2.10
Epoxy Resin	3.5	3.5	1.3	1.3	0.35	1.17

Table 3.3: Elastic properties of the impregnated yarn of TWF composites

Material	E_L (GPa)	E_T (GPa)	G_{LT} (GPa)	v_{LT}	v_{TT}	V_f	ρ (gm/cm^3)
carbon/epoxy	338.57	12.40	5.61	0.287	0.437	0.695	1.8164

Tensile tests were performed. A total of thirteen specimens were cut from sheets of the TWFs which were square with dimension of about 300 mm by 300 mm. Specimens were nominally 300mm by 50mm, the cut being made through the centers of the hexagonal openings. Aluminum alloy gripping tabs, two at each end, were bonded to the specimens. The tests are all quasi-static, uniaxial tensile tests (loading speed is 0.2 mm/minute). The specimens were held using hydraulic wedge grip, and pulled in tension in the direction of the specimen (long) neutral axis. Figure 3.1 shows a photograph of the specimen in the testing machine.

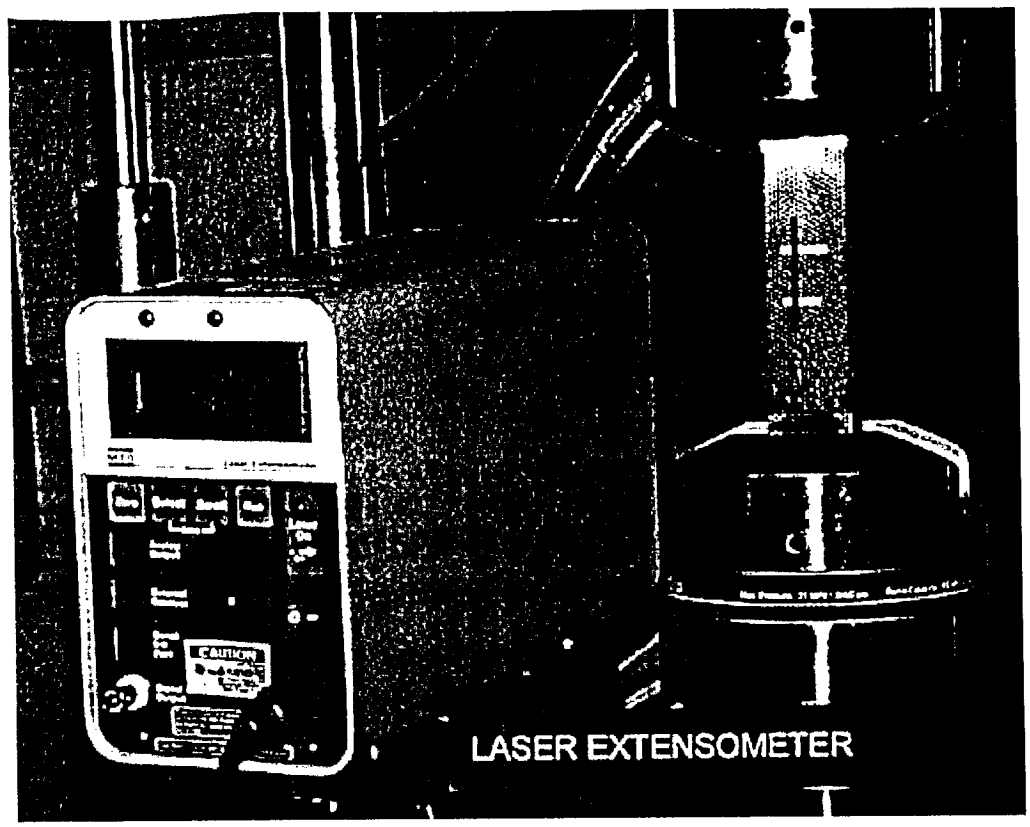

Figure 3.1: Photograph of the TWF specimen

One of the challenges in the experimental determination of the elastic properties of the TWF materials is the measurement of strains. Since the material contains holes that are larger than the fiber yarns, placing electrical strain gages will only allow the determination of very local strain values and these are not representative of the "averaged" properties of the material. To overcome this problem a non-contact measurement using laser extensometer was used. The laser extensometer used is an MTS LX300. For this, a gage length needs to be set up. As shown in Figure 3.1, two pieces of

reflective tape are positioned on the specimen at a convenient distance apart (from 8mm to 81mm). The laser extensometer scans the tape separation distance 100 times per second. The laser extensometer can be set up to scan along different directions. To identify the different relevant directions related to the measurement using laser extensometer, the following angles are defined:

- θ is the angle between the 0^{o} yarn line and load line.
- α is the angle between laser scan line and load line.
- β is the angle between another scan line and load line.

Figure 3.2 shows the definition of these angles.

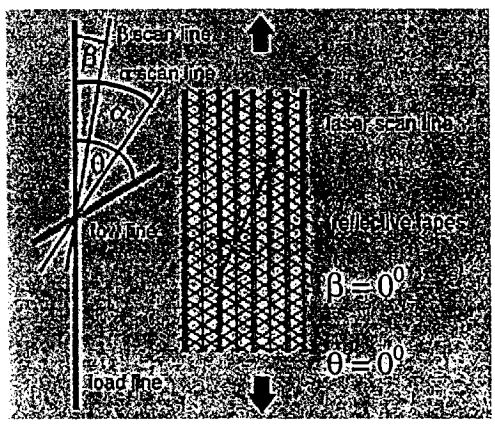

Figure 3.2: Definition of different orientations for laser scan

During the tensile tests, the separation between the reflective tapes and applied loads were recorded and stored on disks. The strain is calculated by dividing the change in tape separation by the original distance between the tapes.

The stress is determined by dividing the load by the cross section area. The cross section area is obtained as the product of width and thickness. Due to the ondulation of the TWF there can be many cross section areas. This is due to the fact that at some location, the thickness consists of only one yarn thickness while at other locations, the thickness consists of two yarn thicknesses. Therefore there can be four different thicknesses: those corresponding to one yarn thickness, two yarn thicknesses, the average (obtained by the weighted average of the one-yarn thickness and two-yarn thickness) and the nominal (obtained by measuring the TWF sheet using a micrometer). The width is obtained by direct measurement on the sample using a micrometer. The nominal cross section area based on measured thickness and measured width is used here.

Two different types of test were carried out. In one type, the loading direction is along the direction of one yarn type (this is referred to as the 0° yarn) i.e. $\theta = 0^{\circ}$. In these specimens, there are eighteen 0° yarns (or tows). The properties obtained using this method are called the longitudinal properties. In the other type, the loading direction is transverse to the 0° yarns, i.e. $\theta = 90^{\circ}$. The properties obtained are called the transverse properties.

Tensile moduli were determined from the slope of the linear portion of the stress-strain curve. It should be noted that strain-stress curve is not linear. Figure 3.3 shows a typical strain-stress curve for the TWF composites when loading is along the longitudinal

direction. This curve was obtained from specimen C4 (Table 3.4). The initial slope is smaller than the slope at larger stress. This can be explained by the straightening of the ondulation of the yarns. The yarns become stiffer as they are more and more straightened. For comparison with finite element results, the initial modulus is used.

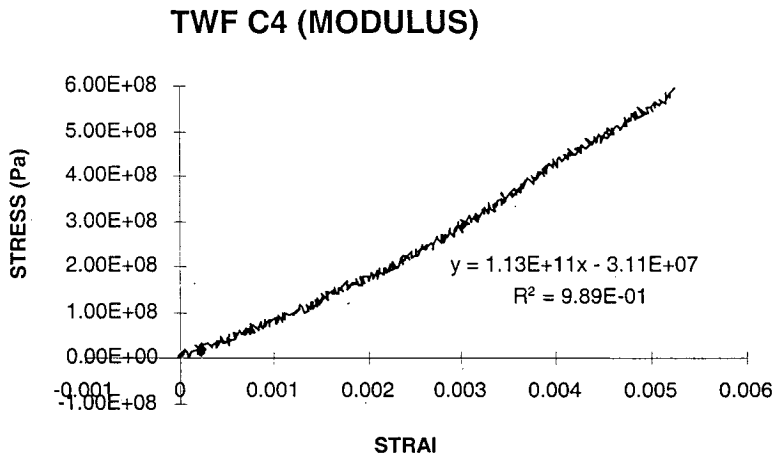

Figure 3.3: Non-linear stress-strain behavior of the TWF in the longitudinal direction

Longitudinal properties

Table 3.4 shows the longitudinal Young's moduli of the TWF specimens. The measured modulus values of various specimens distribute between 27.87 GPa and 37.87 GPa. Average modulus is 32.24 GPa. The numbers indicated above are for the initial portion of the modulus value.

Table 3.4: Measured longitudinal Young's moduli of the TWF specimens

Specimen#	Strength(GPa)	Ultimate Strain (%)	Modulus (GPa)
B2	2.577	0.58	33.05
B4	2.581	0.60	30.92
C1	2.463	N.A.	N.A.
C2	2.610	0.59	34.89
C3	2.364	0.57	28.42
C4	2.184	0.52	31.21
D1	1.868	N.A.	N.A.
D2	2.169	0.51	33.38
D3	2.434	0.61	27.87
D4	2.419	0.66	35.00
E1	2.607	0.58	33.71
F1	2.489	0.54	37.87
G1	2.360	0.60	28.27
Average	2.394	0.58	32.24

Table 3.5: TWF test transverse to zero degree yarn

(50 mm wide unless otherwise noted)

Specimen#	Strength (Pa)	Ultimate Strain (%)	Modulus (GPa)
B1	1.066E+08	5.135E-03	2.29E+01
B3	9.616E+07	4.411E-03	2.08E+01
B5	1.143E+08	5.415E-03	2.25E+01
B6	1.097E+08	6.284E-03	1.96E+01
B7	1.175E+08	6.446E-03	1.66E+01
Group Ave.	1.089E+08	5.538E-03	2.05E+01
Group Std. Dev.	8.233E+06	8.409E-04	2.54E+00
Group C.O.V. (%)	7.56	15.18	12.42
E3*	7.743E+07	N.A.	N.A.
E4*	1.172E+08	5.233E-03	2.33E+01
E5*	1.071E+08	5.175E-03	2.34E+01
Group Ave.	1.006E+08	5.204E-03	2.34E+01
Group Std. Dev.	2.068E+07	4.076E-05	7.07E-02
Group C.O.V. (%)	20.56	0.78	0.3

* Nominal width of 43 mm.

Transverse properties

Table 3.5 shows the results from the transverse tensile tests. Two types of specimens were used. Specimens of series B have width of 50 mm while specimens of series E have width of 43 mm. Specimens with larger width show smaller modulus (20.5 GPa) as

compared to specimens with smaller width (23.4 GPa). This can be explained by the fact that the stiffness is provided by the off-axis yarns when these yarns are connected to the grips (Figure 3.9). This distance between two connective yarns is about 3.18 mm (Figure 3.7). Increasing the width of specimen from 43 mm to 50 mm increases the width by 7 mm. The addition of 2 more 0^0 yarns requires an increase in width of 6 .36 mm. As such an addition al 0.64 mm (7-6.36=0.64 mm) does not add any more off-axis yarns. This extra 0.64 mm increase in width effectively decreases the modulus due to the process of calculation.

In the above explanation, the length of the specimen is kept fixed. If the length is variable, then this should also have an effect on the modulus of the specimen. This is because for a certain width, shorter specimens would have more clamped yarns (a clamped yarn is a yarn that has both ends clamped by the grips) than longer specimens. As such, short specimens would tend to have larger stiffness. Since both width and length may have effects on the modulus, the proper parameter may be the aspect ratio (length over width) of the specimen. The effect of this aspect ratio can be studied more easily using finite element modeling to be presented in the subsequent section.

Poisson's ratio measurement

In general, we define the ratio $\rho_{\theta,\alpha/\beta} = \varepsilon_\alpha / \varepsilon_\beta$, where ε is strain, α is the direction along which a first strain is measured, and β is the direction along which a second strain is measured. Let the angles be measured counter clockwise from the (vertical) load

direction. Assume a yarn makes an angle θ with the (vertical) loading direction. (See Figure 3.4) Then the other two yarns make angles of (θ +/- 60) degrees with the (vertical) loading direction.

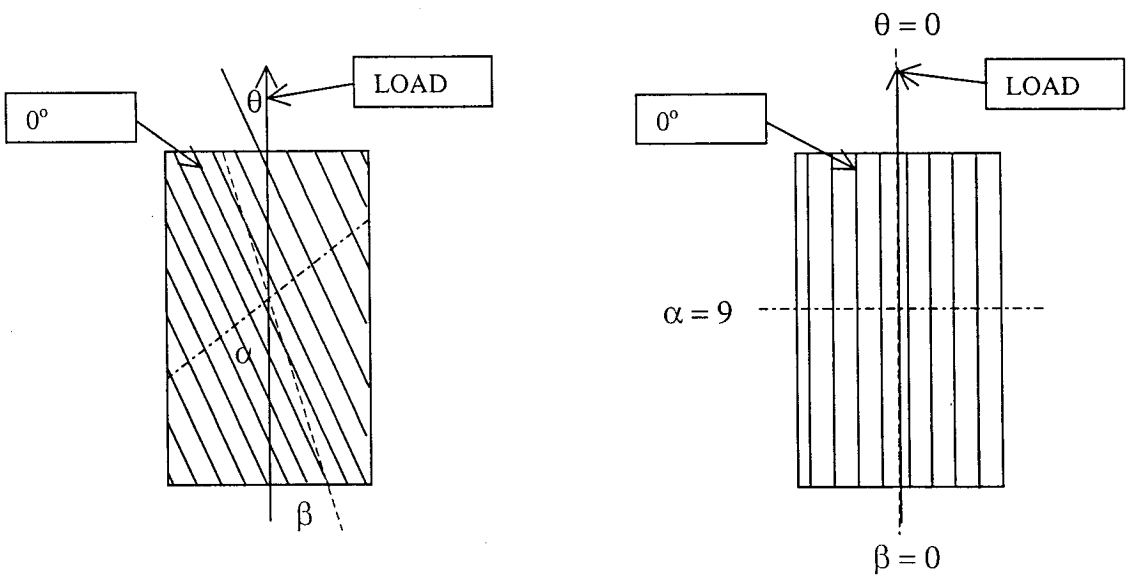

Figure 3.4: The general test configuration for Poisson's ratio.

(The configuration on the right shows the particular case of interest used to find the Poisson's ratio of the Triax fabric when the fabric is loaded in the direction of a 0° tow, i.e., when $\theta = 0^\circ$. So far, only tests with $\theta = 0^\circ$ have been conducted)

Keeping θ fixed, we can measure a series of ratios, $\rho_{\theta,\alpha/\beta}$, describing the TWF deformation. We can also vary θ producing a series of ratios for each TWF test orientation θ. If a tensile load is applied to the specimen, with $\alpha = 90^\circ$ and $\beta = 0^\circ$ we may identify the ratio $\rho_{\theta,90/0}$ with the Poisson's ratio ν_θ for the specific orientation, θ, of the TWF.

We can only measure strain in a single direction during a test. Therefore, we must relate

the strains that are used to compute the ratio using the stresses (i.e., the loads divided by the nominal TWF cross-sectional area) over many independent tests. Since we want an overall view of the behavior over an elastic range, we use the slopes (as shown below), where the subscript "l" refers to the loading direction.

$E_{\theta,\alpha}$ = Slope of σ_l *vs* ε_α (this is not a usual modulus, but rather merely the slope of σ_l *vs* ε_α) $E_{\theta,\beta}$ = Slope of σ_l *vs* ε_β (this is not a usual modulus, but rather merely the slope of σ_l *vs* ε_β) $\rho_{\theta,\alpha/\beta} = -\varepsilon_\alpha/\varepsilon_\beta = [(\sigma_l/E_{\theta,\alpha}) / (\sigma_l/E_{\theta,\beta})] = E_{\theta,\beta}/E_{\theta,\alpha}$

For $\theta = 0^\circ$, $\alpha = 90^\circ$, and $\beta = 0^\circ$, we can use specimens C4 and C5 as examples. Both were tested by loading parallel to the 0° yarns. C4 was tested monotonically to rupture, with the strain measured in the loading direction, i.e., $\beta = 0^\circ$. C5 was tested monotonically to rupture, with the strain measured transverse to the loading direction, i.e., $\alpha = 90^\circ$. Figures 3.5 and 3.6 show the test results. A number of strain ratios (in this particular test configuration, we may say Poisson's ratios) can be calculated depending on where the σ *vs* ε slopes are measured. If we measure the slope for all the data (plot at top right in Figure 3.5) we have, $E_{0,0}$ = 44.4 GPa from specimen C4. If we measure the slope not going through the origin (plot at bottom right in Figure 3.6) we have $E_{0,90}$ = -80.54 GPa from specimen C5; thus we report a Poisson's ratio of $\rho_{0,90/0}$ =- 44.4/(-80.54) = 0.55 (which may be identified with Poisson's ratio for the TWF in test orientation $\theta = 0^\circ$). If we use other slope values, the Poisson's ratio would be different.

Recall that σ_l is the load (in the vertical direction) divided by the cross-sectional area of the specimen. The cross-sectional area can be the net area or the nominal area or some

other measure of the area, but the area chosen must be consistent and explicitly specified if comparisons to other reported material properties are to be made.

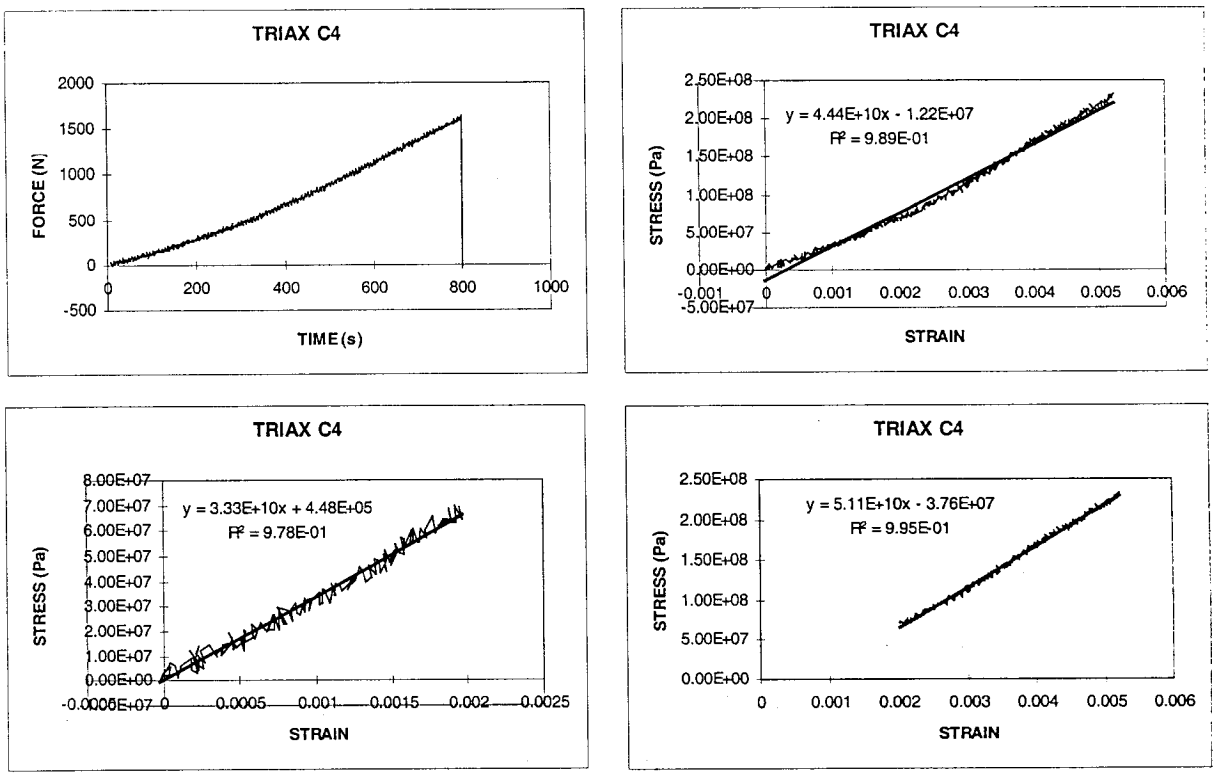

Figure 3.5: Test results for specimen C4 tested monotonically to rupture (strain measured in loading direction)

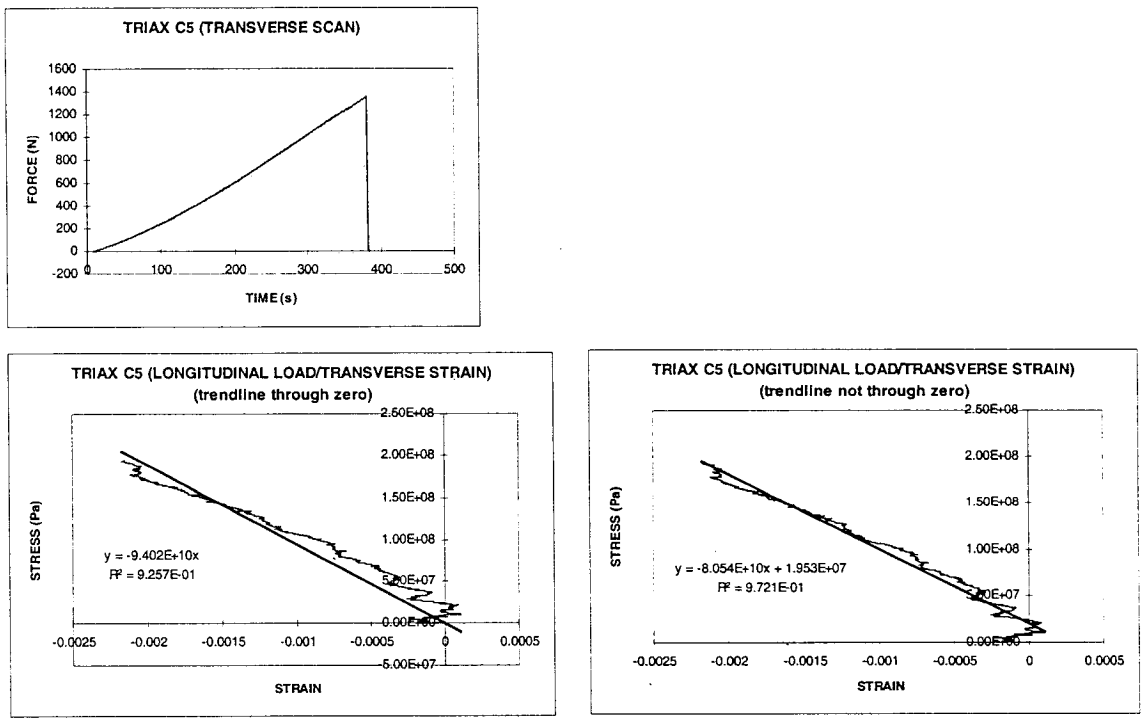

Figure 3.6: Test results for specimen C5 tested monotonically to rupture

(strain measured transverse to loading direction)

3.2 Finite Element Analysis

3.2.1 Comparison of numerical results with experiments

In Chapter 1, there were two finite elements developed for analysis of the TWF composites: superelement 1 and superelement 2. In superelement 1, the connection between two crossover parts is modeled as a straight segment with no twist. Superelement 2 is developed based on superelement 1 with improving element connection and fully considering characteristics of geometric and material properties of

twisted composite yarns. Superelement 1 can be used for the vibration analysis with some economy of computer space and time. Superelement 2 is better for detailed stress analysis and for strength prediction. In this section, these two superelements are evaluated by modeling the experimental specimens. The schematic of the superelements is shown in Figure 3.7. Superelements are used to model the two loading cases: case 1 and case 2. Case 1 is for longitudinal loading and case 2 is for transverse loading (Figure 3.8).

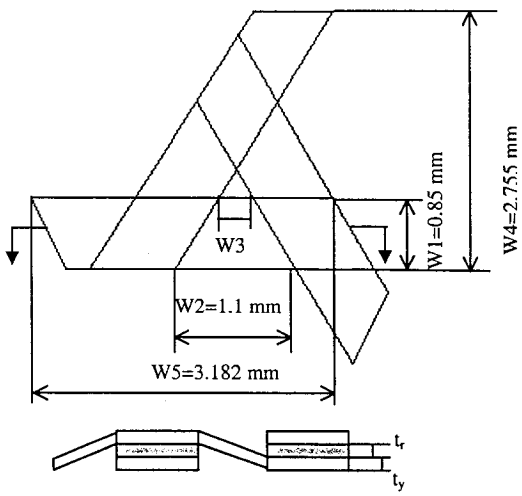

Figure 3.7: Schematic of Superelement 2

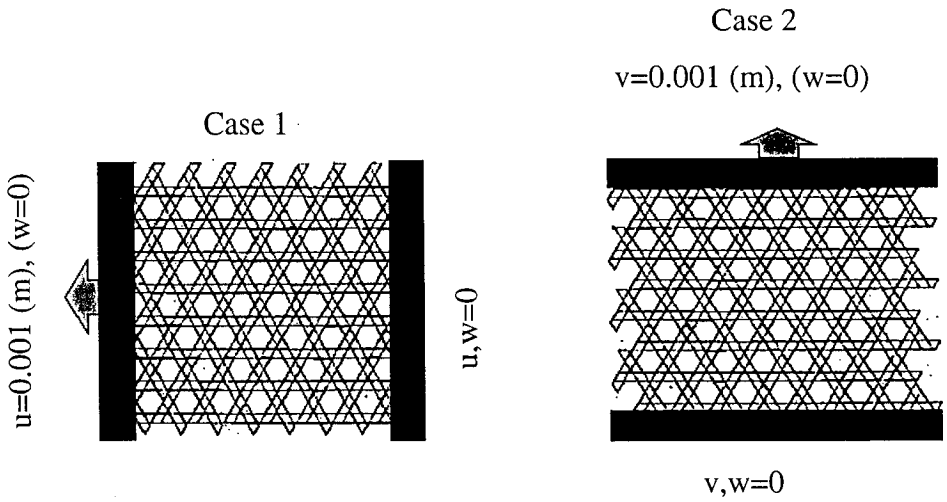

Figure 3.8: Two cases of loading

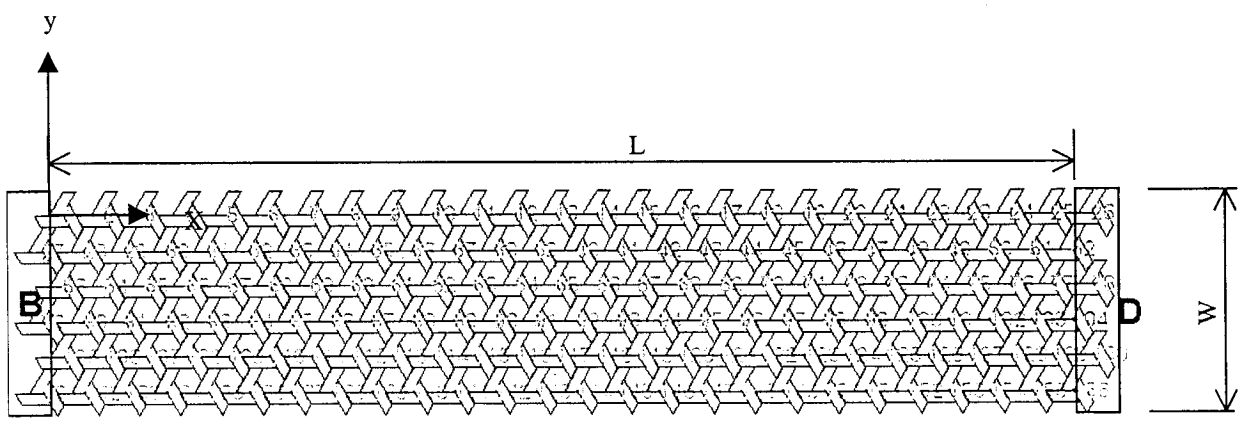

Figure 3.9: Finite element model for case 1

Figure 3.9 shows the FE model for the model in case 1. This FE model has 26 superelements along X direction (71.6 mm long) and 6 superelements along Y direction (22.65 mm wide). These FE model dimensions are taken much smaller than the actual

specimens (300 mm long and 50 mm wide) because of the computer memory limit. However, this FE model can still model the experimental specimens well, because it was found that the Young's moduli and Poisson's ratios calculated using the FE model are not sensitive to the size of the FE model as long as the aspect ratio of the specimen is greater than 3.5. This will be presented in later sections.

Accordingly the FE model of TWF panel was selected with length L and width W. Length L and width W refer to the dimension of the panel in X and Y directions respectively. As shown in Figure 3.9, at region B of the FE model, the deflection in Z direction w of all the nodes is fixed (w = 0) and the displacement u in X direction is assigned a value of -1 mm to simulate displacement tension load. At region D, displacements w and u of all nodes are fixed (w = u = 0). Displacement v in Y direction at node 1 is fixed (v = 0) so as to remove the rigid body motion of the FE model. Note that due to the jagged nature of the elements, there is no clear line where loads are applied or where the constraints are fixed. Rather, there is a region within which all nodes would be subject to the same condition of loading or fixity. For example, within region B, all nodes that fall within this region would be subject to the same uniform displacement as mentioned above. Young's modulus and Poisson's ratio of the TWF were determined respectively by

$$E_1 = \frac{F/(Wh)}{\varepsilon_1}, \qquad \nu_{12} = -\frac{\varepsilon_2}{\varepsilon_1}$$

where F is tension force loaded at region B of the panel in X direction, h is the nominal thickness, W is the nominal width of the TWF panel and ε_1 is the strain along X

direction. Subscripts 1 and 2 denote the X and Y direction respectively. In calculation, the effective elastic properties of yarns in Table 3.3 were used. Force F is obtained by adding reaction forces in X direction at all nodes at region B. Strain ε_1 = 1 mm/L and ε_2 = $\Delta v/W$, where Δv is width change at a certain section of the panel.

For case 2, the FE model is shown in Figure 3.10. The FE model has 6 superelements along X direction and 26 superelements along Y direction. As shown in Figure 3.9, at region A of the FE model, the deflection w of all the nodes is fixed (w = 0) and the displacement v in Y direction is assigned a value of -1 mm to simulate displacement tension load. At region C, displacements w and v of all nodes are fixed (w = v = 0). Displacement u in X direction at node 1 is fixed (u = 0) so as to remove the rigid body motion of the FE model. Young's modulus and Poisson's ratio of the TWF were determined respectively by

$$E_2 = \frac{F/(Lh)}{\varepsilon_2}, \qquad \nu_{21} = -\frac{\varepsilon_1}{\varepsilon_2}$$

where F is tension force loaded at region A of the panel in Y direction. Force F is obtained by adding reaction forces in Y direction at all nodes at region A. Strain ε_2 = 1 mm/L and $\varepsilon_1 = \Delta u/L$, where Δu is length change at a certain section of the panel.

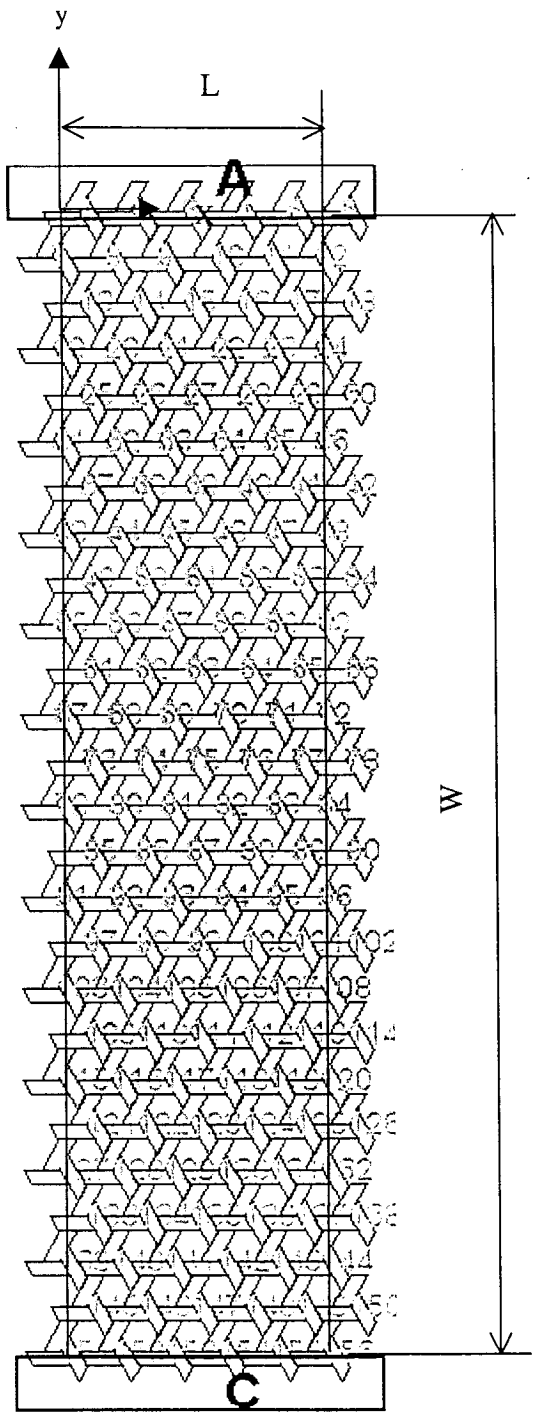

Figure 3.10: Finite element model for case 2

Table 3.6: Predicted and measured TWF properties

	Modulus E_1 (GPa)	Poisson's ratio v_{12}	Modulus E_2 (Gpa)	Poisson's ratio v_{21}
Experiment	32.24	0.55	20.5	–
Standard deviation	5.63	–	2.54	–
Se 2	30.01	0.58	26.55	0.56
Se 1	36.88	0.51	33.61	0.46

Note: Se denotes short of superelement.

The Young's modulus and Poison's ratio evaluated from the FE model prediction and from experimental measurement are summarized in Table 3.6. Considering the experimental values in Table 3.4, for Young's modulus E_1 in 0^0 yarn direction, the modulus value from Superelement 2 and Superelement 1 fall within the range of scatter of experiment values. Superelement 1 gives the value close to the upper bound of the range of the experimental values. Superelement 2 gives the value close to the average of the experimental values. For transverse modulus E_2, the modulus value from Superelement 2 is closer to the average of the experimental values than Superelement 1. For Poisson's ratio v_{12}, the ratio value from Superelement 2 closer to the experiment than Superelement 1. The agreement is within 6%. The above shows that Superelement 2 is better suited for modeling the behavior of the TWF panel.

3.2.2 Determination of the deformations

The detailed deformation of the TWF structure is complex. Figure 3.11 shows the deformation of a sample loaded in the x direction and Figure 3.12 shows the deformation of the sample loaded in the y direction.

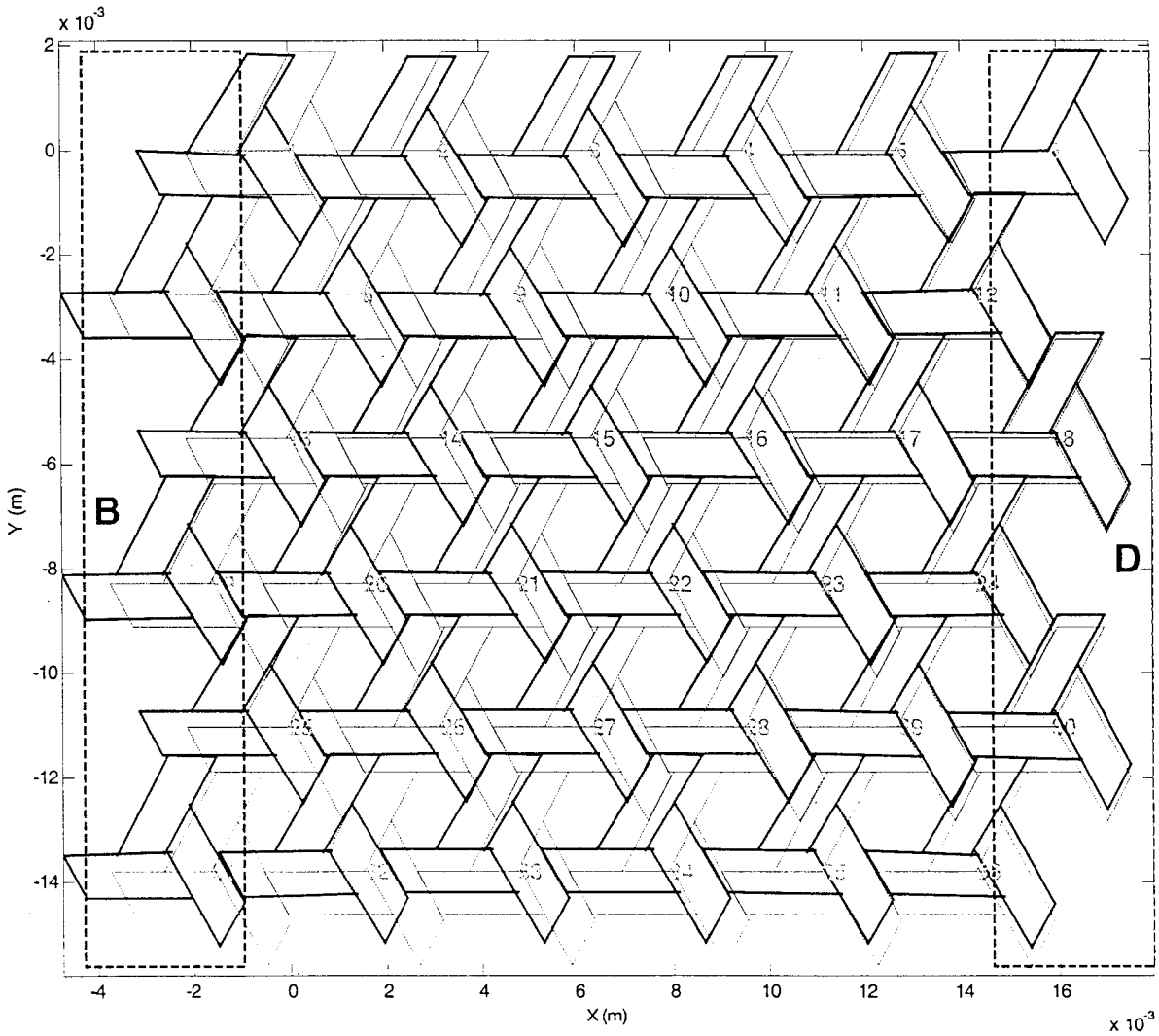

Figure 3.11: Deformation of sample when loaded along the tow direction

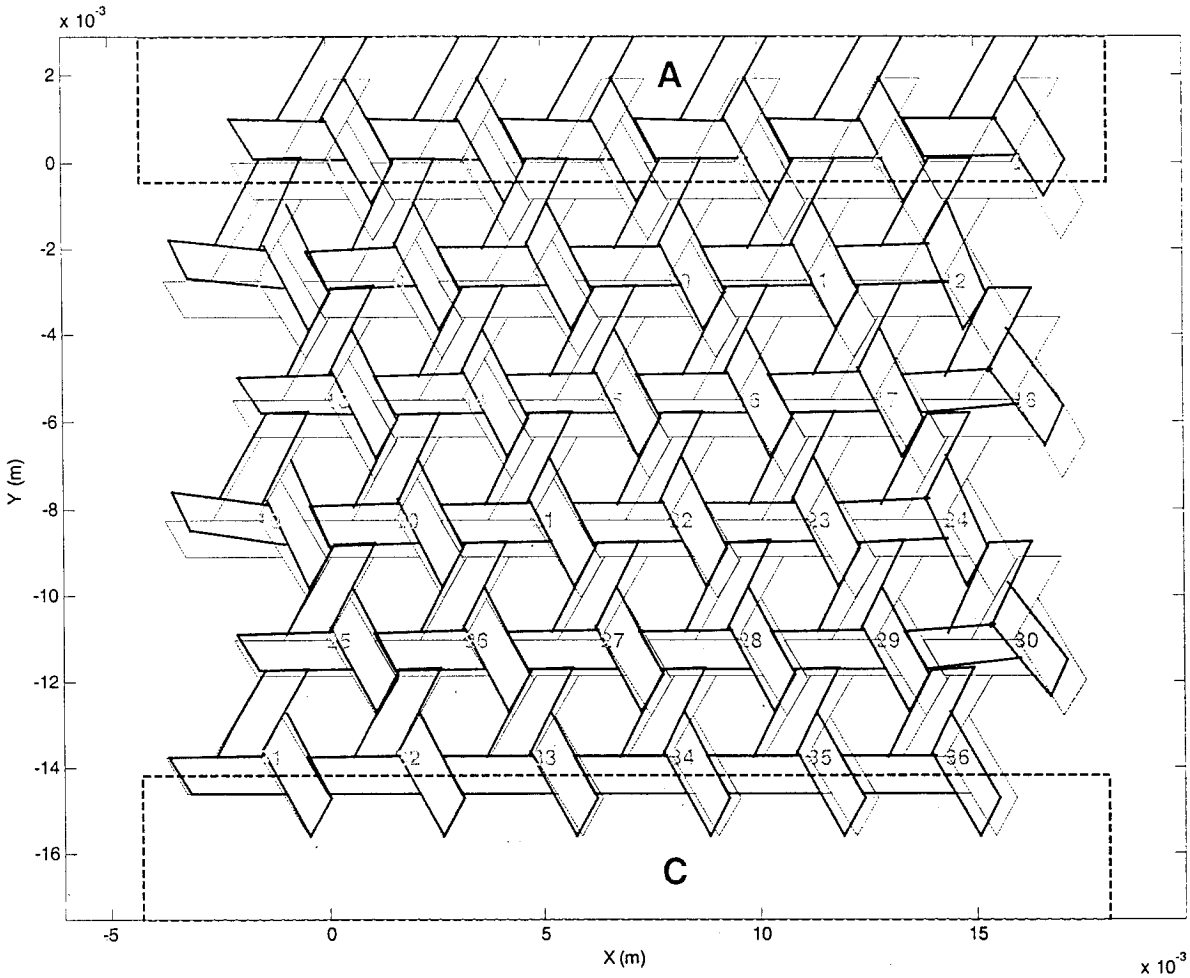

Figure 3.12: Deformation of sample when loaded transverse to the direction of a yarn

In Figure 3.11, the sample is fixed at region D and loaded at region B. Loading is therefore along the direction of one set of yarns. The thin lines represent the undeformed configuration and the thick lines represent the deformed configuration. First examine the yarns along the loading direction. These yarns extend along the direction DB. They also shift from outside toward the inside of the sample. Note that this lateral contraction is not

symmetrical. If the orientation of the sample is vertical with D at the bottom, the contraction of the left yarns is more than that of the yarns on the right hand side. This is due to the unsymmetrical geometry of the yarns included in the sample. Width effect is therefore can be important. This topic is discussed in a section below.

Considering now the yarns that make angles of $\pm 60^{o}$ with the loading direction. For clarity of terminology, if the configuration of the sample is such at that DB is vertical with D at the bottom, we call the yarns as one o'clock and eleven o'clock yarns. The one o'clock yarns rotate in a counterclockwise direction whereas the eleven o'clock yarns rotate in a clockwise direction. This rotation can make the contraction of the sample to be a function of the space variable along the length of the sample. The determination of the Poisson ratio therefore would depend on the space variable.

Table 3.7: Poisson ratios at different sections along the length of the sample.

Section location X (m)	Poisson's ratio v_{12}
1.0407^{e}-3	0.49695
4.2222^{e}-3	0.57174
7.4037^{e}-3	0.58832
1.0585e-2	0.55448
1.3767e-2	0.37103
Average	0.51650

Table 3.8: Poisson ratios at different sections along the width of the sample.

Section location Y (m)	Poisson's ratio v_{21}
0	0.33094
-2.7553^{e}-3	0.49346
-5.5105^{e}-3	0.55127
-8.2658^{e}-3	0.54440
-1.1021e-2	0.47693
-1.3776e-2	0.34852
Average	0.45759

Considering the above, the Poisson ratios at different sections along the length of the sample were determined. They are shown in Table 3.7. The average Poisson ratio is obtained from the above values to be 0.52.

In Figure 3.12, the sample is fixed in the C region and loaded in the A region. Again the thin lines represent the undeformed configuration and the thick lines represent the deformed configuration. If AC is along the vertical direction, it can be seen that there is bending in the horizontal yarns, particularly those close to the fixed end. Similar rotations of the off-axis yarns are also observed. It is clear that the width and length of the sample have influence on its deformation. The values of Poisson ratios at different sections along the length of the sample are shown in Table 3.8. The average value of the Poisson ratio is 0.46.

3.2.3 Effects of panel aspect ratio on elastic constants

The TWF is a special woven structure with holes. As such, the constraint end and loaded end of a sample made of this material may not have effect on all the yarns of the sample. For example, when loading is along one set of yarns (for example the 0^0 yarns), not all ends of the off-axis yarns are clamped. Some off-axis yarns may ride along without any of their ends clamped by either the constraint region or the loaded region. Some other yarns may have one end clamped and the other end not clamped. Some yarns may have both their ends clamped. As such, the values of the modulus and Poisson's ratio obtained from experiments and finite element models may depend strongly on the aspect ratio of the sample. This effect needs to be investigated before meaningful results can be obtained. In the following, the effect of length and width of the sample for the two loading cases 1 and 2 will be examined.

(1) Effects of panel length on elastic constants

In this section we will investigate the effects of panel length on elastic constants. Firstly consider case 1. Four panels are selected with 6 by 6, 10 by 6, 20 by 6 and 26 by 6, respectively. Table 3.9 gives the effects of panel length (in X direction) on Young's modulus E_1 and Poisson's ratio v_{12}. These results are plotted in Figure 3.13. It can be seen that as panel length increases, the modulus E_1 increases and approach an asymptotic value. As the length changes from 6 unit cells to 26 unit cells, modulus E_1 changes from 29.85 GPa to 30 GPa, which is 0.5%. This can be considered negligible for this structure. Therefore, it can be said that the modulus E_1 is not sensitive to panel length or boundary location. However, the effect on Poisson's ratio v_{12} (average) is more significant.

Poisson's ratios v_{12} obtained at various locations along X direction are shown in Figures 3.14, 3.15, 3.16 and 3.17 for the panel of 6 by 6, 10 by 6, 20 by 6 and 26 by 6, respectively. At the regions close to load region B and boundary region D, since the yarns are directly loaded or restrained, the Poisson's ratio values are smaller. At the region where the yarns are not loaded nor restrained, the Poisson's ratio v_{12} can be considered more correct. It can be seen that for a sample width of 6 unit cells, the panel length has to be at least 10 unit cells to provide sufficient gage area for a meaningful Poisson's ratio. The calculated Poisson's ratio v_{12} can be taken to be 0.58.

Table 3.9: Effects of panel length on modulus E_1 and Poisson's ratio v_{12} in case 1

Panel size X by 6	Aspect ratio (L/W)	Young's modulus E_1 (GPa)	Poisson's ratio v_{12}	Poisson's ratio v_{12} (average)
6	1.0000	29.870	0.59	0.52
10	1.6667	29.948	0.59	0.55
20	3.3333	30.003	0.58	0.56
26	4.3333	30.014	0.58	0.57

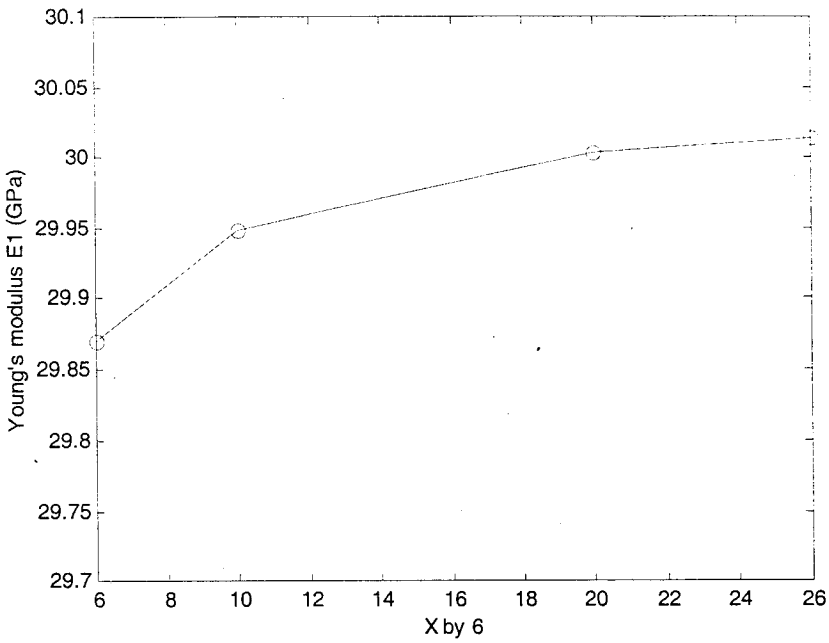

Figure 3.13: effects of panel length (X direction) on Modulus E1

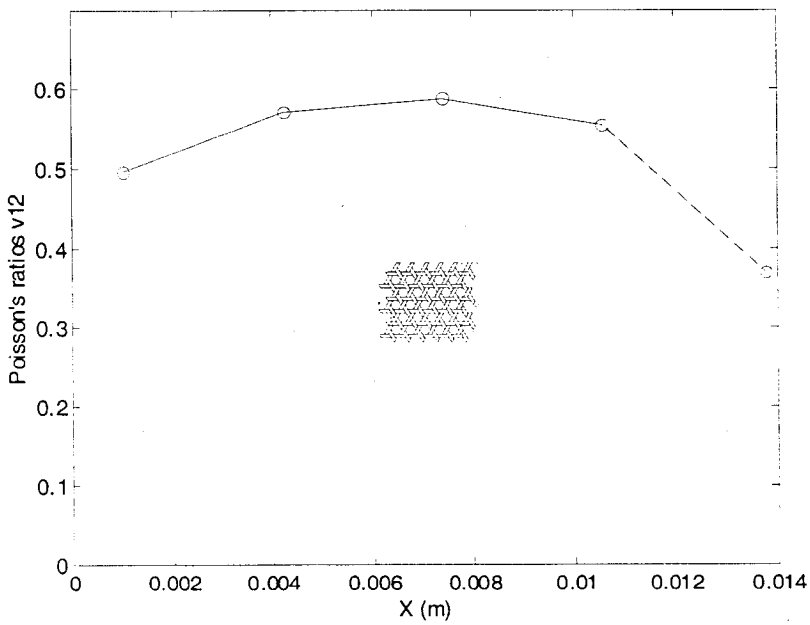

Figure 3.14: Poisson's ratio v12 of 6 by 6 panel in X direction

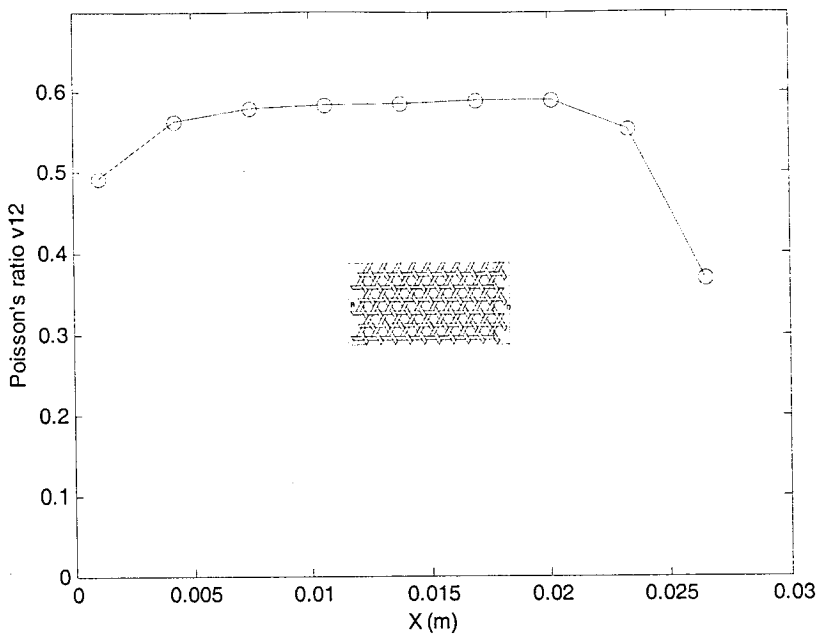

Figure 3.15: Poisson's ratio v12 of 10 by 6 panel in X direction

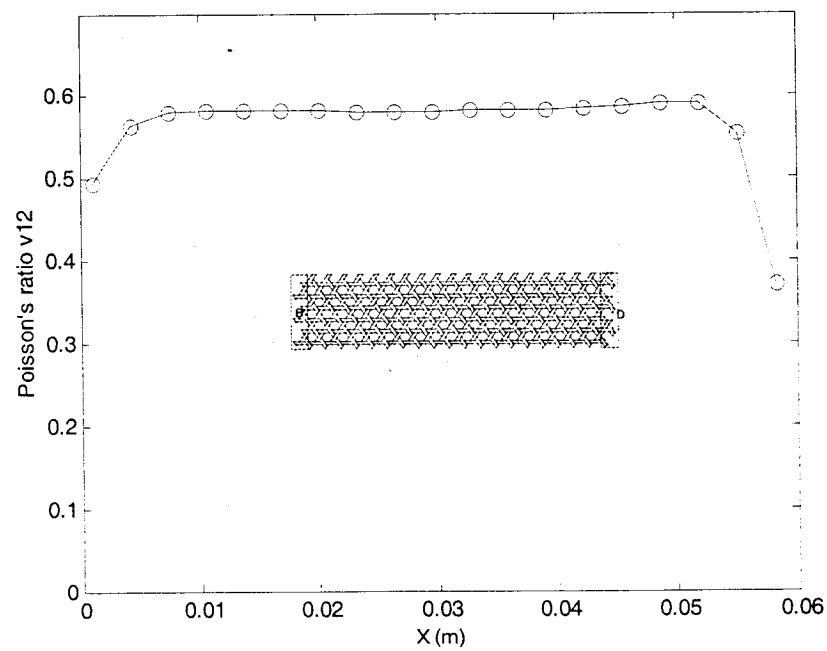

Figure 3.16: Poisson's ratio v12 of 20 by 6 panel in X direction

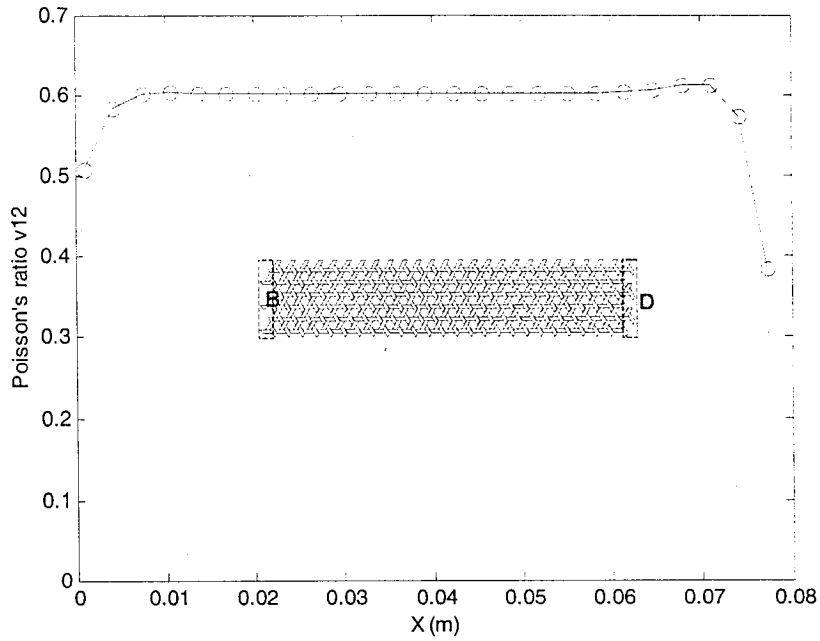

Figure 3.17: Poisson's ratio v12 of 26 by 6 panel in X direction

Now consider loading case 2. Four panels with 6 by 6 (6 unit cells along X direction by 6 unit cells along Y direction), 6 by 10, 6 by 20, and 6 by 26 are taken respectively. The effects of panel length (in Y direction) on the modulus E_2 and the ratio v_{21} are given in Table 3.10. Figure 3.18 shows the effects of panel length on modulus E_2. For a change of sample length from 6 unit cells to 26 unit cells, the modulus E_2 changes from 28.3 GPa to 26.5 GPa or 7 %. Figures 3.19, 3.20, 3.21 and 3.22 show the change of Poisson's ratios v_{21} along Y direction for 6 by 6, 6 by 10, 6 by 20, and 6 by 26 panel respectively. Different from case 1, the modulus E_2 is sensitive to panel length. It could be seen that for a sample width of 6 unit cells, the panel length has to be at least 10 unit cells to provide sufficient gage area for a meaningful Poisson's ratio. The calculated Poisson's ratio v_{21} can be taken to be 0.56. It is interesting to note that there is no significant

difference between v_{12} (0.58) and v_{21} (0.56) even though there is some difference between E_1 (30.01 GPa) and E_2 (26.55 GPa).

Table 3.10: Effects of panel length on modulus E_2 and Poisson's ratio v_{21} in case 2

Panel size 6 by X	Aspect ratio (L/W)	Young's modulus E_2 (GPa)	Poisson's ratio v_{21}	Poisson's ratio v_{21} (average)
6	1.0000	28.309	0.55	0.46
10	1.6667	27.322	0.58	0.50
20	3.3333	26.687	0.57	0.52
26	4.3333	26.551	0.56	0.53

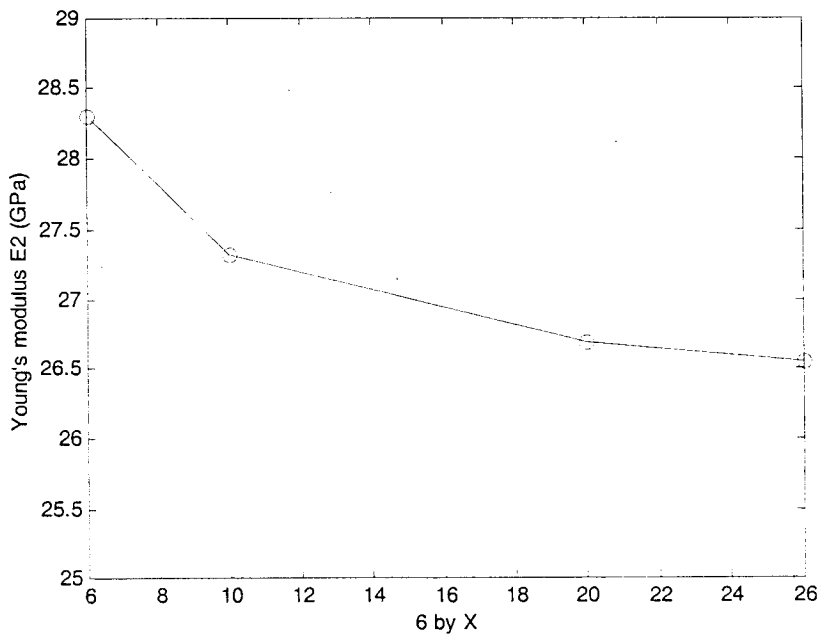

Figure 3.18: Effects of panel length (Y direction) on Modulus E2

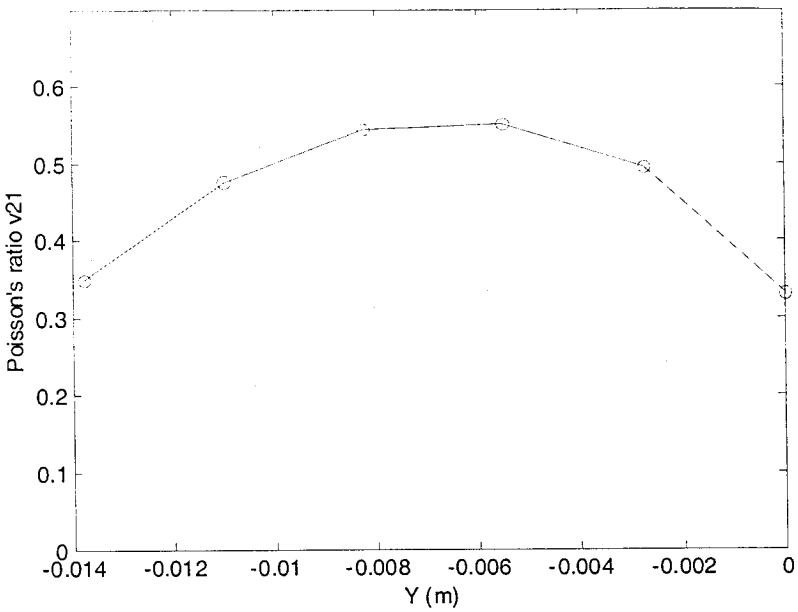

Figure 3.19: Poisson's ratios v21 of 6 by 6 panel in Y direction

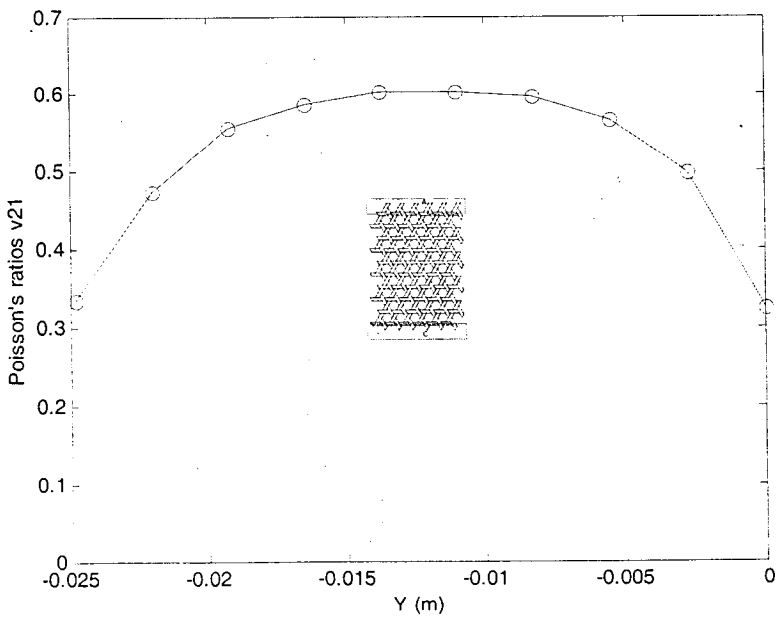

Figure 3.20: Poisson's ratio v21 of 6 by 10 panel in Y direction

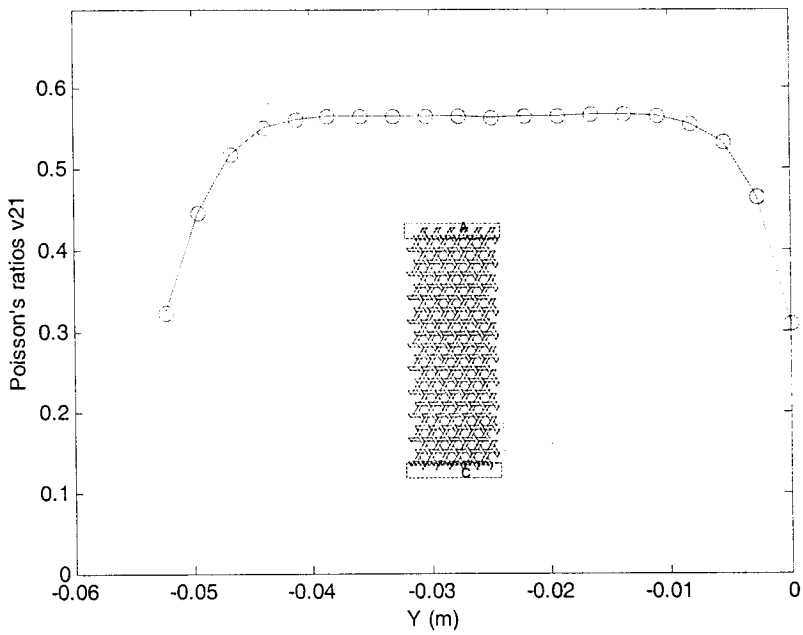

Figure 3.21: Poisson's ratios v21 of 6 by 20 panel in Y direction

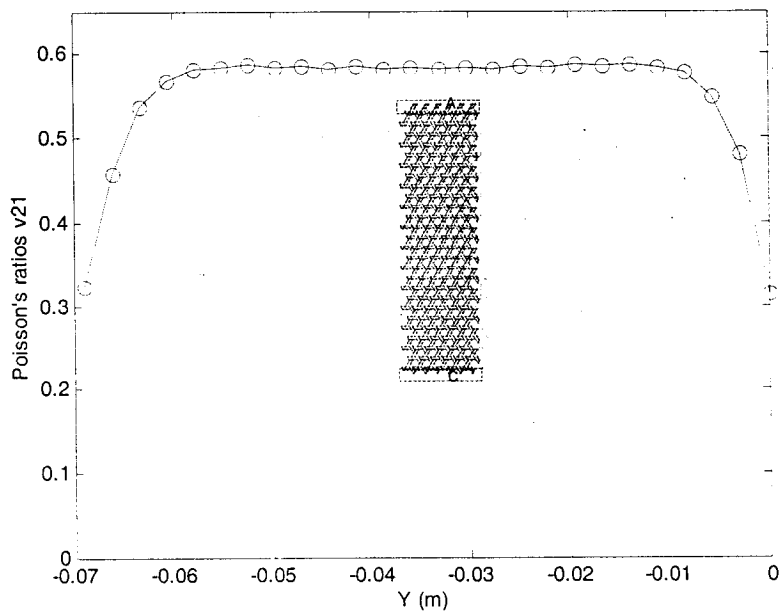

Figure 3.22: Poisson's ratios v21 of 6 by 26 panel in Y direction

(2) Effects of panel width on elastic constants

In this section, consider the TWF panels of certain length with various widths and study the effects of panel width on elastic constants. Also consider two loading cases. For case 1, the TWF panels have the dimensions of 6 unit cells in length and X (X = 4,6,8,$\cdots$,24) unit cells in width. For case 2, the panels have X (X = 4,6,8,$\cdots$,22) unit cells in width and 6 unit cells in length.

Table 3.11: Effect of width on modulus E_1 and Poisson's ratio v_{12} in case 1

Panel size 6 by X	Aspect ratio (L/W)	Young's modulus E_1 (Gpa)	Poisson's ratio v_{12}
4	1.5000	29.262	0.5742
6	1.0000	29.870	0.5883
8	0.7500	30.205	0.5711
10	0.6000	30.415	0.5584
12	0.5000	30.558	0.5505
14	0.4286	30.661	0.5453
18	0.3333	30.799	0.5388
20	0.3000	30.847	0.5367
22	0.2727	30.887	0.5350
24	0.2500	30.920	0.5336

First consider case 1. The change of Young's modulus E_1 and Poison's ratio v_{12} as a result of panel width is given in Table 3.11 and plotted in Figures 3.23 and 3.24. It can be seen that as panel width becomes larger, E_1 increases and approaches a value of 32.2 GPa. For Poisson's ratio, v_{12} reaches maximum at 6 by 6 and then decreases and approaches a value of 0.53.

Secondly consider case 2. The effect of panel width on elastic constants E_2 and v_{21} in case 2 is shown in Table 3.12 and plotted in Figures 3.25 and 3.26. Same as in case 1, as the panel width increases, E_2 increases and approaches a value of 32.2 GPa. V_{21} decreases monotonously and approaches a value of 0.5.

Table 3.12: Effect of width on modulus E_2 and Poisson's ratio v_{21} in case 2

Panel size X by 6	Aspect ratio (L/W)	Young's modulus E_2 (Gpa)	Poisson's ratio v_{21}
4	1.5000	25.710	0.5558
6	1.0000	28.309	0.5513
8	0.7500	29.640	0.5382
10	0.6000	30.447	0.5279
12	0.5000	30.988	0.5206
14	0.4286	31.374	0.5154
18	0.3333	31.889	0.5085
20	0.3000	32.070	0.5061
22	0.2727	32.217	0.5042

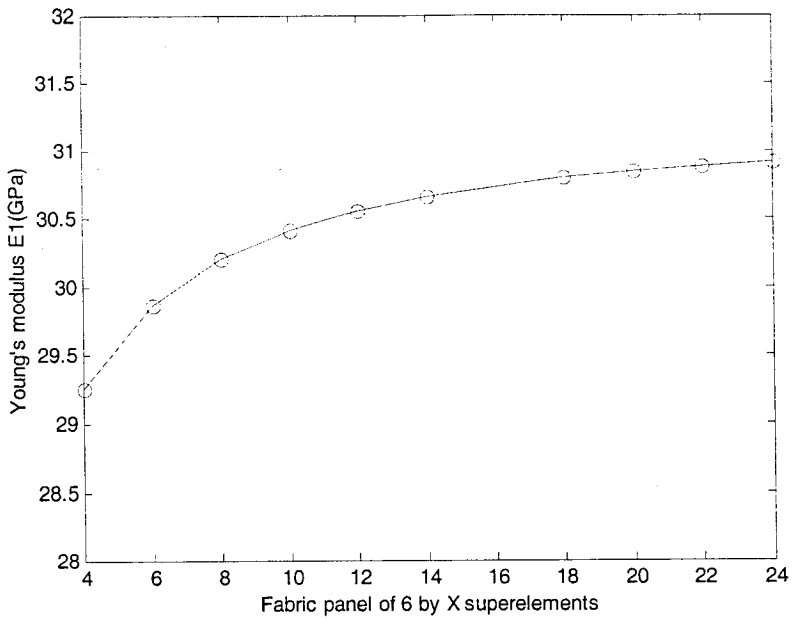

Figure 3.23: Effect of width on Young's modulus E1 in case 1

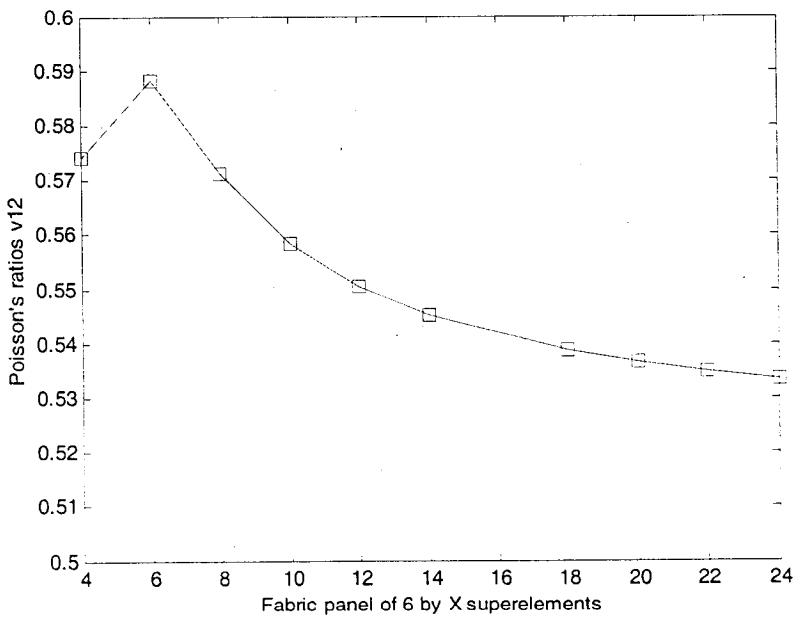

Figure 3.24: Effect of width on Poison's ratio v12 in case 2

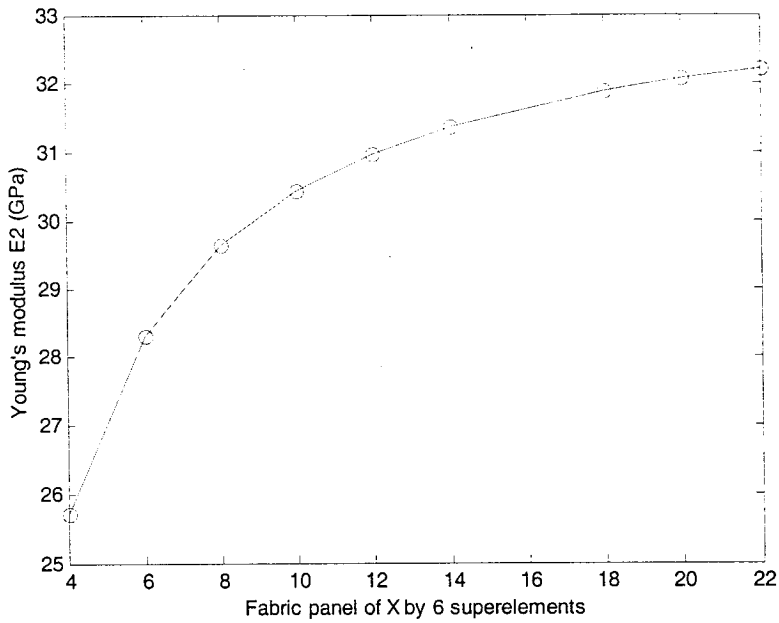

Figure 3.25: Effect of width on Young's modulus E2 in case 2

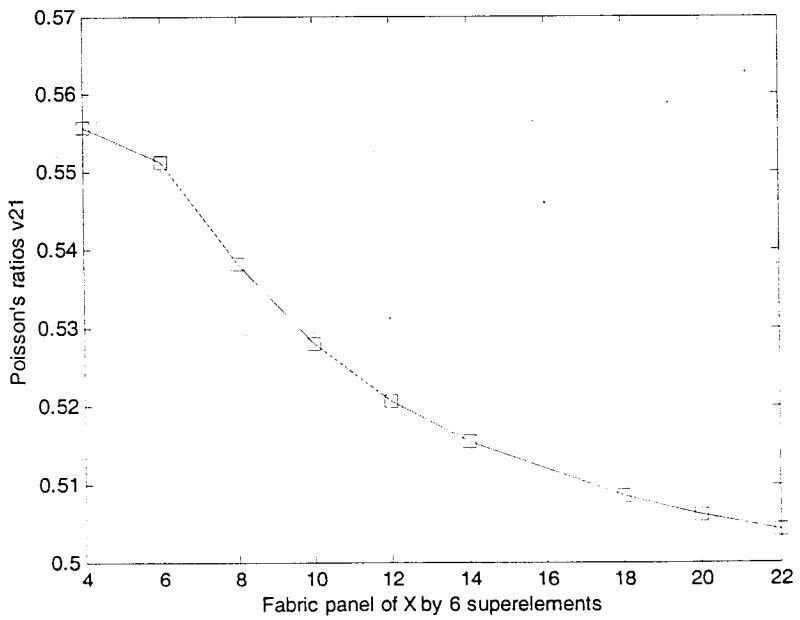

Figure 3.26: Effect of width on Poison's ratio v21 in case 2

Figures 3.13 and 3.18 show that by keeping the width the same and increasing the length, the modulus E_1 is not affected while E_2 decreases. Figures 3.23 and 3.25 show that by keeping the sample length the same and increasing the width, both moduli E_1 and E_2 increase. This is because increasing the width would increase the number of clamped yarns, particularly the off-axis yarns.

For a fixed width of 6 unit cells, when the length increases from 6 to 24 unit cells, the aspect ratio L/W increases from 1 to 4. For a fixed length of 6 unit cells, when the width increases from 6 to 24 unit cells, the aspect ratio L/W decreases from 1 to ¼. The variations of E_1 and v_{12} with aspect ratio are shown in Figures 3.27 and 3.28. Variation of E_2 and v_{21} with aspect ratio are shown in Figures 3.29 and 3.30. Figures 3.27 to 3.30 show a kink in the curve and there are two property values for the same aspect ratio. These results are shown here to illustrate that there can be anomalies in the results for samples that are too short. When the sample is too short, the behavior is not representative and these samples should be avoided. The results obtained show that for meaningful results, the aspect ratio L/W should be at least 3.5.

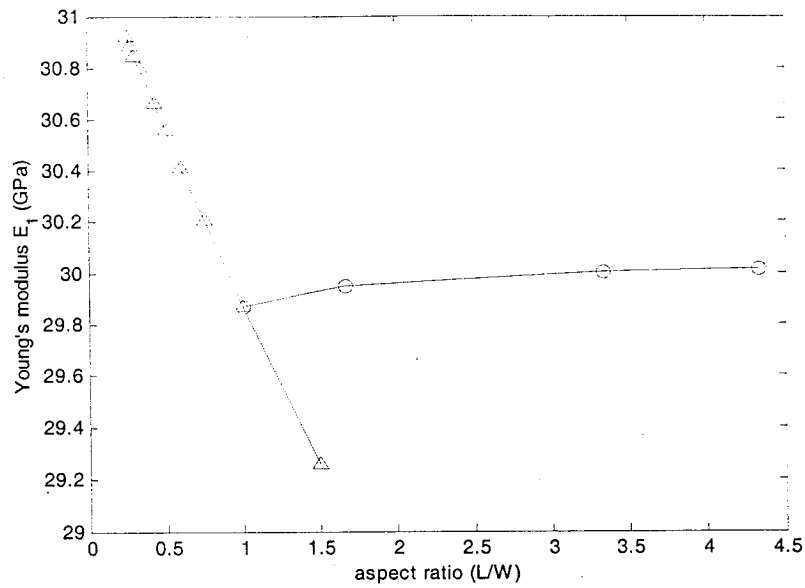

Figure 3.27: Effect of aspect ratio on Young's modulus E_1

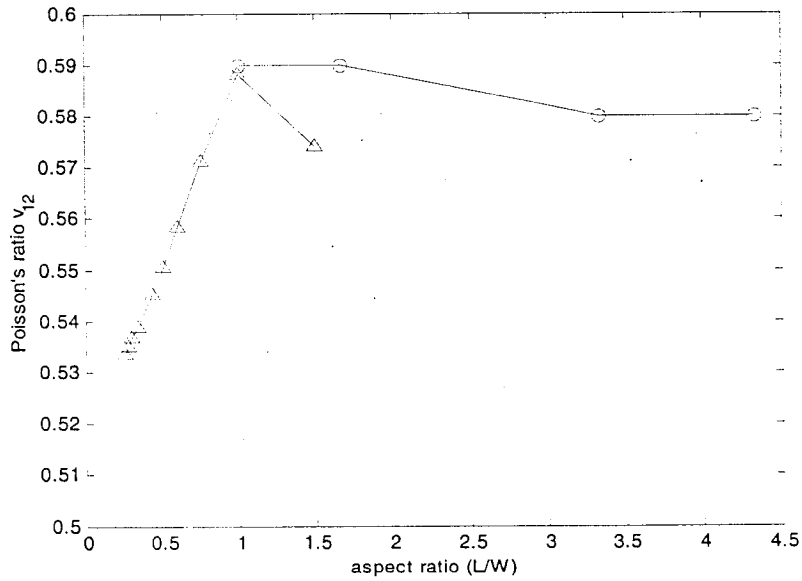

Figure 3.28: Effect of aspect ratio on Poisson's ratio v_{12}

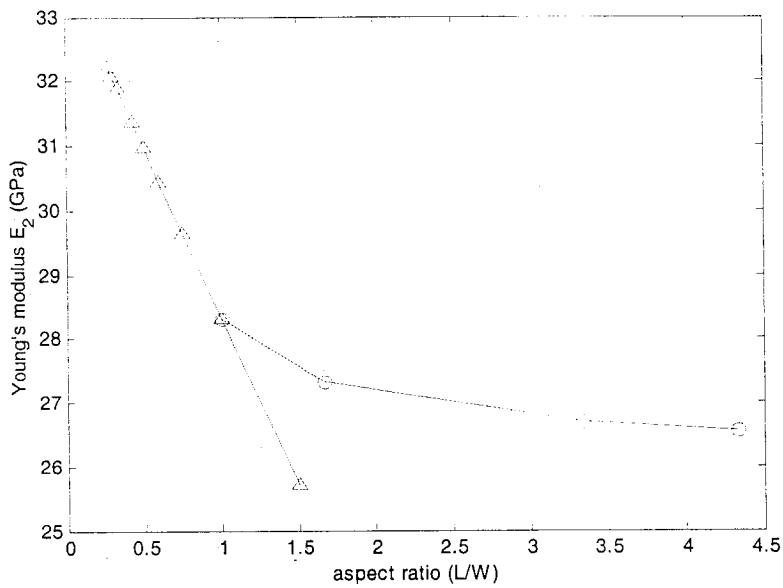

Figure 3.29: Effect of aspect ratio on Young's modulus E_2

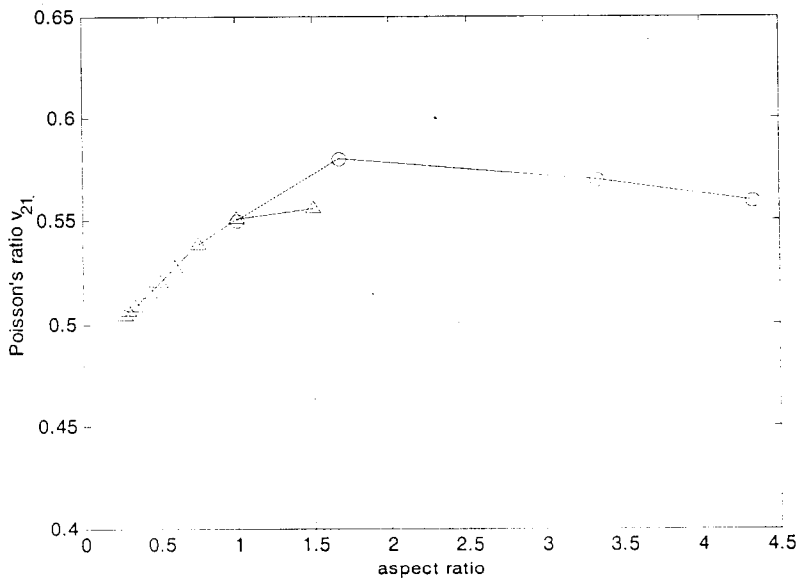

Figure 3.30: Effect of aspect ratio on Poisson's ratio v_{21}

3.2.4 Effects of panel size on elastic constants

Figure 3.7 shows that the size of a unit cell (superelement) is slightly more than 3 mm. A sample of width of 6 unit cells and length of 26 unit cells is about 22.65 mm by 71.6 mm. This size is small compared to actual dimension of a test specimen (about 50 mm by 300 mm). The effect of the size of sample on the elastic constant results is discussed here. TWF panels of certain aspect ratio with various sizes are investigated for two loading cases. For case 1, three panels of 26 by 6, 34 by 8, and 42 by 10 are chosen with close aspect ratios and their aspect ratios are 4.33, 4.25, and 4.2 respectively. For case 2, three panels of 6 by 26, 8 by 34, and 10 by 42 are selected and they have close aspect ratios, which are 4.33, 4.25, and 4.2 respectively. Table 3.13 shows the effects of panel size on Young's modulus E_1 and Poisson's ratio v_{12} in case 1. Table 3.14 shows the effects of panel size on Young's modulus E_2 and Poisson's ratio v_{21} in case 2. It is observed from Tables 3.13 and 3.14 that panel size has almost no effect on Poisson's ratios, provided that the size is at least 6 unit cells in width and the aspect ratio is more than 3.5. Panel size has more effect on the modulus E_2 than on the modulus E_1, but this effect is little. That means that the elastic properties are not sensitive to panel size.

Table 3.13: Effects of panel size on Young's modulus E_1 and Poisson's ratio v_{12} in case 1

Panel size	Aspect ratio (L/W)	Young's modulus E_1 (GPa)	Poisson's ratio v_{12}
26 by 6	4.33	30.010	0.58
34 by 8	4.25	30.259	0.59
42 by 10	4.20	30.403	0.59

Table 3.14: Effects of panel size on Young's modulus E_2 and Poisson's ratio v_{21} in case 2

Panel size	Aspect ratio (L/W)	Young's modulus E_2 (GPa)	Poisson's ratio v_{21}
6 by 26	4.33	26.550	0.56
8 by 34	4.25	27.671	0.57
10 by 42	4.20	28.320	0.58

3.2.5 Discussions

Boundary constraints affect the deformations of TWF panels in extension. At the area close to the boundaries, the transverse deformations of panels are resisted due to $w = 0$ at the boundaries. This effect is called the boundary resistance effect. This resistance makes Poisson's ratios at this area smaller than other areas of panels, as shown in Figures 3.14-3.17. This effect also contributes to increasing Young's modulus. As one moves away from the boundaries, this effect is reduced quickly. On the other hand, the boundaries make the yarns twisted during the extension of panels (see Figure 3.11). This effect is

called boundary twist effect. Twisting yarns contribute to the transverse deformation and Poisson's ratio of panels. For a short panel, the resistance effect plays a more dominant role. For a long panel, the twist effect is more dominant. This is why the curve in Figure 3.24 first goes up and then turns down.

3.3 Conclusions

In this chapter, a series of experiments were done to obtain the tensile elastic constants of the TWF composites. Finite element models (Superelement 1 and Superelement 2) developed in Chapter 1 for the TWF composites were also used to provide results for comparison with experiments. From the experimental and analytical results, Superelement 2 is better suited to predict the elastic properties of the TWF composite than Superelement 1. It is also clear that the finite elements provide a rigorous approach for the determination of elastic constants.

From the experiments, it can be seen that the TWF composites exhibit nonlinear behavior of stress-strain relation. The initial slope of the stress-strain curve is smaller than the slope at larger stress. That means at different loading levels, the TWF composites have different moduli. This can be explained by the structural adjustment during loading. This structural adjustment comes from the straightening of the undulation of the yarns. The yarns become stiffer as they are more and more straightened.

There are inherent limitations in the experimental approach. One limitation is the ability to account for the approximate thickness and width to be used for the extraction of the

elastic constants. It is not obvious which thickness and width should be used in the calculation of the cross section area. In this respect, the finite element modeling should provide more accurate results. The use of the laser extensometer certainly is a step forward from the use of strain gage. However, there is uncertainty in the measurement of the transverse strain due to the low value of the deformation and also due to the limitation of the resolution of the laser system.

The numerical results show that there is definitely an effect of the size of the sample on the elastic constants. These results indicate that an aspect ratio L/W of at least 3.5 should be used and sample size should have a width of at least 6 unit cells. Using these approaches, the elastic constants for this material system were found to be E_1 = 30 GPa, E_2 = 26.5 GPa, v_{12}=0.58 and v_{21}=0.56. These values may differ if one were to use different fibers, different yarn sizes and yarn spacings.

Chapter 4

Thermal Deformation Behavior of TWF Composites

In many demanding applications, including aerospace and automobile industries, one is interested in maintaining the shape of parts and lowering the mismatch between parts over a temperature range. So thermal deformation behavior of material is one of the most important mechanical properties of concern.

In this chapter, the thermal deformation behavior of TWF composites is modeled using Superelement 2 proposed previously. Thermal Expansion Coefficients (TECs) of TWF composites are evaluated. Effects of the aspect ratios and size of panels on the TECs are studied.

4.1 Finite element Model

The TWF composite is composed of three sets of yarns, which intersect and interlace with each other at 60^0 angles, as shown in Figure 4.1. The entire fabric can actually be obtained by assembling many unit cells. A unit cell is shown in Figure 4.2. The TWF

composite will have complex deformation status because of textile structure and material anisotropic characteristics. Even when the TWF composite is subjected to pure tension, the yarn will bear a combination of tensile, compression, bending and torsion. The pure and torsion shears will exist at the crossing areas between yarns and will play an important role in fabric failure.

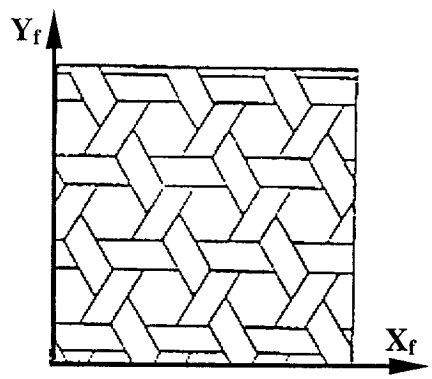

Figure 4.1: Triaxial woven fabric

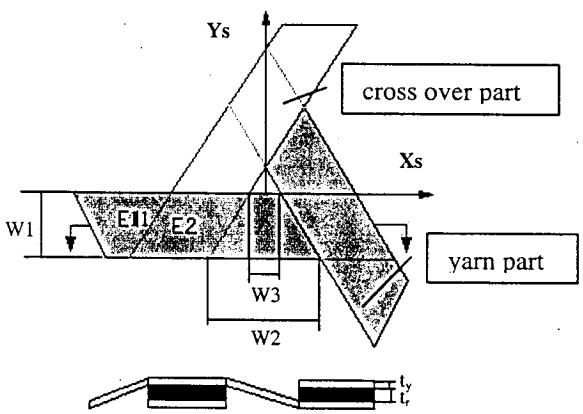

Figure 4.2: A unit cell (superelement)

In this chapter, thermal deformation of the TWF composites is investigated using

Superelement 2. Nodal forces of Superelement 2 due to thermal effects are formulated in this section. The thermal force vector of element E11 (as indicated in Figure 4.2) can be added into the force vector of Eq. (2.2.12) in Chapter 1. The thermal force vector of element E2 can be added into the force vector of Eq. (2.1.29) in Chapter 1. With these thermal force vectors, Superelement 2 can be used for thermal deformation analysis of TWF composites. Details of nodal forces of Superelement 2 due to thermal effects are presented below.

Formulas of elemental nodal forces due to thermal effects:

(1) Element E1 (single-layer element):

Virtual work due to thermal strain $\{\varepsilon_0\}$:

$$\{W_{Te1}\} = \int_v \delta\{\varepsilon\}^T\{\sigma_0\}dv = \int_v \delta\{\varepsilon\}^T[Q]\{\varepsilon_0\}dv = \delta\{d\}^T\left(\int_v [B]^T[Q]\{\varepsilon_0\}dv\right) \tag{4.1.1}$$

where $\{\varepsilon_0\}$ is thermal strain matrix and $\{d\}$ is nodal displacement vector.

Let $W_{Te1} = \delta\{d\}^T\{P_{Te1}\}$, the thermal force vector of element E11 can be given by

$$\{P_{Te1}\} = \int_v [B]^T[Q]\{\varepsilon_0\}dv \tag{4.1.2}$$

(2) Element E2 (three- layer element):

Virtual work due to thermal strain $\{\varepsilon_0\}$

$$\{W_{Tel}\} = \int_v \delta\{\varepsilon\}^T \{\sigma_0\} dv = \int_v \delta\{\varepsilon\}^T [Q]\{\varepsilon_0\} dv \tag{4.1.3}$$

Consider strain vector:

$$\{\varepsilon\} = \sum_{j=1}^{4} \{\varepsilon_j\} = \sum_{j=1}^{4} \{\overline{\Phi}_j\}\{\overline{U}_j\} = \sum_{j=1}^{4} \{\Phi_j\}[S]\{\Delta_j\} \tag{4.1.4}$$

where j is layer number of laminate element E2. Matrix $\{\Phi_j\}$ and [S] can be found in Chapter 2.

$$\{\overline{U}_j\} = \left[\frac{\partial U_j}{\partial x}, \frac{\partial V_j}{\partial y}, W_j, V_j, \frac{\partial W_j}{\partial y}, U_j, \frac{\partial W_j}{\partial x}, \frac{\partial U_j}{\partial y}, \frac{\partial V_j}{\partial x}\right]^T \tag{4.1.5}$$

$$\{\Delta_j\} = \left[u_j^1, u_j^2, u_j^3, u_j^4, v_j^1, v_j^2, v_j^3, v_j^4, w_j^1, w_j^2, w_j^3, w_j^4\right]^T \tag{4.1.6}$$

$$\{\overline{\Phi}_j\} = \begin{bmatrix} \Phi_j & 0 & 0 & 0 & 0 & 0 & 0 & 0 & 0 \\ 0 & \Phi_j & 0 & 0 & 0 & 0 & 0 & 0 & 0 \\ 0 & 0 & \frac{d\Phi_j}{dz} & 0 & 0 & 0 & 0 & 0 & 0 \\ 0 & 0 & 0 & \frac{d\Phi_j}{dz} & \Phi_j & 0 & 0 & 0 & 0 \\ 0 & 0 & 0 & 0 & 0 & \frac{d\Phi_j}{dz} & \Phi_j & 0 & 0 \\ 0 & 0 & 0 & 0 & 0 & 0 & 0 & \Phi_j & \Phi_j \end{bmatrix} \tag{4.1.7}$$

so that

$$\begin{aligned} \{W_{Tel}\} &= \sum_{j=1}^{4} \int_v \delta\{\Delta_j\}^T [S]^T [\overline{\Phi}_j]^T [Q]\{\varepsilon_0\} dv \\ &= \sum_{j=1}^{4} \int_\Omega \delta\{\Delta_j\}^T [S]^T \left(\int_{-\frac{h}{2}}^{\frac{h}{2}} [\overline{\Phi}_j]^T [Q]\{\varepsilon_0\} dz \right) d\Omega \end{aligned} \tag{4.1.8}$$

Let $\{\Delta\}=\begin{bmatrix}\Delta_1^T & \Delta_2^T & \Delta_3^T & \Delta_4^T\end{bmatrix}^T$, $W_{Te1}=\delta\{\Delta\}^T\{P_{Te1}\}$, the thermal force vector of element E2 can be given by

$$\{P_{Te1}\}=\begin{Bmatrix}\int_\Omega [S]^T\left(\int_{-\frac{h}{2}}^{\frac{h}{2}}[\overline{\Phi}_1]^T[Q]\{\varepsilon_0\}dz\right)d\Omega \\ \int_\Omega [S]^T\left(\int_{-\frac{h}{2}}^{\frac{h}{2}}[\overline{\Phi}_2]^T[Q]\{\varepsilon_0\}dz\right)d\Omega \\ \int_\Omega [S]^T\left(\int_{-\frac{h}{2}}^{\frac{h}{2}}[\overline{\Phi}_3]^T[Q]\{\varepsilon_0\}dz\right)d\Omega \\ \int_\Omega [S]^T\left(\int_{-\frac{h}{2}}^{\frac{h}{2}}[\overline{\Phi}_4]^T[Q]\{\varepsilon_0\}dz\right)d\Omega\end{Bmatrix} \tag{4.1.9}$$

4.2 Thermal deformation of TWF composites

In thermal deformation analysis, the following geometry and material properties of TWF composites are used. Table 4.1 lists the geometric parameters of the unit cell measured by checking the microscopic photographs of TWF composites. Table 4.3 shows the effective elastic properties of the impregnated yarn obtained by using the Strength-Of-Materials model (SOM) [73] and using fiber and matrix properties of Table 4.2 and the fiber volume fraction V_f = 0.695. Table 4.4 gives TECs of fibers and matrix of TWF composites. Table 4.5 gives the TECs of impregnated yarns of TWF composites obtained by using the Rule-Of- Mixtures model [73].

Table 4.1: Geometric Parameters

Geometric parameters	Measured values
Yarn thickness (mm)	0.07
w1 (mm)	0.85
w2 (mm)	1.10

Table 4.2: Elastic properties of fibers and matrix

Material	E_L (GPa)	E_T (GPa)	G_{LT} (GPa)	G_{TT} (GPa)	v_{LT}	ρ (gm/cm^3)
Carbon Fiber	500.0	40.0	24.0	14.3	0.26	2.10
Epoxy Resin	3.5	3.5	1.3	1.3	0.35	1.17

Table 4.3: Elastic properties of the impregnated yarn of TWF composites

Material	E_L (Gpa)	E_T (Gpa)	G_{LT} (Gpa)	v_{LT}	v_{TT}	V_f	ρ (gm/cm^3)
Carbon/epoxy	338.57	12.40	5.61	0.287	0.437	0.695	1.8164

Table 4.4: Thermal expansion coefficients of fibers and matrix

Material	α_L (ppm/^{0}C)	α_T (ppm/^{0}C)
Carbon Fiber	-0.7	10.0
Epoxy Resin	63.0	63.0

Table 4.5: Thermal expansion coefficients of the impregnated yarn of TWF composites

Material	α_L (ppm/^{0}C)	α_T (ppm/^{0}C)
Carbon/epoxy	-0.40	23.75

4.2.1 Thermal deformation

Thermal models

The thermal deformation of the TWF panel is investigated using four models. Each model consists of a rectangular panel. The size of the panel is determined by the number of unit cells shown in Figure 4.2 along each side of the rectangle. Each model has a different constraint condition. The reason for using these models is to investigate the effect of the different constraint conditions on the thermal behavior and also to determine the Thermal Expansion Coefficients (TEC) for the sample where applicable. It should be noted that many other constraint conditions were investigated but these could not provide useful information for the determination of the TEC. These four models are described as follows:

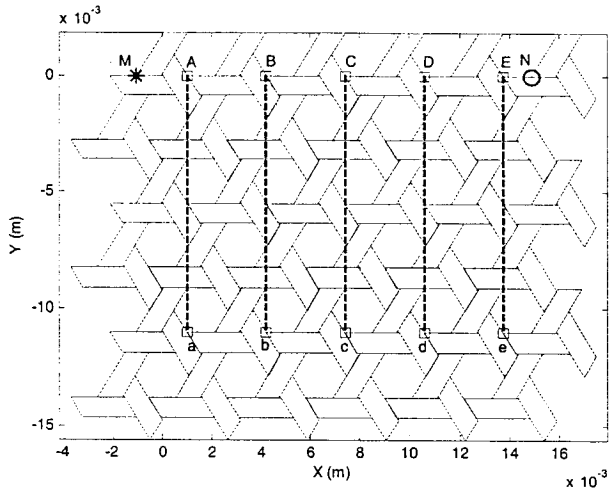

Figure 4.3: Model 1

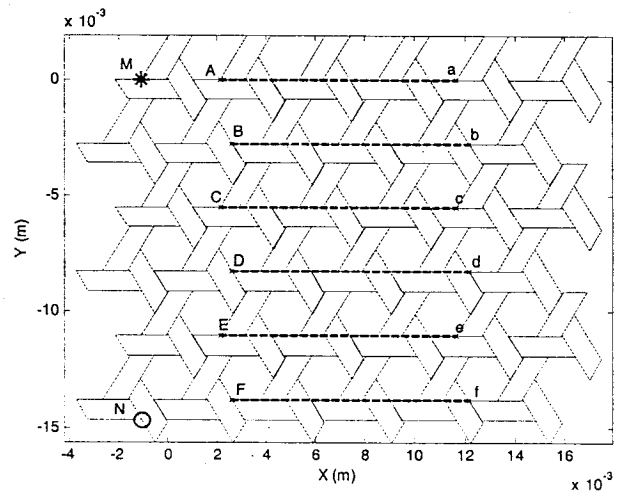

Figure 4.4: Model 2

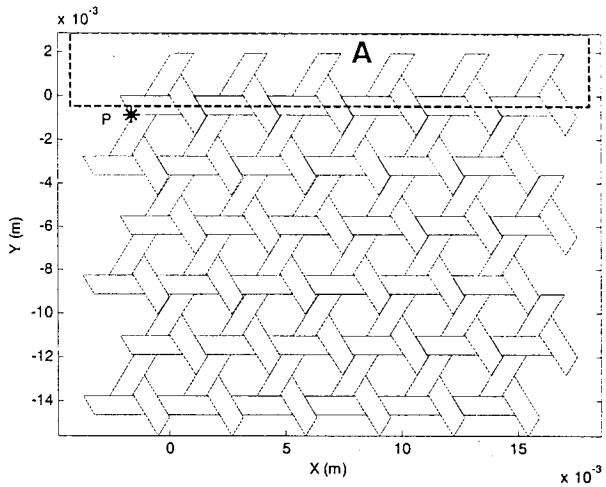

Figure 4.5: Model 3

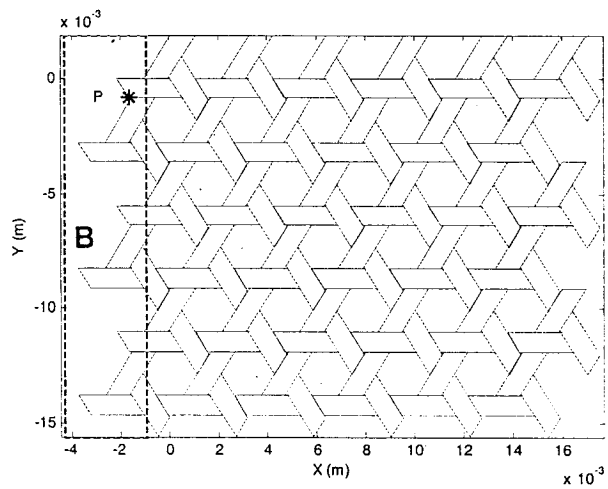

Figure 4.6: Model 4

Model 1:

For model 1 (Figure 4.3), a node (node M) at top left corner of the panel is fixed (u = v = w = 0), and at another node N of the top right corner of the panel, the displacements in Z and Y directions are set to zero (w = v = 0). This constraint condition fixes the two nodes along the direction of one tow and let the other nodes free. This model will be used to determine the TEC along the direction transverse to the tow direction (Y direction).

Model 2:

For model 2 (Figure 4.4), a node (node M) at top left corner of the panel is fixed (u = v = w = 0), and at another node O of the bottom left corner of the panel, the displacements in Z and X directions are set to zero (w = u = 0). This model fixes two nodes along the direction transverse to the tow direction. It will be used to determine the TEC along a direction parallel to a tow (X direction).

Model 3:

For model 3 (Figure 4.5), node P is fixed (u = v = w = 0) and v = w = 0 at all the nodes in area A of the panel. This constraint arrangement is similar to the case of Model 1 except that all points in region A are constrained (u = w = 0) rather than just one point. This model will be used to determine the deformation of the triax panel.

Model 4:

For model 4 (Figure 4.6), u = v = w = 0 at node P and u = w = 0 at all the nodes in area B of the panel. This model is similar to model 2 except that all points in region B are

constrained (u = w = 0) rather than just one point.

Samples of different sizes will be developed. Figures 4.3, 4.4, 4.5, and 4.6 show these four models for 6 by 6 panel respectively. Symbols '*' and 'o' represent the positions of two fixed nodes, u = v = w = 0 at node '*' and w = u = 0 at node 'o'.

Thermal deformation results:

Some products made of TWF composites, such as satellite antenna, need to work in a large temperature range from much lower than room temperature to much higher than room temperature. Hence it is necessary to investigate the thermal deformation behavior of TWF composites in this situation. For this calculation, we assume that the TECs of the fiber and resin stay the same through the thermal deformation process.

Figures 4.7 and 4.8 show the front and isometric views of the thermally deformed configuration of 6 by 14 panel (6 unit cells along the X direction and 14 unit cells along the Y direction) using Model 1. The temperature loading is an increment of 100 ^{0}C. The undeformed configuration of the panel is plotted in thin lines and the deformed configuration is plotted in thick lines. The panel is twisted as shown in Figure 4.7. In Figure 4.8, it is observed that the panel bends up and the left side of the panel bends more than the right side. The thermal deformation of the panel is a combination of extension, bending and twisting. Therefore, the panel has different TEC values at different locations.

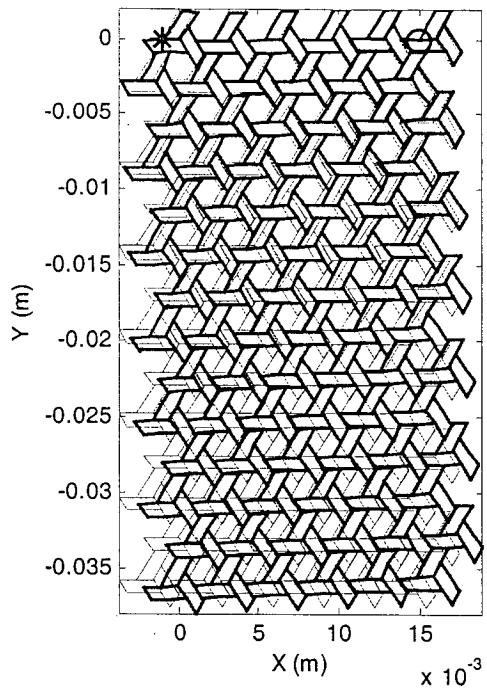

Figure 4.7: Thermally deformed configuration of 6 by 14 panel using Model 1 (Front)

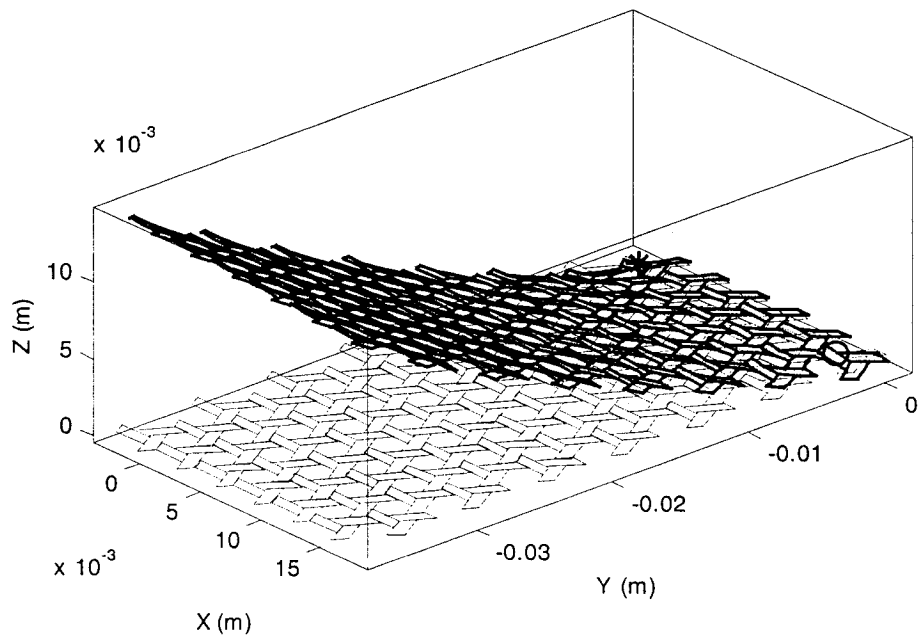

Figure 4.8: Thermally deformed configuration of 6 by 14 panel using Model 1

(Isometric)

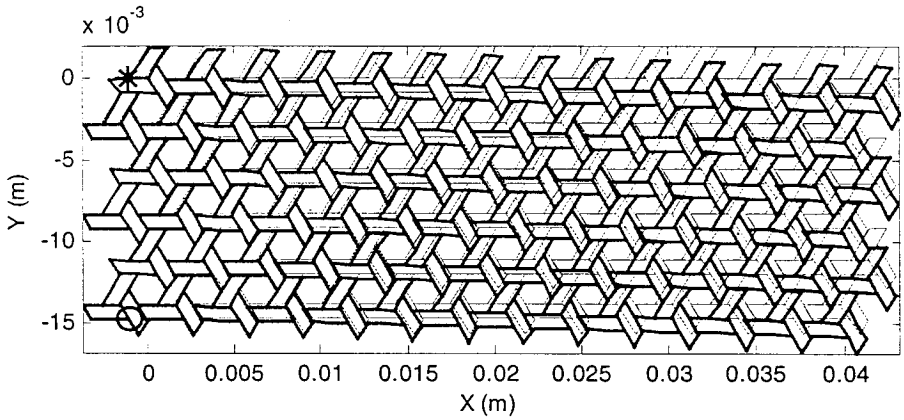

Figure 4.9: Thermally deformed configuration of 14 by 6 panel in Model 2 (Front)

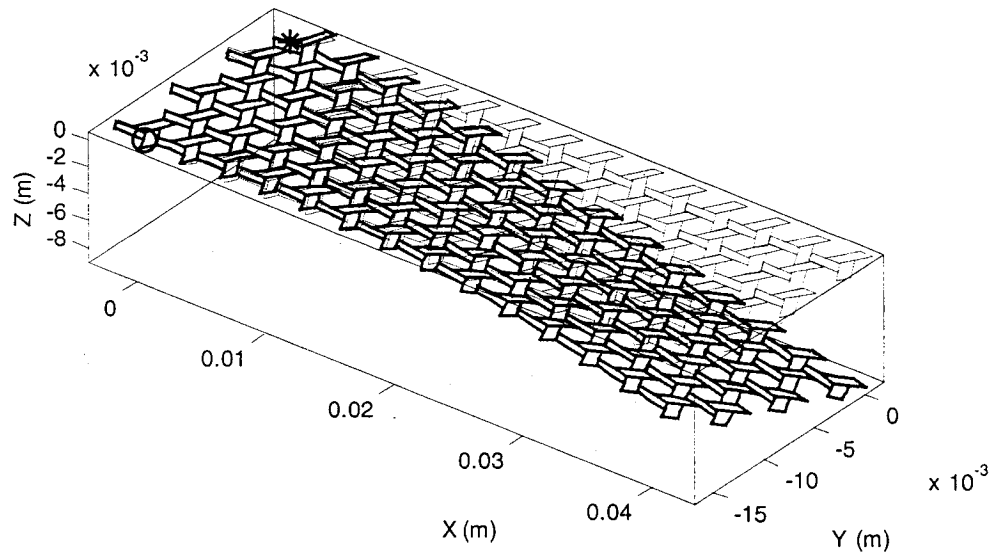

Figure 4.10: Thermally deformed configuration of 14 by 6 panel in Model 2 (Isometric)

Figure 4.9 shows the front view of the thermal deformed configuration of 14 by 6 panel in Model 2 due to the temperature increment of 100 ^{0}C. Figure 4.10 shows the isometric view. Different from Model 1 shown in Figures 4.7 and 4.8, the panel bends down as shown in Figures 4.9 and 4.10. The panel also has a twist.

Discussion:

The deformation behavior as shown in Figures 4.7 to 4.10 shows that the TWF is not symmetric. This may appear to be erroneous at first sight. However, close examination of the composition of the material along the thickness direction shows that indeed the material is not symmetric with respect to its mid plane. Figure 4.11 shows the configurations of four types of cross-sections of the TWF panel. The right hand side view shows two cross-sections of the panel along X direction, i.e., cross-sections C-C' and D-D'. From geometric viewpoint, these two sections are symmetric in thickness direction. But the top and bottom layers of three-layer parts have different material properties because the upper tow and lower tow have different fiber orientations. Hence the TWF panel is, in effect, unsymmetrical in thickness direction along X direction. This will lead the panel to bending along X direction due to thermal loading. The bottom view shows two cross-sections A-A' and B-B' along Y direction. The section A-A' is symmetric in geometry but unsymmetrical in material properties. The section B-B' is unsymmetrical in thickness direction because both geometry and material properties are not symmetric in thickness direction. Therefore, the TWF panel is also unsymmetrical in thickness direction along Y direction. The panel will also bend along Y direction subjected to

thermal loading. This is why the panel will bend due to thermal loading.

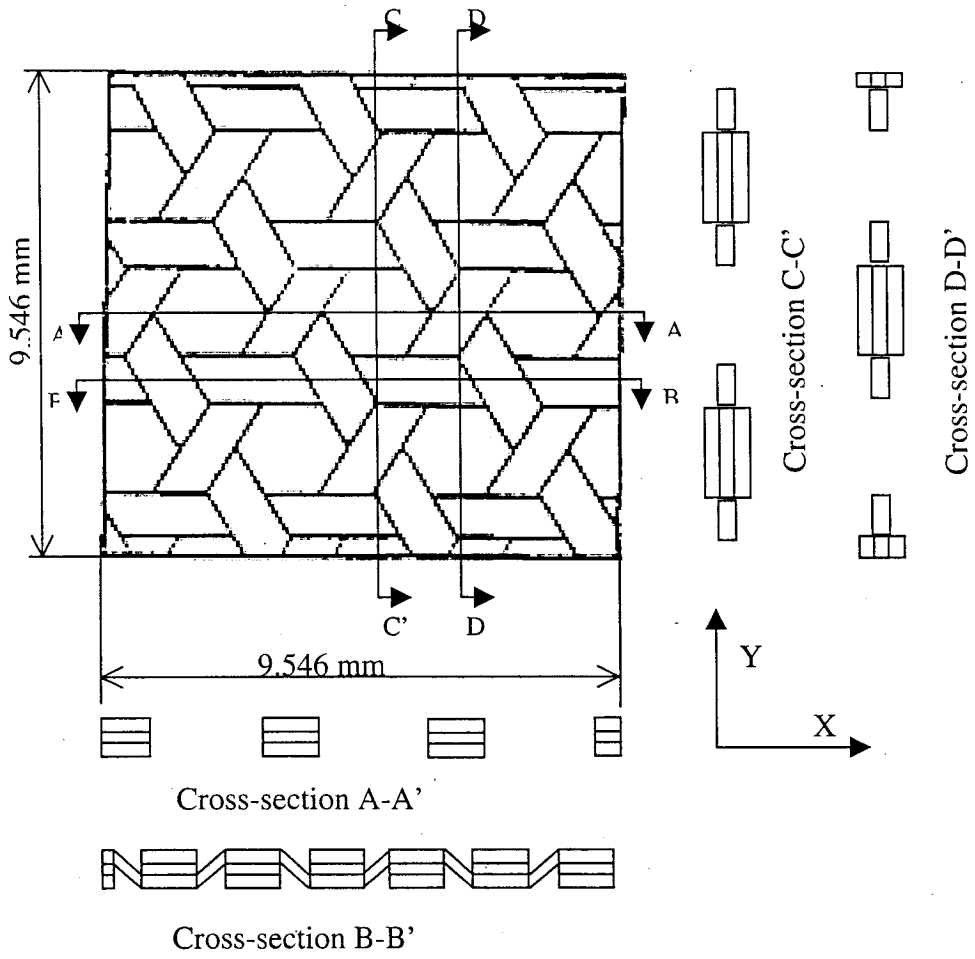

Figure 4.11: Cross sections of triaxial woven fabric composites

Effect of different constraint conditions:

The following presents the thermal deformation of the panels subject to the constraint conditions in Model 3 and Model 4.

Figure 4.12 shows the front view of the deformed configuration of 6 by 14 panel due to

increments of 100 ^{0}C and –100 ^{0}C. Figure 4.13 shows the isometric view. Figures 4.14 and 4.15 show the views along –Y direction and along –X direction respectively. Thin lines show the un-deformed configuration of the panel at room temperature. Dashed lines show the deformed configuration of the panel due to the temperature increment of 100 ^{0}C. Thick lines show the deformed configuration of the panel due to the temperature increment of –100 ^{0}C. Due to the temperature increment of 100 ^{0}C, the panel bends upward and the end of the panel deflects to 0.012 m on the right side and to 0.014 m on the left side as shown in Figures 4.10 and 4.12. The left side of the panel deflects more than the right side (Figure 4.14). The panel twists a little to right side as shown in Figures 4.12 and 4.14. For the temperature increment of –100 ^{0}C, the panel bends downward as shown in Figure 4.13 and the panel end reaches the deflection of –0.012 m to –0.014 m. The panel twists a little to left side as shown in Figures 4.12 and 4.14.

It can be seen that the mode of deformation of the TWF is similar when using either Model 1 or Model 3. However, the magnitudes of the deformation are different for each model. The above presentation shows that the thermal deformation is different for each constraint condition. The calculation for the TEC will be based on the constraint condition that gives the lesser amount of constraint (Model 1 as compared to Model 3). Model 1 will therefore be used to determine the TEC of the TWF in a later section.

Figure 4.16 shows the front view of the deformed configuration of 14 by 6 panel due to temperature increments of 100 ^{0}C and –100 ^{0}C in Model 4. Figure 4.17 shows the isometric view. Figures 4.18 and 4.19 show the views along –Y direction and along –X direction respectively. Different from Model 3 as shown in Figure 4.12, the panel bends

downward with a temperature increment of +100 ^{0}C and reaches the deflection of –0.007 m to –0.014 m (the right side of the panel deflects more than the left side), as shown in Figure 4.18. For an increment of –100 ^{0}C, the panel bends upward and has the deflection of 0.007 m to – 0.014 m (the right side of the panel also deflects more than the left side). Similar to the argument made before, Model 2 will be used to determine the TEC along the X direction.

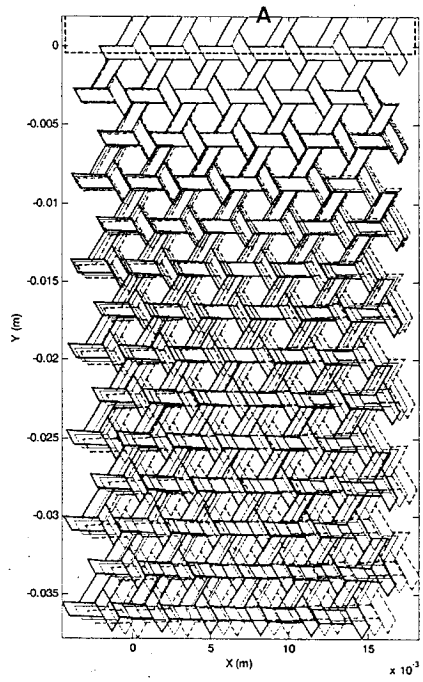

Figure 4.12: Thermally deformed configuration of 6 by 14 panel in Model 3 (Front)

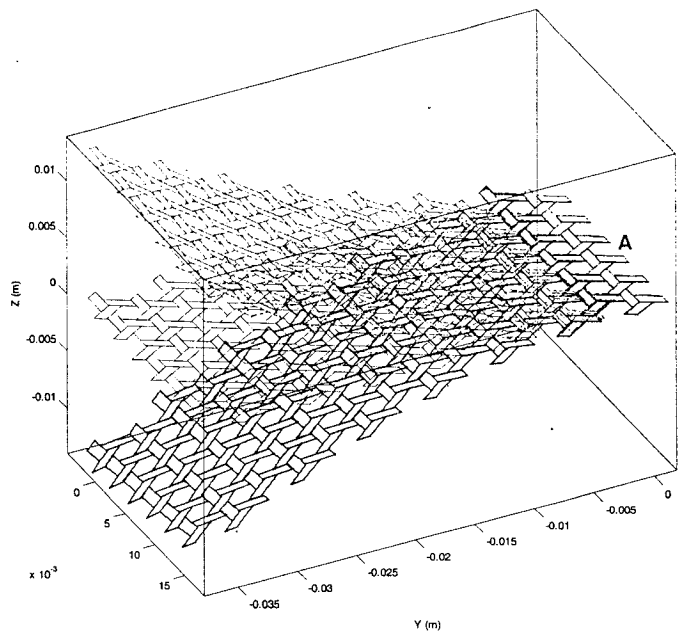

Figure 4.13: Thermally deformed configuration of 6 by 14 panel in Model 3 (Isometric)

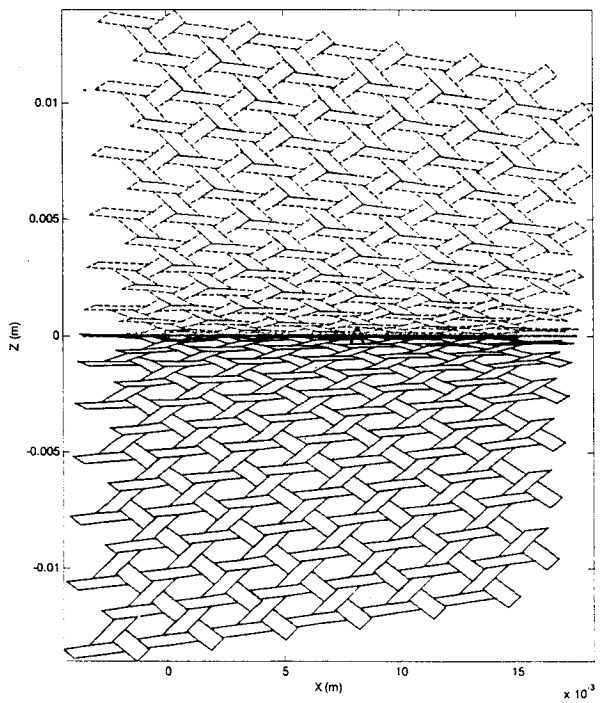

Figure 4.14: Thermally deformed configuration of 6 by 14 panel in Model 3

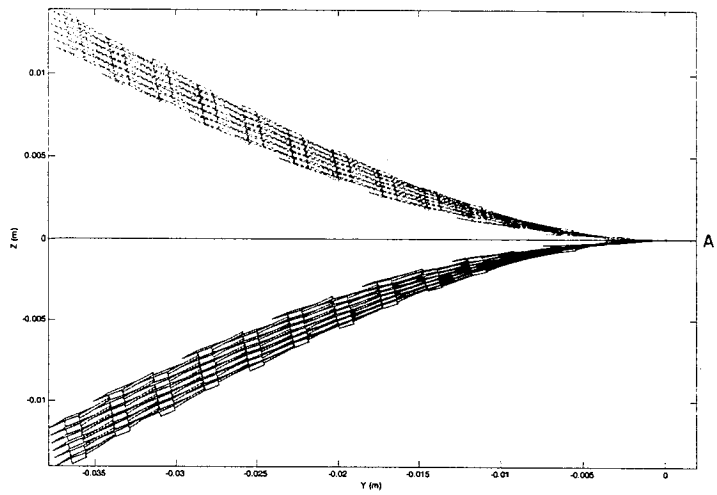

Figure 4.15: Thermally deformed configuration of 6 by 14 panel in Model 3 (view along –X direction)

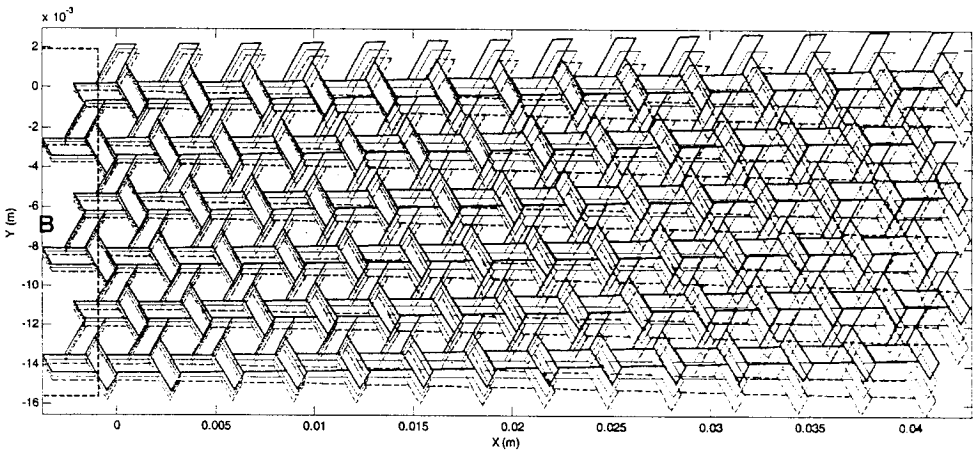

Figure 4.16: Thermally deformed configuration of 14 by 6 panel in Model 4 (Front)

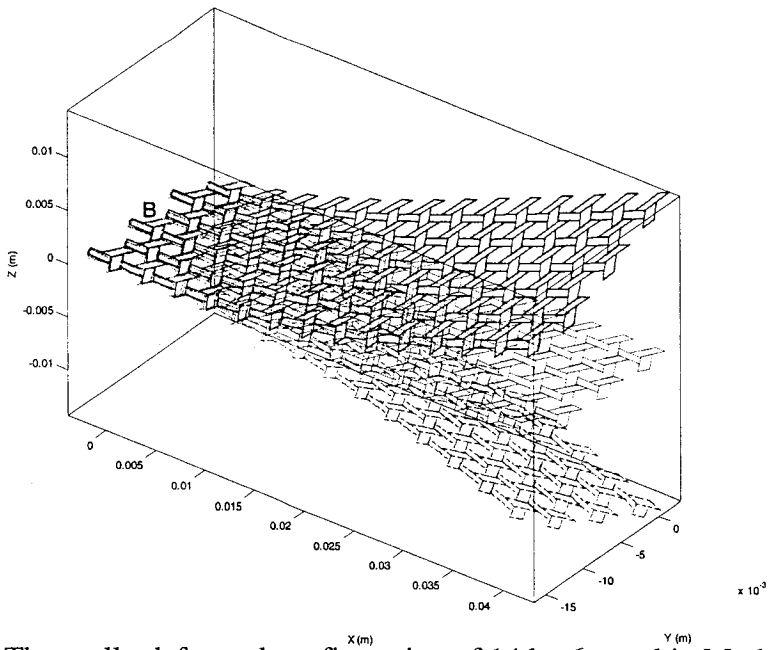

Figure 4.17: Thermally deformed configuration of 14 by 6 panel in Model 4 (Isometric)

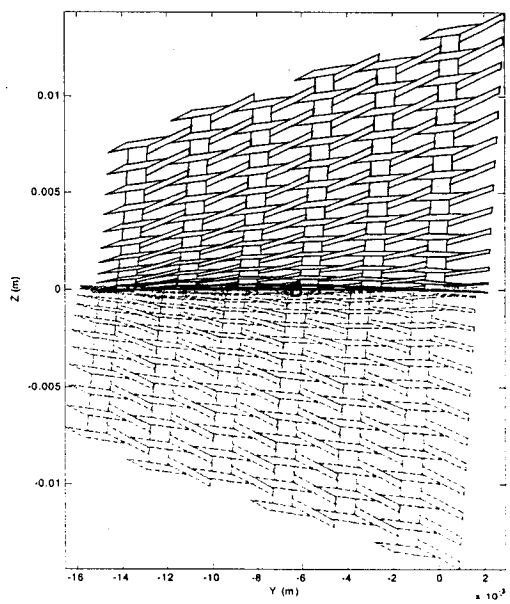

Figure 4.18: Thermally deformed configuration of 6 by 14 panel in Model 4

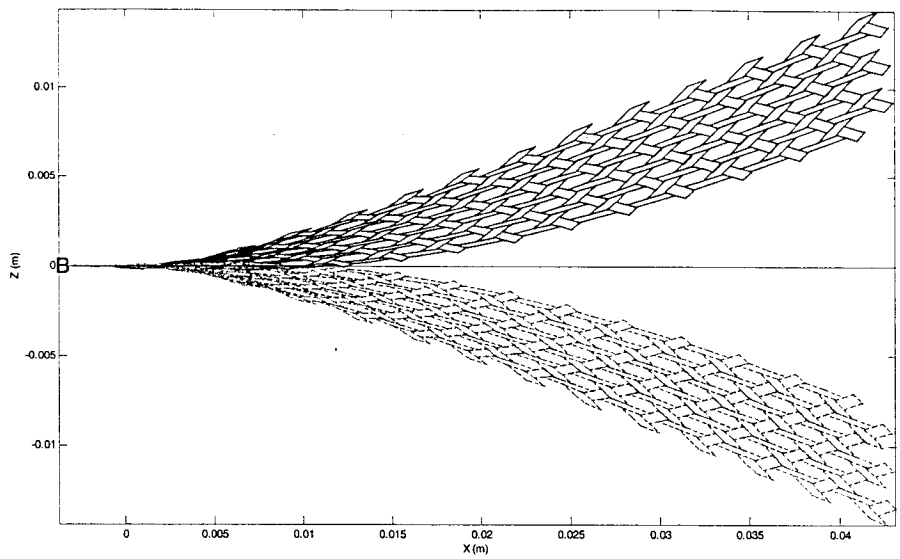

Figure 4.19: Thermally deformed configuration of 6 by 14 panel in Model 4

4.2.2 Apparent Thermal Expansion Coefficients (TECs) of TWF composites

In this section, TECs of TWF composites are calculated using the thermal deformation model. The apparent thermal expansion coefficient is defined to be similar to the regular thermal expansion of conventional material. The two models (models 1 and 2) are considered, as shown in Figures 4.3 and 4.4 for an example of 6 by 6 panel. Model 1 is used for calculating the Y direction TECs. Model 2 is used for calculating the TEC along the X direction.

For evaluating TEC in Y direction, the strain in Y direction is determined between two points denoted by '□' and linked with a dashed line, as shown in Figure 4.3. The strain in Y direction is given by

$$\varepsilon_y = \frac{\Delta v}{L}$$

where Δv is the increment of displacements at the two points in Y direction. L is the distance between the two points. For an example of 6 by 6 panel, as shown in Figure 4.3, there are totally five pairs of points (Aa, Bb, Cc, Dd and Ee). The five strains in Y direction can be determined as follows

$$\varepsilon_{yAa} = \frac{v_A - v_a}{L_{Aa}},\quad \varepsilon_{yBb} = \frac{v_B - v_b}{L_{Bb}},\quad \varepsilon_{yCc} = \frac{v_C - v_c}{L_{Cc}},\quad \varepsilon_{yDd} = \frac{v_D - v_d}{L_{Dd}},\quad \varepsilon_{yEe} = \frac{v_E - v_e}{L_{Ee}}$$

With these five strains, corresponding five TECs of 6 by 6 panel in Y direction can be determined by

$$\alpha_i = \varepsilon_i / \Delta T \qquad (i = yAa,\ yBb,\ yCc,\ yDd,\ yEe)$$

where ΔT is temperature change. The Y direction TECs of other panels can be determined in the same way.

In Figure 4.4, two points denoted by 'x' and linked with a dashed line are used for the strain and TEC in X direction. The strain in X direction is given by

$$\varepsilon_x = \frac{\Delta u}{L}$$

where Δu is the increment of displacements at the two points in X direction. L is the distance between the two points. For an example of 6 by 6 panel in Model 2, as shown in Figure 4.4, there are totally 6 pairs of points (Aa, Bb, Cc, Dd, Ee and Ff). The corresponding six strains in Y direction can be determined as follows

$$\varepsilon_{xAa} = \frac{u_A - u_a}{L_{Aa}}, \quad \varepsilon_{xBb} = \frac{u_B - u_b}{L_{Bb}}, \quad \cdots\cdots, \quad \varepsilon_{xFf} = \frac{u_F - u_f}{L_{Ff}}$$

where u_i is average displacement in X direction at point i.

With these five strains, corresponding six TECs of 6 by 6 panel in X direction can be determined by

$$\alpha_i = \varepsilon_i / \Delta T \qquad (i = xAa,\ xBb,\ xCc,\ xDd,\ xEe,\ xFf)$$

where ΔT is temperature change. The X direction TECs of other panels can be also determined in the same way.

Model 1

First consider Model 1. The Y direction TECs at different locations of a panel are investigated. The TECs of square panels with different sizes are compared. Figure 4.20 shows the Y direction TECs at different locations for the square panels of 8 by 8, 10 by 10, 12 by 12, 14 by 14, and 16 by 16. In Figure 4.20, it is observed that the Y direction TEC values at two sides of the panels are different, as seen previously in Figure 4.7. As the size of the panels increases, the Y direction TECs at the left side become larger while the Y directions TECs at the right side become smaller. The center parts of these curves remain approximately constant. This value may be taken to be the Y direction TEC since it seems to be unaffected by the size of the panel. It has the value of $\alpha_y \approx -4.8\times10^{-6}\ {}^0C^{-1}$.

Figure 4.21 shows the Y direction TECs at different locations of the panels of 8 by 8, 8

by 10, 8 by 12 and 8 by 14 using Model 1. It is observed that aspect ratios of panels have effects on the Y direction TECs. The 8 by 8 panel has almost the same TEC at its central area. For the panel of 8 by n_y (n_y = 8,10,12,·····), when n_y is greater than 8, the Y direction TEC of the left side part is greater than the one of 8 by 8 panel and the Y direction TEC of the right side part is less than the one of 8 by 8 panel. These curves also go through a common point. At this point, the Y direction TEC $\alpha_y \approx -4.8\times10^{-6}\ {}^0C^{-1}$, which can be considered as the representative Y direction TEC of panels of 8 by n_y (n_y=8,10, ·····).

The same situation is also observed for other panels. For the panel of m by m (m=6, 8, 10, ·····), the panel has almost the same TEC at its central area. For panel m by n_y (n_y = 6,8,10, ·····), when n_y is greater than m, the Y direction TEC of the left side part is greater than the one of m by m panel and the Y direction TEC of the right side part is less than the one of m by m panel. In addition, these curves go through a common point, at which the Y direction TEC is the representative value of the Y dimension TECs of the panel and that is unaffected by the dimension of the panel in Y direction. It is important that these representative Y direction TECs of the panel of any width are very close, as shown in Figure 4.20. Therefore, we can conclude the equivalent Y direction TEC of panels $\alpha_y \approx -4.8\times10^{-6}\ {}^0C^{-1}$. With the Y direction TEC and panel aspect ratio, the thermal deformed configuration and the Y direction TEC of panel can be evaluated approximately.

Model 2

Model 2, as shown in Figure 4.4, is used for the X direction TECs of panels. The effects

of panel length (X direction dimension) or aspect ratio on TECs of panels are investigated. Figure 4.22 shows the X direction TECs at different locations of the panels of 6 by 20, 8 by 20, 10 by 20 and 12 by 20 respectively. It is observed from Figure 4.22 that these curves coincide with each other at the centre part. That means that there is little effect of panel length or aspect ratio on TECs of centre parts of panels. From the centre part of these curves, we can obtain the mean value of X direction TECs $\alpha_x \approx -6\times10^{-6}$ $^0C^{-1}$. It can be considered as the equivalent X direction TEC of panels.

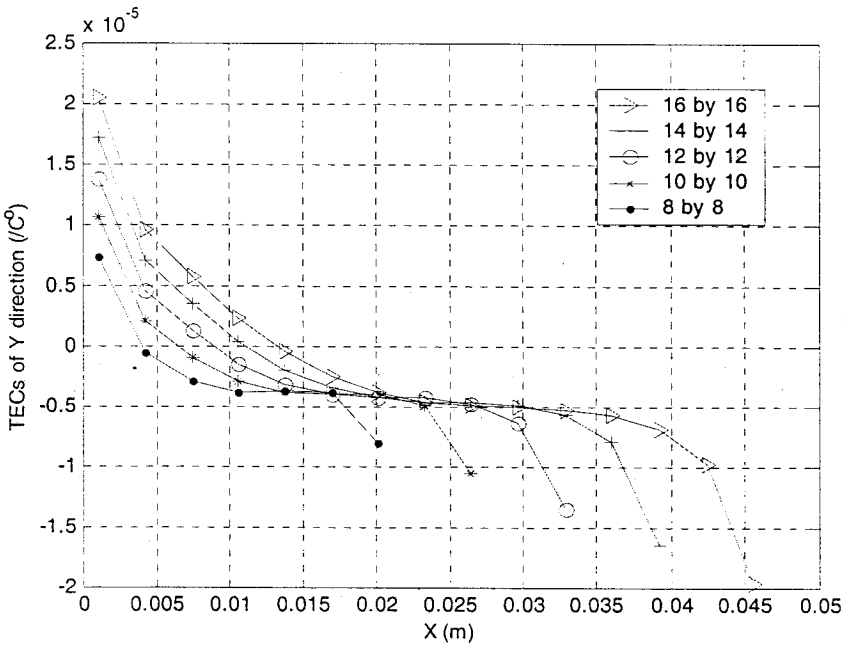

Figure 4.20: Y direction TECs of square panels in Model 1

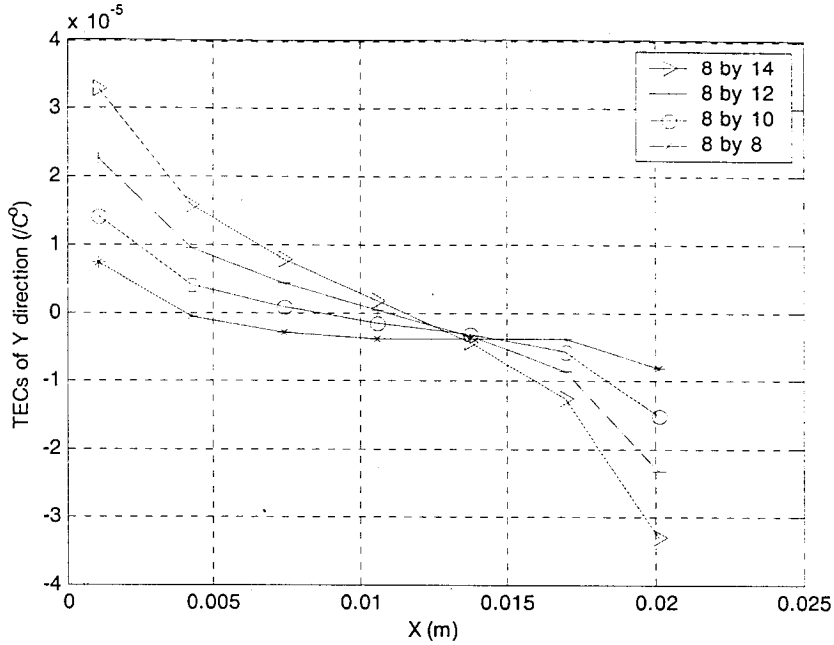

Figure 4.21: Y direction TECs of panels of 8 by n_y in Model 1

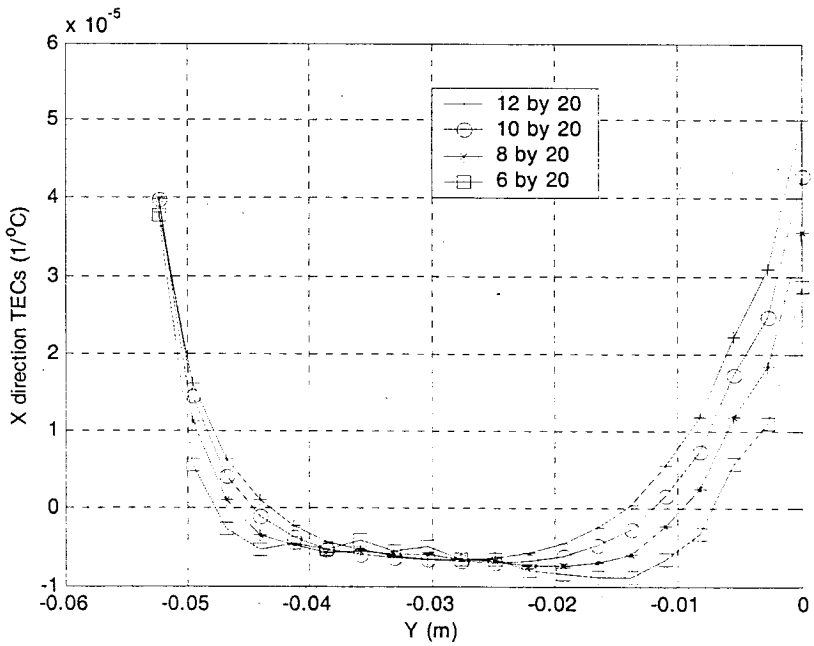

Figure 4.22: X direction TECs of panels of n_x by 20 in Model 2

Discussion:

If one were to take the constant values in Figures 4.20 and 4.22 to be the representative TEC values for the triax, then we have α_x = -6.0 x 10^{-6}/°C, and α_y = -4.8 x 10^{-6} /°C. Both of these values are negative. The reason for this is because the coefficient of expansion of the tow is negative. Both the contraction along the x and y direction are larger than the contraction of a tow (-0.4 x 10-6/oC). This is due to the bending effect of the triax.

4.2.3 Thermal deflection of TWF composites in Z direction

As can be seen from previous discussion and also from Figures 4.8 and 4.10, TWF panels bend when they are subjected to a temperature increment. The amount of bending depends on the size of the panel and also on the boundary conditions. However it would be convenient to define some coefficient to characterize this behavior, and also to obtain some values for the characterization of the behavior of the TWF panels. In this section, the deflections of the panels with Model 4 due to the temperature increment of 100 ^{0}C are studied. Figure 4.23 shows an example of 6 by 6 panel with model 4. At all the nodes at region B, displacements u and w are imposed to be zero (u = w = 0), and u = v = w = 0 at node P. Node P is located with the symbol '*' in Figure 4.23. For an example of 6 by 6 panel, there are 6 pairs of points (Aa, Bb, Cc, Dd, Ee, Ff). Each pair of points is used to calculate deflection. For instance, the deflection of 6 by 6 panel at line Aa is obtained by calculating the difference of Z direction displacements between points a and A as:

$$W_{aA} = W_a - W_A \qquad (4.2.1)$$

By averaging the deflections at these six lines, we can obtain the average deflection W_m of 6 by 6 panel. The average deflections of other panels can also be calculated in the same way.

Table 4.6 gives the average deflections of panels of n_x by n_y (n_x, n_y = 6, 8, 10, 12, 14) in Model 4 due to the temperature increment of 100 ^{0}C. L_x is the average distance between the pairs of points. From Table 4.6, it is observed that increasing the dimension of the panel in Y direction (i.e., increasing n_y) affects the average deflections of the panels very little, only by 0.8%. Hence, the effect of n_y on the average deflections of the panels may be neglected. We only need to consider the panels of n_x by 6 and to investigate the effect of n_x on the average deflections of these panels. Defining a new parameter β, called the bending thermal coefficient as the average deflection W_m divided by L_x^2, i.e.,

$$\beta = W_m / L_x^2 \tag{4.2.2}$$

Values of parameters β are plotted against the number of superelements along X direction n_x in Figure 4.24. It can be seen that β value varies linearly with the number of superelements n_x. From this observation, we can propose the following engineering formula to evaluate the average deflections of any sized panels in Model 4 due to thermal effects.

$$W_m = -(pn_x + q)L_x^2 \Delta T \qquad (n_x, n_y \geq 6) \tag{4.2.3}$$

where W_m is the average deflection of the panel of n_x by n_y due to the temperature increment of 1 ^{0}C. ΔT is the temperature increment (^{0}C). p and q are the material

constants. For this particular study, p and q have values of -4.375×10^{-3} and 1.250×10^{-3} respectively.

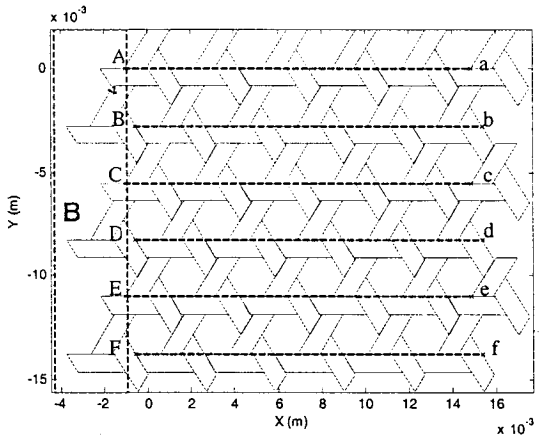

Figure 4.23: Model 4

Table 4.6: Average deflections of panels of various aspect ratios in Model 4

n_x	L_x (m)	n_x by 6 (m)	n_x by 8 (m)	n_x by 10 (m)	n_x by 12 (m)	n_x by 14 (m)
6	1.5907×10^{-2}	-6.3894×10^{-4}	-6.3787×10^{-4}	-6.3632×10^{-4}	-6.3493×10^{-4}	-6.3378×10^{-4}
8	2.2270×10^{-2}	-1.6840×10^{-3}	-1.6811×10^{-3}	-1.6772×10^{-3}	-1.6736×10^{-3}	-1.6705×10^{-3}
10	2.8633×10^{-2}	-3.4971×10^{-3}	-3.4903×10^{-3}	-3.4823×10^{-3}	-3.4751×10^{-3}	-3.4688×10^{-3}
12	3.4996×10^{-2}	-6.2906×10^{-3}	-6.2767×10^{-3}	-6.2620×10^{-3}	-6.2491×10^{-3}	-6.2380×10^{-3}
14	4.1359×10^{-2}	-1.0278×10^{-2}	-1.0252×10^{-2}	-1.0227×10^{-2}	-1.0206×10^{-2}	-1.0188×10^{-2}

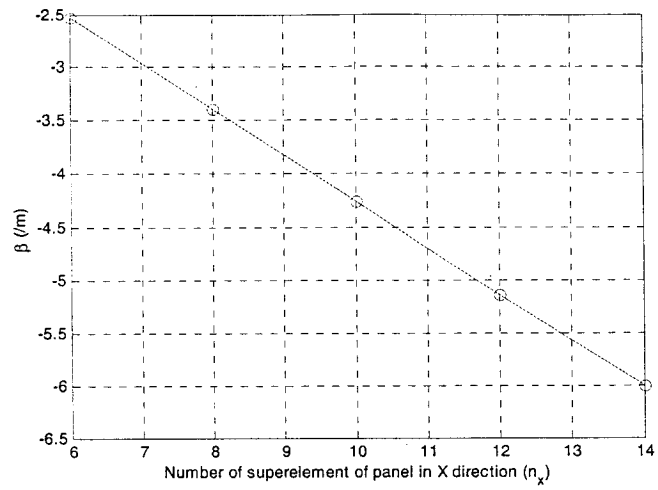

Figure 4.24: Parameter β versus n_x

4.3 Conclusions

The thermal deformation behavior of TWF composites was studied using finite element model (Superelement 2). It is demonstrated that the TWF composites are a special woven structure with holes and without any symmetric planes. Therefore the material bends and twists in addition to expansion or contraction when subjected to thermal loading. As such it is difficult to characterize the Thermal Expansion Coefficient for the material.

It is also difficult to find suitable boundary constraints for the finite element models so that the effect of the size of the panels does not enter into the analysis. Many different constraint conditions were attempted. A few constraint conditions were found where the size effect of the panel was minimized. These constraint conditions were used to

determine the thermal deformation behavior of the triax composites. It was found out that the apparent Thermal Expansion Coefficients remain constant within a certain region of the panel. These may be taken to be the representative TEC for the material.

With the above understanding, the following conclusions can be made:

1) The TWF composites are not symmetric in thickness direction. Hence, their thermal deformation includes bending besides contraction (expansion), shear, and twist.

2) For the square panel of m by m (m=6, 8, 10, ·····), the panel has almost the same Y direction TECs at its central area. For the panel of m by n_y (n_y = 6,8,10, ·····), when n_y is greater than m, the Y direction TEC on the left side of the panel is greater than the Y direction TEC of the right side. In addition, the TEC curves go through a common point, at which the Y direction TEC may be taken to be the representative value of the Y dimension TECs of the panel ($\alpha_y \approx -4.8\times10^{-6}\ ^0C^{-1}$).

3) The apparent X direction TEC of panels is $\alpha_x \approx -6\times10^{-6}\ ^0C^{-1}$.

4) The average out-of-plane deflection (deflection in Z direction) of the panels divided by L_x^2 is found to vary linearly with the dimension of the panels in X direction (n_x). An engineering formula (Eq. 4.2.3) is proposed for evaluating the average Z direction deflections of any sized panels in Model 4 due to thermal effects.

Chapter 5

Finite Element Modeling of a Membrane Sector of a Satellite Reflector

Due to their extremely light weight with good stiffness and strength, single layers of triaxial woven fabric composites have been used to make communication satellite reflectors. Special super-finite elements have been developed for the analysis of these lightweight materials. These super-finite elements are used for the deflection and stress analysis of a membrane sector of the satellite reflector subjected to lateral pressure. Due to the significant difference in the size of the satellite structure (order of meters) and the size of the super-finite elements (order of millimeters) it was not possible to model the satellite structure using the super-finite elements and computer facilities available in most labs (personal computers). In the process of finding a solution to this problem, a special similitude behavior for the deflection of the curved panels made of triaxial fabrics was discovered. Using this behavior, the deflection of a large size reflector panel (order of meters) can be analyzed using models in the millimeters size range. Stresses in the triax reflector model were also calculated. However, no special similitude behavior was obtained for the stresses.

5.1 Introduction

Communication satellite dishes incorporate a parabolic or circular curve into the design of their bowl-shaped reflectors. The parabolic curve has the property of reflecting all incident rays arriving along the reflector's axis of symmetry to a common focus located at the front and center. The parabolic antenna's ability to amplify signals is primarily governed by the accuracy of this parabolic curve. The spherical antenna creates multiple focal points located at the front and center of the reflector, one for each available satellite. The curvature of the reflector is such that if extended outward far enough along both axes it would become a sphere.

The ART EM reflector is a mesh spherical antenna of the communication satellite [74]. It is constructed of ribs and membrane surface, as shown in Figure 5.1. The membrane surface is a part of a spherical surface between two inner and outer circles. The sphere radius is about 2820 mm. Its outer perimeter diameter is about 1450 mm and inner perimeter diameter is about 508 mm. The entire membrane is divided uniformly into 12 sectors by ribs. Each membrane sector is a 30^0 degrees angle part of the spherical surface. Figure 5.2 shows detailed reflector dimensions. Compared with ribs, the membrane sector is a very weak load-bearing structural part. It is necessary to investigate its mechanical behavior.

The ribs and membrane surface of the ART EM reflector is made of the triaxial woven fabric (TWF) composites. The reason for this construction is due to lightweight, and also due to the facility to allow air to escape through the holes during launching. This air

escape reduces significantly the air impact, which significantly reduces the loading on the structure.

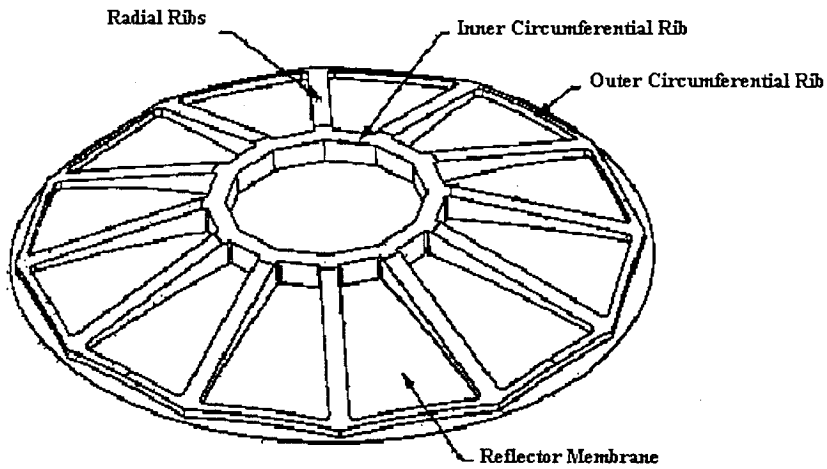

Figure 5.1: EM reflector bottom view

The TWF composite is a woven fabric. It is composed of three sets of yarns, which intersect and interlace with each other at 60^0 angles. Figures 5.3 and 5.4 show the schematic of the single layered triaxial woven fabric structure and also a representative unit cell. The thickness of a tow (yarn) is 0.14 mm. The width w_1 is about 0.85 mm. The distance w_2 is about 1.10 mm. This gives the total side dimension of a cell of about 3 mm. The presence of holes in the structure presents special challenge for the analysis of these triax structures.

One approach to this problem would be to obtain average properties of a representative unit cell in the structure and use these properties for the analysis of the whole structure. There are a variety of analyses for analyzing plain-weave composites. These differ in

both geometric approximation and assumption about stress and strain distribution. Many of these are concerned with the micro-mechanics, stiffness averaging, and homogenization [75]. Following similar approach, a previous investigation using equivalent energy principle was made where averaged properties of a representative unit cell of a single layer of triax were obtained [76]. A comprehensive survey of the different techniques for the homogenization of the microstructure was also given in reference [76]. The results obtained give upper bounds and lower bounds for the moduli and Poisson ratios. Compared with experimental values the upper bound of the Young's modulus show reasonable agreement but the shear moduli did not show good agreement. Also these averaging procedures cannot provide facilities to calculate the stresses required for strength prediction.

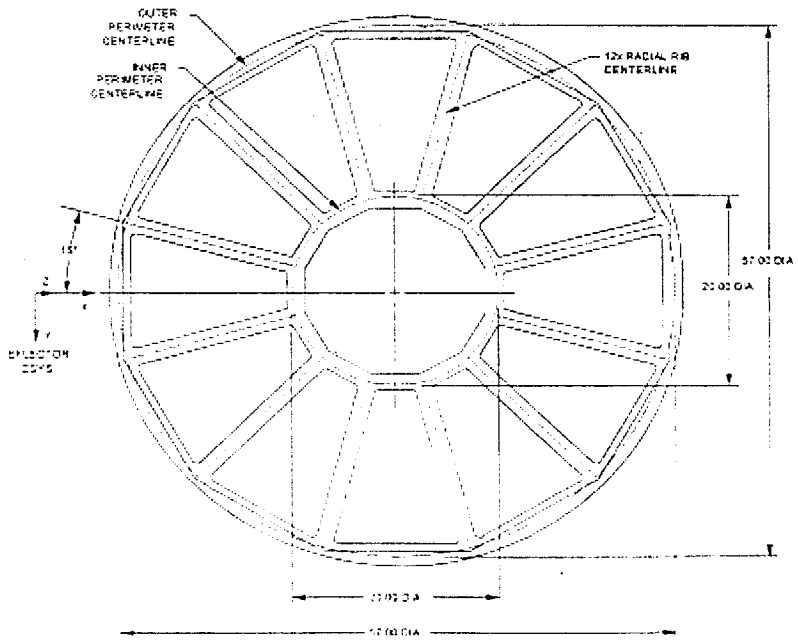

Figure 5.2: Reflector dimensions

To address these concerns, special finite elements were developed for the analysis of structures made of a single layer of triax woven fabric composites. The development of these special super-finite elements was described in Chapter 2. Basically the super-finite elements model the whole unit cell as shown in Figure 5.4. The super-finite element consists of many smaller elements assembled together. There are two different types of these smaller elements. One type represents a single thickness part and the other type represents a cross-over part. This cross-over part has two yarns crossing over each other. The resin layer between these cross-over yarn part is also modeled in the super-finite element. As such, the shear stress in the adhesive layer can be calculated. These super-finite elements were validated by analyzing rectangular panels to obtain mechanical properties. These properties compared well with experimental results. Effects of different parameters such as sample size, sample width were also investigated (see Chapter 3). The remaining question is how to use these super-finite elements for the analysis of a real size satellite structure made of triax fabric. The challenge is due to the large difference in size of the satellite structure (dimensions in thousands of millimeters) and the size of super-finite elements (dimensions in millimeters). Each of the super-finite elements has 15-node with 12 DOFs at each node. To model a 1000 mm by 1000 mm panel, it will require about 90,000 super-finite elements. This size problem is beyond the capacity of most personal computers. A similitude law is necessary to handle the problem.

In this chapter, the stress analysis of a membrane sector of ART EM reflector subjected to pressure is performed using the super-finite elements. This chapter presents the finite element model, the deformed configuration and the values and location of the maximum stresses of the membrane sector. A special similitude law was also discovered for the

deflection calculation.

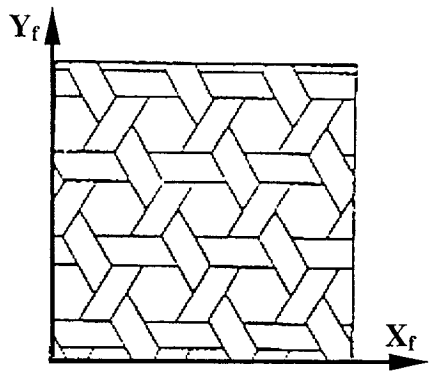

Figure 5.3: Triaxial woven fabric

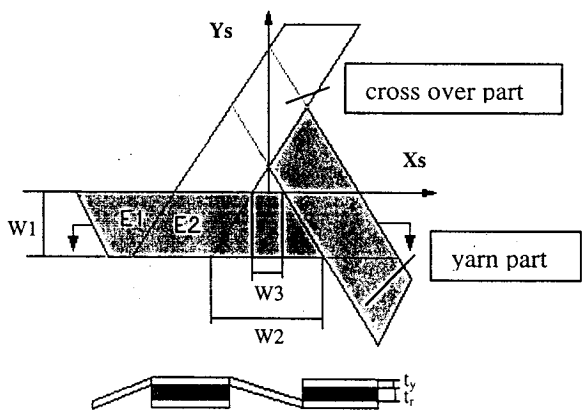

Figure 5.4: A unit cell (superelement)

5.2 Finite Element Model

One pie sector (out of twelve) as shown in Figure 5.2 was considered for analysis. A

pressure P = 200,000 Pa is applied on its inner surface (concave side). Since ribs surround the membrane sector, ribs' effect on the sector must be taken into account. Compared with the ribs, the membrane sector is much weaker in stiffness. So the membrane sector can be assumed as being clamped on its boundaries. For a short expression, the term 'super-finite element' will be replaced with the term 'element' in following statements.

Through the automatic meshing program, the membrane sector is discretized into 10,603 elements and 96,269 nodes. Since there are 12 DOFs at each node, 96269×12 unknowns need to be solved for this problem. This will require a computer with the ability to handle 96269×12 by 96269×12 matrix. The computer should have at least 96269×12 × 96269×12×32 bits memory because calculation must be performed in double precision condition. Even if some memory-saving skills are considered, it still is a large-scale problem that needs much more memory and can hardly be processed in a current personal computer. Therefore, this problem needs to be simplified before a solution can be obtained. As we know, for continuum and homogeneous problem, one may reduce the size of the object with similitude law and solve the problem of the size-reduced object to obtain the solution of the full-scale problem. But for the TWF composite, this strategy does not seem to be suitable. If the structure of the TWF composite is reduced in size, the unit cells built for it also need to be reduced in the same proportion. The number of the unit cells of size-reduced structure is still the same as one of full-scale structures. Since the element is set up on modeling a single unit cell, that means that the number of elements is not reduced in finite element model of the size-reduced structure. So the similitude law is not suitable for accurate solution of the TWF composite. We have taken

a different approach, that of studying different sizes of similar shape sectors and extracting from the results a similitude rule.

Table 5.1: Different size sectors

Parameters	Full size	Model size with scale λ
Yarn thickness	t	λt
Yarn width	w1	w1
Hexagon hole side length	w2	w2
Dimension and curvature radius of sector	L	λL

In this chapter, we make an approach by solutions of several size-reduced membrane sectors. Membrane sectors of sizes 1/12, 1/ 10 and 1/8, 1/7 and 1/6 of full scale are studied. These different sized models are shown in Figure 5.5. The applied pressure is still P = 200,000 Pa. Yarn thickness is reduced in the same proportion as the scale of the model, but the planar dimensions of the yarns are kept the same. This means that the planar dimensions of the finite elements are kept the same, while the thickness of the finite elements is reduced in proportion with the size of the model. Figure 5.5 shows the plan view of the sectors of different sizes. The curvatures of the models of different sizes are also reduced proportionally. This means that smaller sized models have smaller radius of curvatures. Coordinate z has the same common origin at 0 for all sectors. Table 5.1 gives the summary of the different size for the model.

5.3 Numerical Results and Discussions

Table 5.2 gives the geometric parameters of the unit cell (the unit cell is same as Superelement 2 in Chapter 2) measured from the microscopic photographs of the TWF composites. The thickness of the yarn in Table 5.2 is for the full scale structure and it is reduced proportionally for the smaller sized models. Table 5.3 lists the fiber and matrix properties for the fiber volume fraction $V_f = 0.695$. Table 5.4 shows the effective elastic properties of the impregnated yarn obtained by using the composite cylinder assemblage (CCA) model. These data are used for finite element models.

Table 5.2: Geometric parameters

Geometric parameters	Measured values
Yarn thickness t (mm)	0.14
Yarn width w1 (mm)	0.85
w2 (mm)	1.10

Table 5.3: Elastic properties of fibers and matrix

Material	E_L (GPa)	E_T (Gpa)	G_{LT} (Gpa)	G_{TT} (Gpa)	ν_{LT}	ρ (gm/cm^3)
Carbon Fiber	500.0	40.0	24.0	14.3	0.26	2.10
Epoxy Resin	3.5	3.5	1.3	1.3	0.35	1.17

Table 5.4: Elastic properties of the impregnated yarn of TWF composites

Material	E_L (Gpa)	E_T (Gpa)	G_{LT} (Gpa)	v_{LT}	v_{TT}	V_f	ρ (gm/cm^3)
YS-50A-15S carbon/epoxy	338.57	12.40	5.61	0.287	0.437	0.695	1.8164

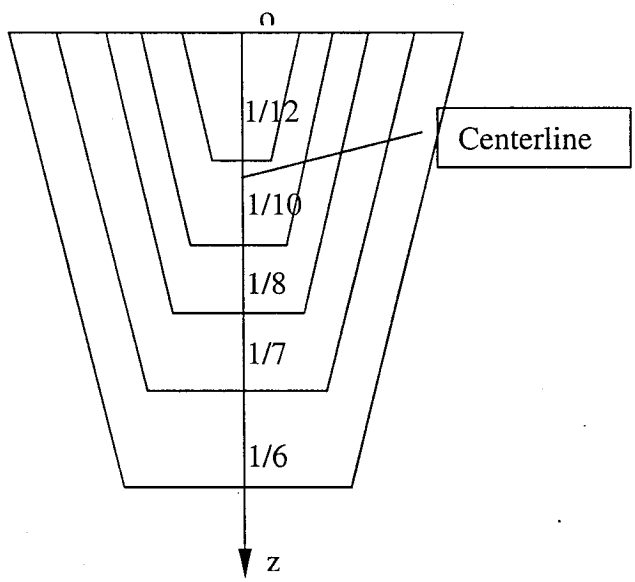

Figure 5.5: Different-size sectors

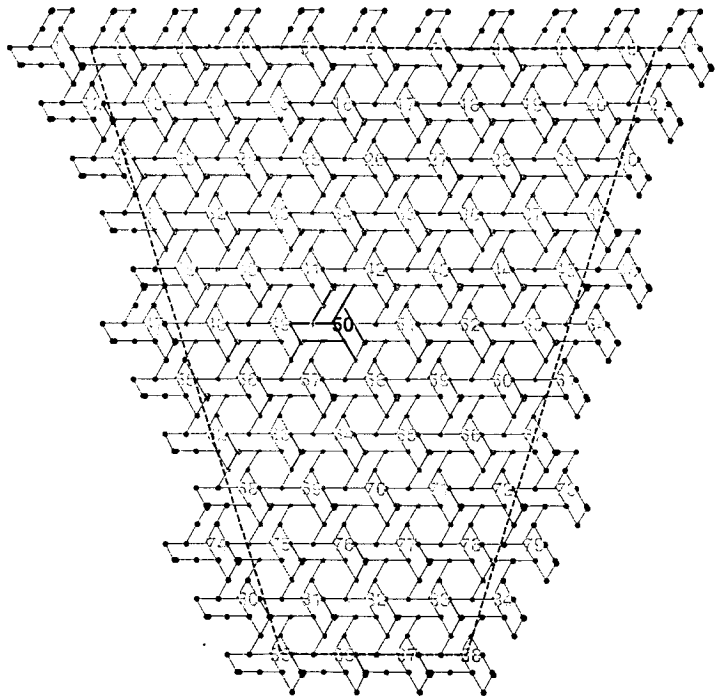

Figure 5.6: Mesh of 1/12 sector (Front)

5.3.1 Finite element Models

Figures 5.6 and 5.7 show the finite element mesh for a sector of 1/12 scale. There are 88 elements and 868 nodes. The boundary conditions are assumed to be clamped all around, i.e., the displacements of all nodes outside red lines in Figures 5.6 and 5.7 are set to zero. Figure 5.8 shows the finite element mesh for a sector of 1/10 scale. There are 130 elements and 1264 nodes. The meshes for other sector scales are similar.

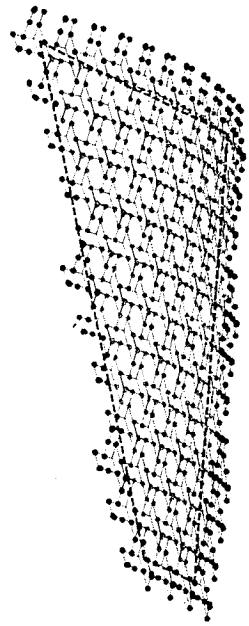

Figure 5.7: Mesh of 1/12 sector (Isometric)

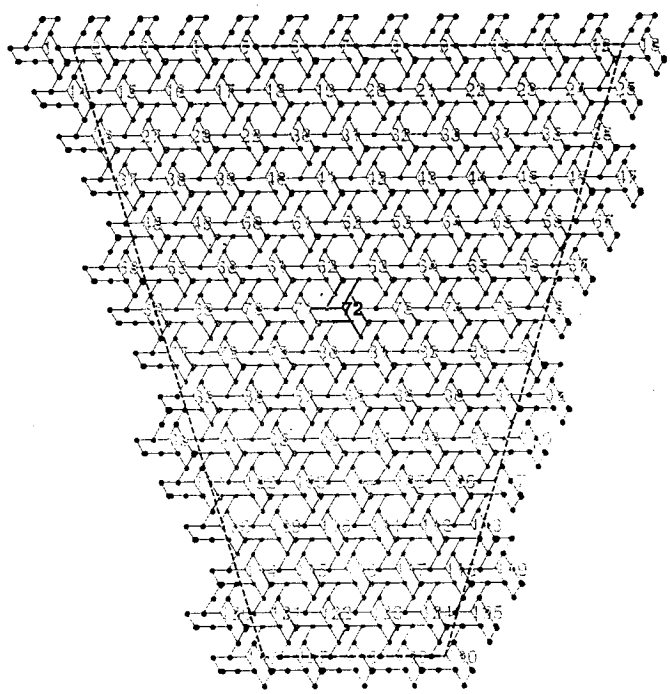

Figure 5.8: Mesh of 1/10 sector (Front)

5.3.2 Sector deflection along the centerline Oz

The lateral deflections at the nodes (along the Oz line) for the 1/12 scaled sector are shown in Figure 5.9. The deflection is 0 at two ends due to the clamped boundary conditions. The deflection is increasing as one moves away from the larger side of the sector to the smaller side of the sector. This occurs because the reflector is a shell with curvature.

The deflections for other scaled sectors also follow similar shaped curves. The superposition of the deflections for all sectors is shown in Figure 5.10. The origin O in Figure 5.10 corresponds to the origin O in Figure 5.5. It is interesting to note that apart from end conditions and local variations, the deflection for all five scaled sectors fall along the same line. The amplitude for the local variations is about $\pm 0.6 \times 10^{-4}$ m. It is important to remember that the thickness of the yarn for each scaled sector is also reduced by the same proportion. This means for the 1/12 scaled sector, the thickness of the yarn is t/12 where t is the thickness of the full scale sector. For the 1/10 scaled sector, the thickness of the yarn is t/10 etc.

The deformed configurations for the 1/12 scaled sector and the 1/10 scaled sector are shown in Figures 5.11 and 5.12.

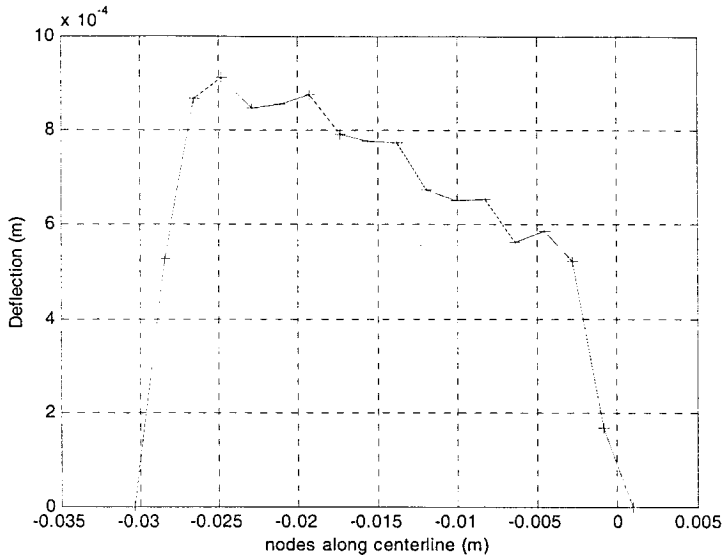

Figure 5.9: Deflection of 1/12 sector along its centerline

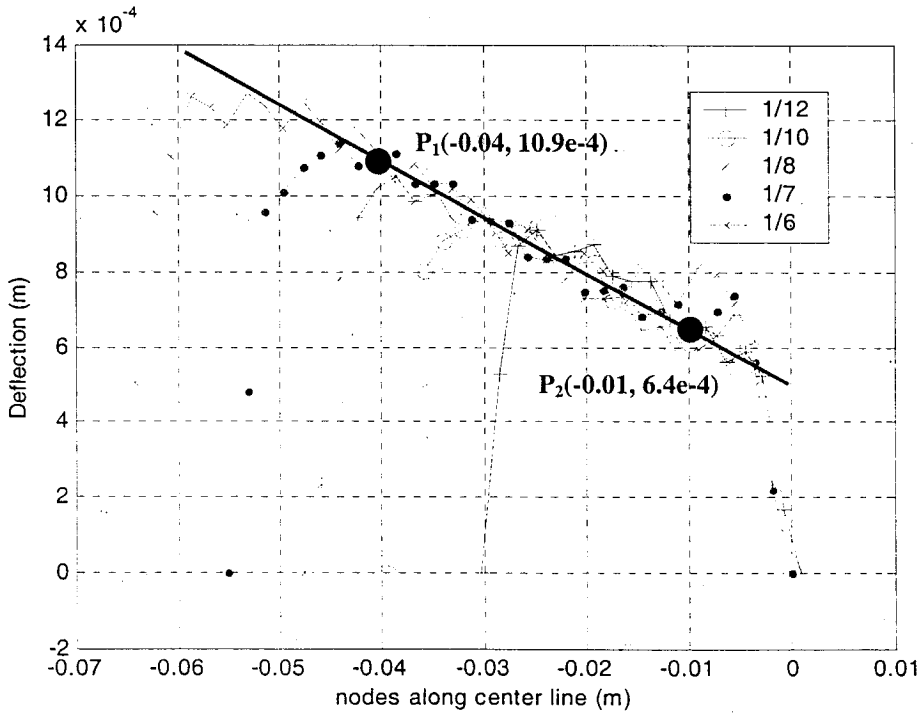

Figure 5.10: Deflection of different-scale sectors on their centerlines

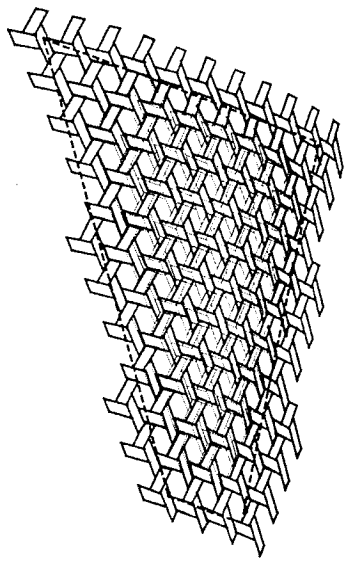

Figure 5.11: Deformed and undeformed configurations of 1/12 sector

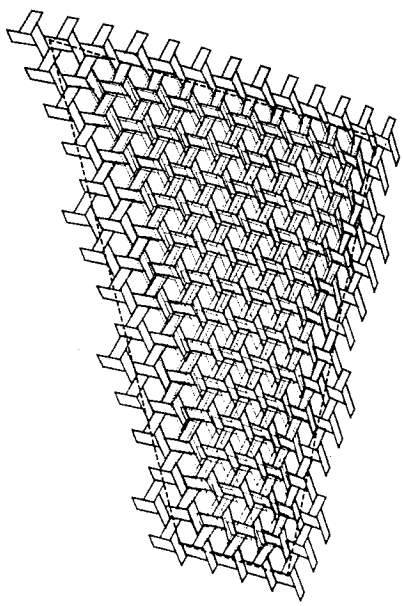

Figure 5.12: Deformed and un-deformed configurations of 1/10 sector

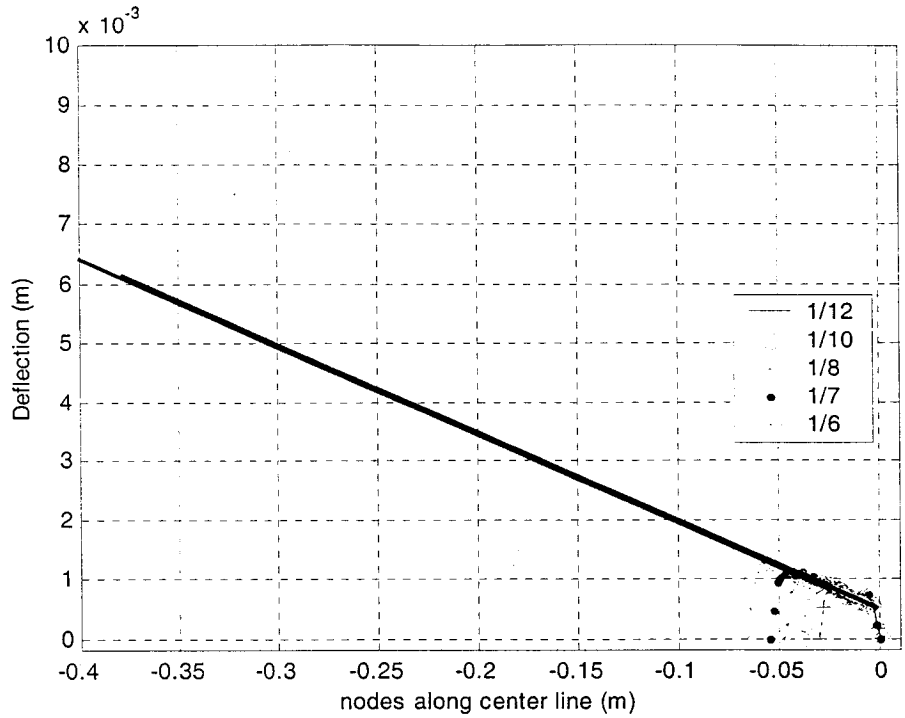

Figure 5.13: Predicted defection of full-scale sector along its centerline

5.3.3 Similitude observation for deflection

The appearance of the common straight line begs for a similitude observation. An equation for the straight line can be obtained by using the coordinates of two points. Point P_1(-0.04 m,10.9 × 10^{-4} m) and point P_2(-0.01 m, 6.4 × 10^{-4} m) on the curve are used (note that the first argument in the parenthesis represents the position along the Oz line and the second argument in the parenthesis represents the deflection at that point). The following equation is obtained:

$$v = -0.0150z + 4.9\times10^{-4} + \delta \qquad (1)$$

where v is the deflection (m). z is the coordinate distance from O as shown in Figure 5.5

(m). δ represents the magnitude of the local variations, which in this case is $\pm 0.6 \times 10^{-4}$ (m). Equation (1) is plotted as shown in Figure 5.13. This equation is not valid close to the clamped boundaries. The range of validity of this equation for the full scale model can be -0.38 m < z < -0.03 m.

5.3.4 Explanation for the deflection behavior of the triax panel

The coinciding of the deflection at the center line of triax panels of different scales is intriguing. In order to explain this behavior, supplementary investigation was carried out. There are a few parameters that enter into the situation. These consist of the trapezoidal shape of the reflector panel, the curvature of the panel, and the triax material itself. Each of these parameters is examined separately to determine the reason for the behavior.

Effect of the trapezoidal shape

To determine the effect of the trapezoidal shape, a rectangular panel with cylindrical curvature made of triax was modeled using the super-finite elements. Figure 5.14 shows the full-scale configuration of this panel ($t_1 = 0.14 \times 10^{-4}$ m, $R_1 = 0.07239$ m). All edges of this panel are clamped. Two different scales of this panel were analyzed with the same superelement planar size as in Table 5.2. One is full-scale and the other scale is 0.8. The relative dimensions are as follows:

$a_2 = \lambda a_1$
$b_2 = \lambda b_1$
$R_2 = \lambda R_1$
$t_2 = \lambda t_1$

where subscripts 1, 2 refer to model 1, model 2 and λ is the scale factor, equal to 0.8.

The centerline deflections for the two models are shown in Figure 5.15.

It can be seen from Figure 5.15 that apart from the edge effect, the center line deflections of both panels are the same. The deflection is constant along the center line because of cylindrical bending. Therefore, this case exhibits the same behavior as in the curved trapezoidal panels is observed in Figure 5.10. The trapezoidal shape is therefore not an effect.

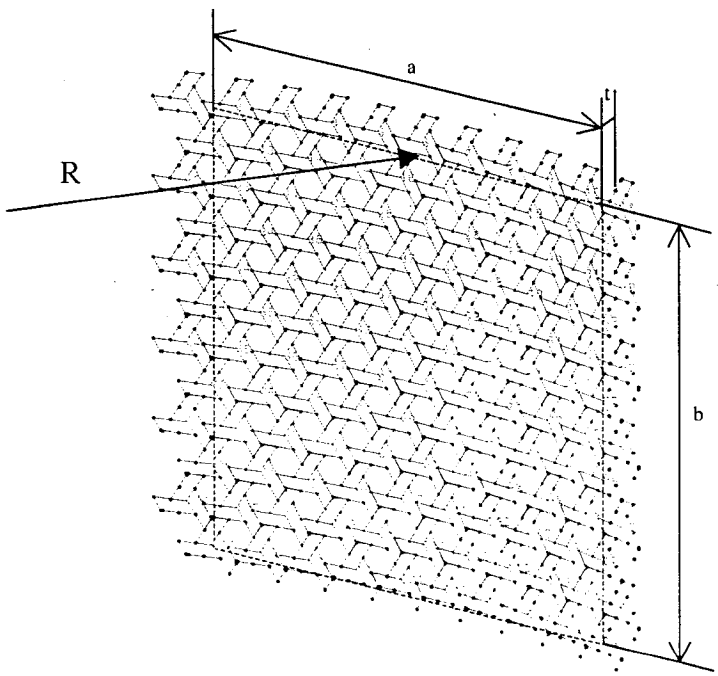

Figure 5.14: Rectangular triax panel with cylindrical curvature

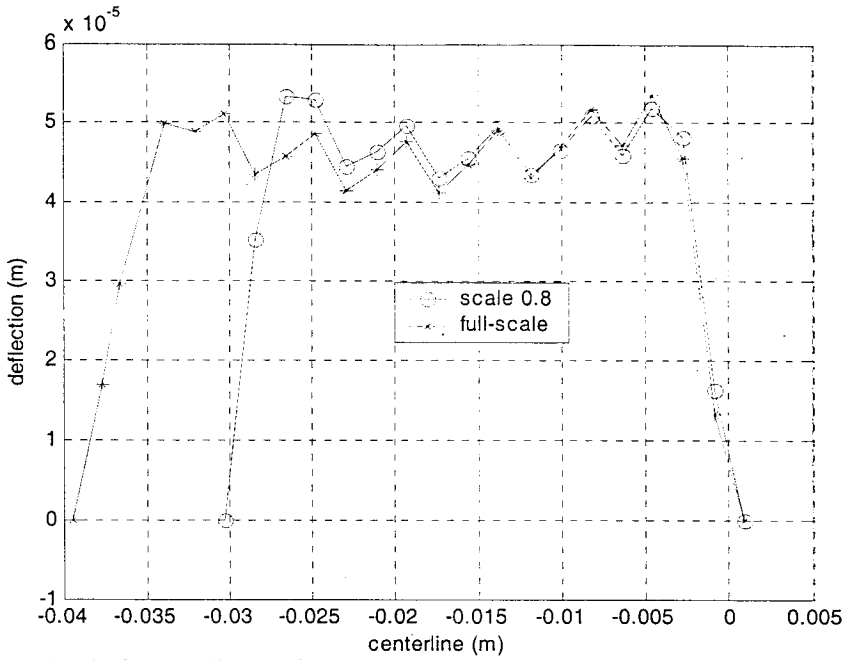

Figure 5.15: Center line deflection of curved rectangular triax panels of two

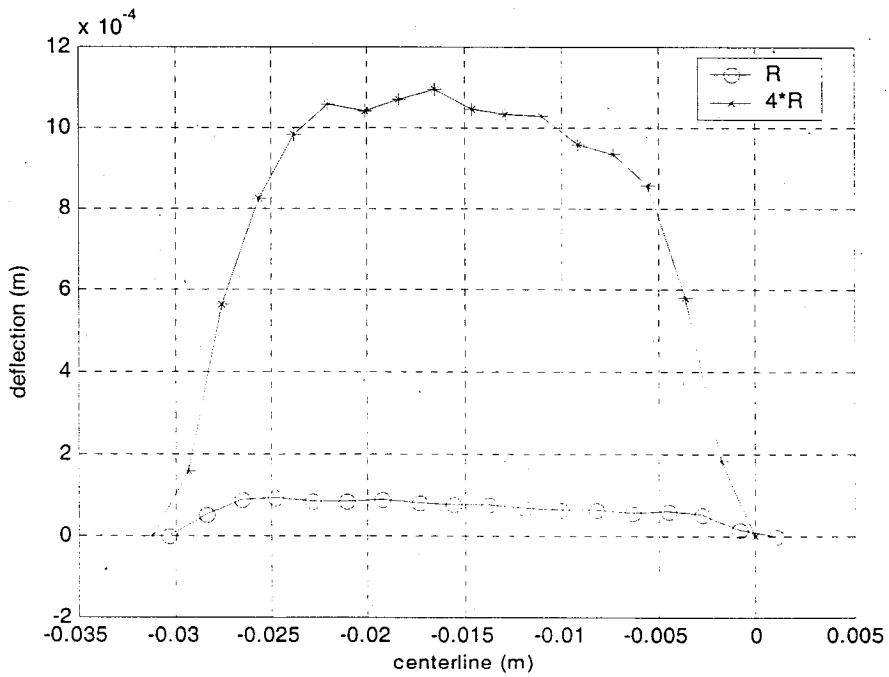

Figure 5.16: Center line deflection of trapezoidal triax panels of different curvatures

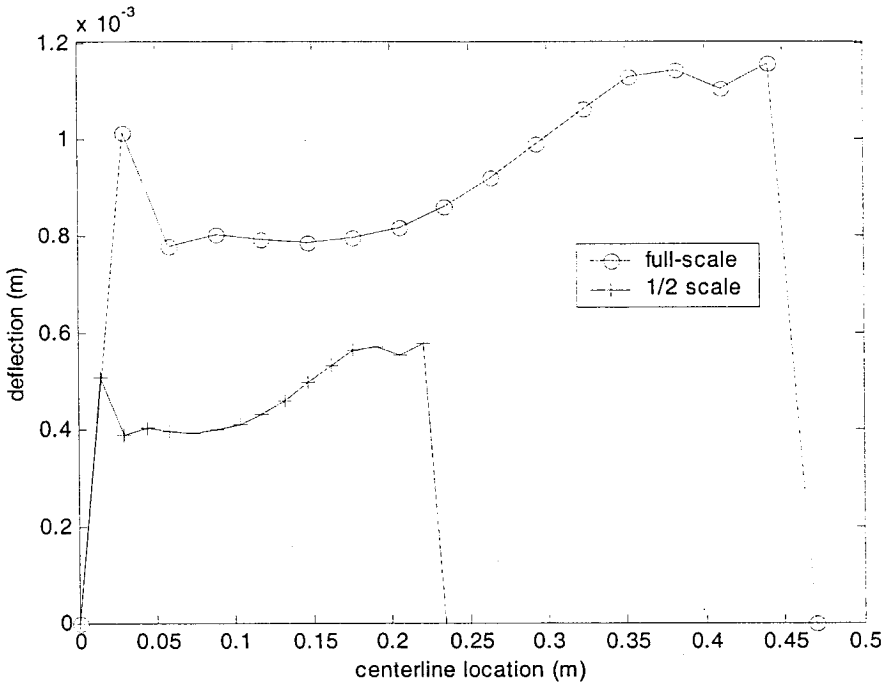

Figure 5.17: Deflections of isotropic sectors along the centerlines

Effect of curvature of the panel

To investigate this effect, trapezoidal triax panels of the same overall planer dimensions and same thickness but with different radius curvatures were analyzed. The dimensions for the different models are as follows:

$a_2 = a_1$
$b_2 = b_1$
$R_2 = \lambda R_1$
$t_2 = t_1$

In the above dimensions, subscript 1 refers to a model that is 1/12 the full scale reflector sector. The scale factor λ studied is 1/1 and 1/4. Figure 5.16 shows the center line

deflections of these models.

It can be seen from Figure 5.16 that the smaller is the radius of curvature the smaller is the center line deflection. This should be expected. The dependence on the radius of curvature is therefore normal.

Effect of the triax material

To investigate the effect of the triax material, two additional studies were made.

(1) Panels made of isotropic material:

First panels of the same trapezoidal shape, dimensions and curvature as the triax panels studied before, but made of isotropic material (E = 30.56 GPa and ν = 0.3) were analyzed. Shell elements in ANSYS software were used for this analysis. Two different scales (full and half) were examined. The full scale has the same dimension as the reflector sector. The center line deflections of these panels are shown in Figure 5.17. It can be seen that the half scale model has half the deflection as compared to the deflection of the full scale model. This follows the similitude law as described in a following section.

(2) Flat triax panels subjected to bending:

Flat triax panels of different dimensions were analyzed. The dimensions of the panel are as follows:

$$a_i = \lambda a_1$$
$$b_i = \lambda b_1$$
$$R_i = \lambda R_1$$
$$t_i = \lambda t_1$$

where the subscript i refers to the smaller scaled model. The scale factor λ takes on values of 10/10, 8/10 and 6/10. The results are shown in Figure 5.18. From this figure, the center deflection of the smaller model is smaller than the center deflection of the larger model.

If one were to use the general equation for the deflection of an isotropic rectangular flat plate subjected to bending, one has [77]:

$$\delta = \frac{\alpha q a^4}{E t^3}$$

where a is the side of the square, q is the pressure, E is the Young's modulus, t is the thickness and α is a shape factor for the rectangle. The Poisson ratio is already incorporated into the factor α.

From the above equation, if the dimensions of the plate are reduced proportionally (for both *a* and *t)*, the deflection δ would be proportional to the length scale. This means that for a half scaled model, the deflection would be half that of the full scale model. This is the case for the isotropic curved trapezoidal plates results as shown in Figure 5.17 above. Examining the results in Figure 5.18 shows that the ratios between the deflections for

different models are as follows:

$$\frac{\delta_6}{\delta_{10}} = \frac{5x10^{-5}m}{16.5x10^{-5}m} = 0.30$$

$$\frac{\delta_8}{\delta_{10}} = \frac{10.5x10^{-5}m}{16.5x10^{-5}m} = 0.64$$

The above ratios do not agree with 0.6 and 0.8 as would be expected from the similitude law. Therefore the material effect needs to be taken into consideration.

Using the triax super-finite elements, flat triax panels subjected to uniaxial in-plane loadings were analyzed. The displacements were used to calculate the apparent Young's moduli and Poisson's ratios (the procedure was explained in Chapter 3). The results are shown in Table 5.5.

Table 5.5: Change of Young's moduli and Poisson's ratios with triax thickness

Triax thickness (mm)	Young's modulus E_1 (GPa)	Young's modulus E_2 (GPa)	Poisson ratios v_{12}	Poisson ratios v_{21}
0.14	30.56	26.69	0.58123	0.56451
0.07	37.00	32.42	0.52126	0.50328
0.035	41.03	35.63	0.48620	0.46767

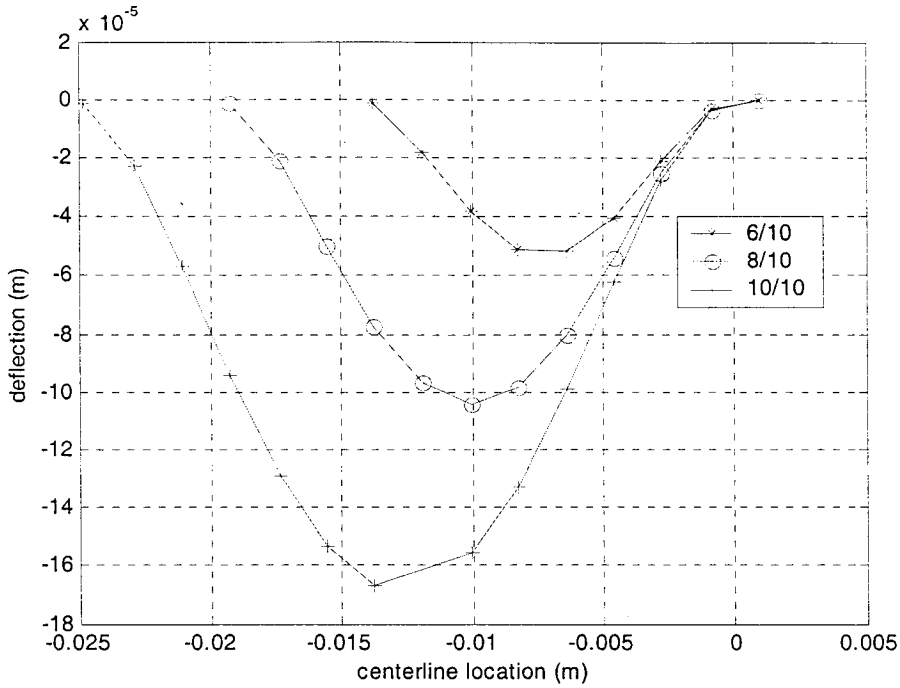

Figure 5.18: Deflections of TWF square plates along the centerlines

From Table 5.5, as the thickness of the triax decreases, the Young's moduli increase and the Poisson ratios decrease. Since the Young's moduli increase and the Poisson ratios decrease, the deflection of the thinner models would be reduced accordingly. This explains the lower ratio between the deflections in the above equation.

The behavior as shown in Figures 5.10, 5.13, and 5.15 are therefore unique to triax materials and maybe also to some other materials made by textile process. This behavior can be considered as a discovery from this work since the author believes that this behavior has not been reported before. This behavior was proven very useful for the determination of deflection of large panels made of triax materials such as in satellite structures.

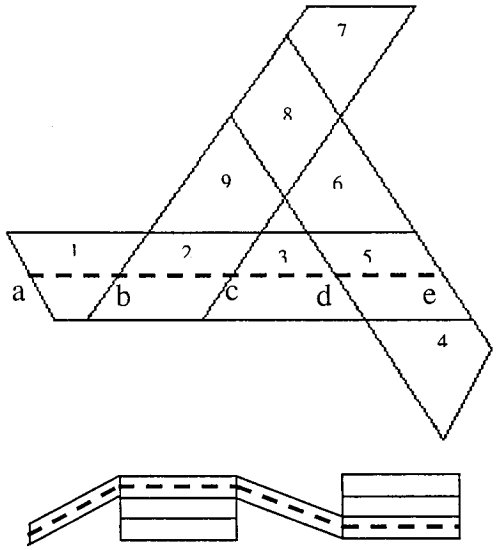

Figure 5.19: Centerline of yarn on unit cell

5.3.5 Stress distribution of yarns of unit cells in central area of the sector

The TWF composites support loads mainly by yarn extension in fiber direction. Hence it is necessary to investigate the stress distribution of the yarns in fiber direction. In this section, stress distributions along yarn centerline in central areas of different scale sectors are investigated. Consider 5 different scale sectors with scales 1/12, 1/10, 1/8, 1/7 and 1/6. For each sector, a yarn of a unit cell (super-element) in central area of the sector is selected. The super-element numbers 50, 72, 114, 159 and 218 are selected respectively for the reflectors 1/12, 1/10, 1/8, 1/7 and 1/6. The location of super-element 50 is shown in Figure 5.6 and that of super-element 72 is shown in Figure 5.8. The yarn orientation on each super-element is shown in Figure 5.19. The stress distributions along the yarn centerline of these unit cells are calculated and plotted together in Figure 5.20. In Figure 5.20, s refers to the relative location of the point on the yarn centerline, at which the

stress $\sigma 1$ is evaluated. 0-2 corresponds to a-b in Figure 5.19. 2-4, 4-6 and 6-8 are corresponding respectively to b-c, c-d and d-e in Figure 5.19. From Figure 5.20, it is easy to find that all the stresses $\sigma 1$ along b-c and d-e (crossovers) remain the same value of about 1.5 GPa for different scale sectors. The corresponding stress of the full-scale sector should also be about 1.5 GPa. Along a-b and c-d, the stress $\sigma 1$ varies greatly. But there are some special points at which the stress values basically keep the same for these 5 different-scale sectors. At point s = 0.6 of a-b (see Figure 5.20), the stresses are about 1.2 GPa. For c-d, at point s = 4.4, the stress value is about –0.2 GPa. At point s = 5.6, the stress value is about 3.7 GPa. We can speculate that the full-scale sector also has these characters.

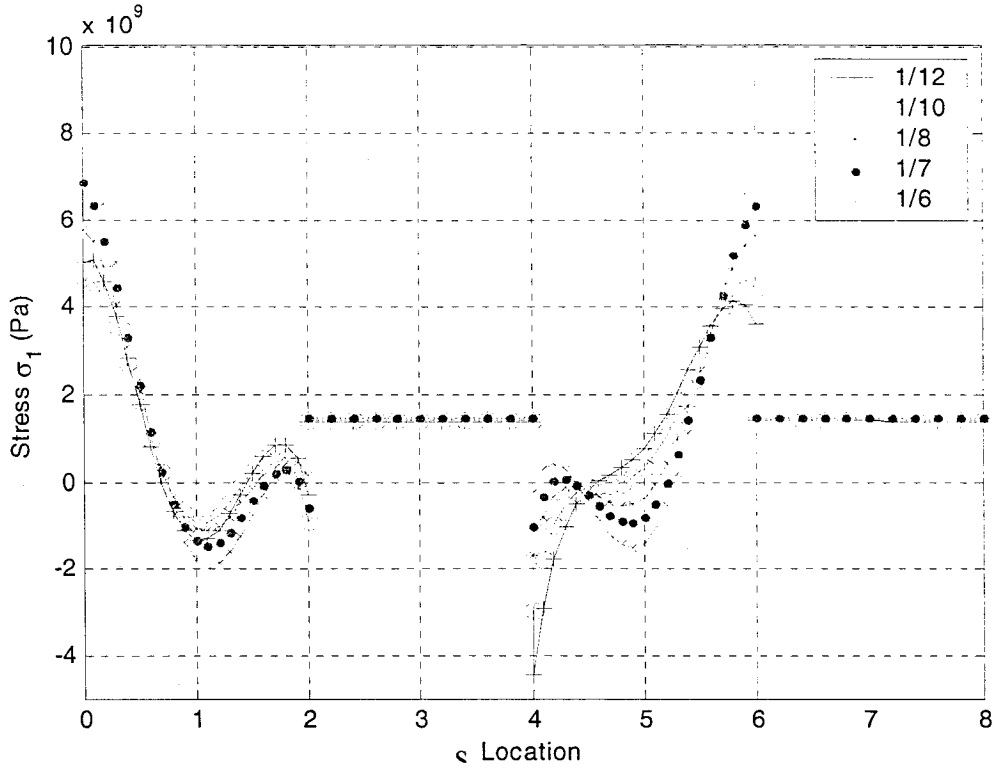

Figure 5.20: Stresses σ_1 of yarn centerlines of unit cells of 5 different scale sectors

5.3.6 Maximum stresses

Figure 5.21 gives the locations of maximum stresses σ_{1max}, σ_{2max} and σ_{12max} of the 1/12 sector. σ_1 represents the normal stress along fiber direction, σ_2 is the normal stress along transverse direction and σ_{12} is the shear stress. Table 5.6 gives the locations and values of maximum stresses. In this table, se denotes super-element and e denotes element number. Orientations of elements in super-element are given in Figure 5.19. The element natural coordinates in the table give locations of maximum stresses in the element.

Figure 5.22 gives the locations of maximum stresses σ_{1max}, σ_{2max} and σ_{12max} of the 1/10

sector. Table 5.7 gives the locations and values of maximum stresses.

Figure 5.23 gives the locations of maximum stresses σ_{1max}, σ_{2max} and σ_{12max} of the 1/8 sector. Table 5.8 gives the locations values of maximum stresses.

In above three examples, there are some characters in common. All maximum stresses appear in areas near boundaries. Maximum stresses always exist at the transition between a single thickness area and the crossover area such as a, b, c, d and d in Figure 5.19. σ_{2max} and σ_{12max} are located at same location. For this load case, the yarns of the sectors mainly bear tension loads. Failure probably starts at these transition areas with the damage in tension mode.

Table 5.6: Maximum stresses in the 1/12 sector

Maximum Stress (GPa)	σ_{1max}=-354.49	σ_{2max}=-3.5540	σ_{12max}=-1.7796
Stresses (GPa) (σ_1, σ_2, σ_3, σ_{13}, σ_{23}, σ_{12})	-354.49 -2.3780 -4.2558 4.5177 3.6877 0.27907	-72.508 -3.5540 -2.8819 1.6963 4.0379 -1.7796	-72.508 -3.5540 -2.8819 1.6963 4.0379 -1.7796
Location (se, e, layer)	(83, 6, 1)	(83, 3, 1)	(83, 3, 1)
Element natural coordinates (ξ,η,ς)	(0.90618, -0.90618, 0.90618)	(-0.90618, -0.90618, 0.90618)	(-0.90618, -0.90618, 0.90618)

Table 5.7: Maximum stresses in the 1/10 sector

Maximum Stress (GPa)	σ_{1max}=-303.33	σ_{2max}=-3.7244	σ_{12max}=-1.6064
Stresses (GPa) (σ_1, σ_2, σ_3, σ_{13}, σ_{23}, σ_{12})	-303.33 -2.0356 -3.5401 3.4341 2.8232 0.28237	-51.237 -3.7244 -5.6891 -3.9775 12.451 -1.2136	-56.307 -3.2587 -2.6794 1.2802 3.5072 -1.6064
Location (se, e, layer)	(124, 6, 1)	(115, 1, 1)	(124, 3, 1)
Element natural coordinates (ξ,η,ς)	(0.90618, -0.90618, 0.90618)	(-0.90618, 0.90618, -0.90618)	(-0.90618, -0.90618, 0.90618)

Table 5.8: Maximum stresses in the 1/8 sector

Maximum Stress (GPa)	σ_{1max}=-284.37	σ_{2max}=4.4567	σ_{12max}=1.9973
Stresses (GPa) (σ_1, σ_2, σ_3, σ_{13}, σ_{23}, σ_{12})	-284.37 -1.8757 -3.2591 2.8256 2.4735 0.26829	162.82 4.4567 3.7927 -1.0783 -4.9419 1.9973	162.82 4.4567 3.7927 -1.0783 -4.9419 1.9973
Location (se, e, layer)	(180, 6, 1)	(190, 7, 1)	(190, 7, 1)
Element natural coordinates (ξ,η,ς)	(0.90618, -0.90618, 0.90618)	(-0.90618, -0.90618, 0.90618)	(-0.90618, -0.90618, 0.90618)

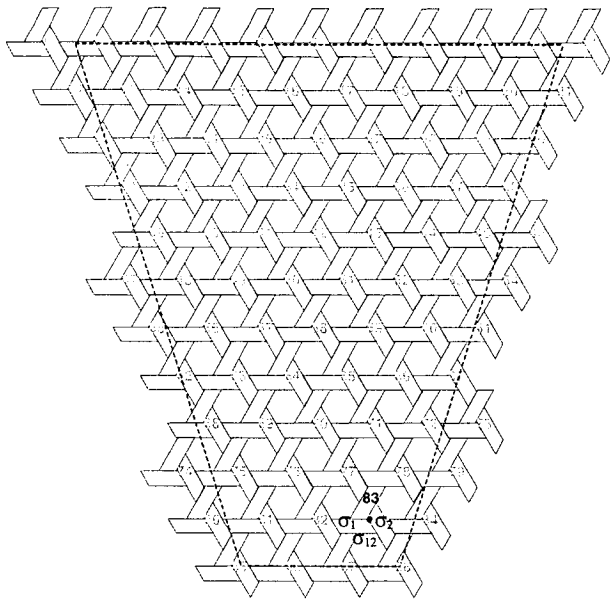

Figure 5.21: Locations of maximum stresses in the 1/12 sector

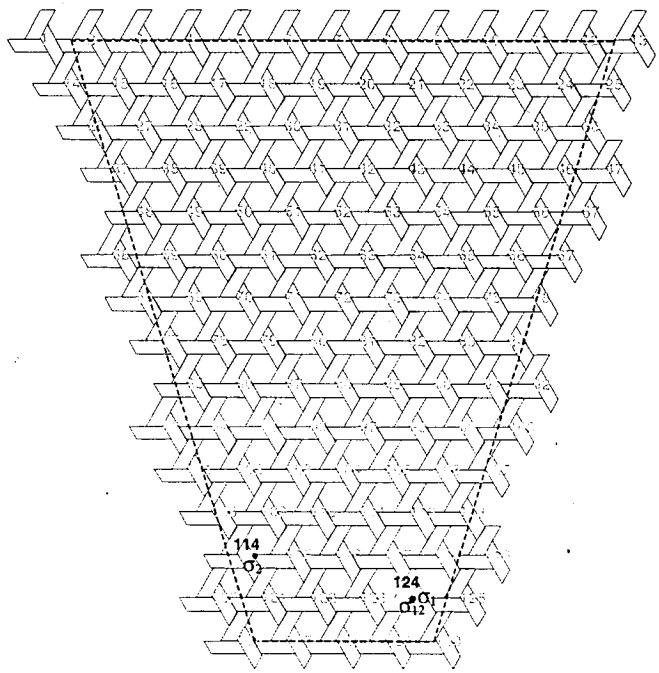

Figure 5.22: Locations of maximum stresses in the 1/10 sector

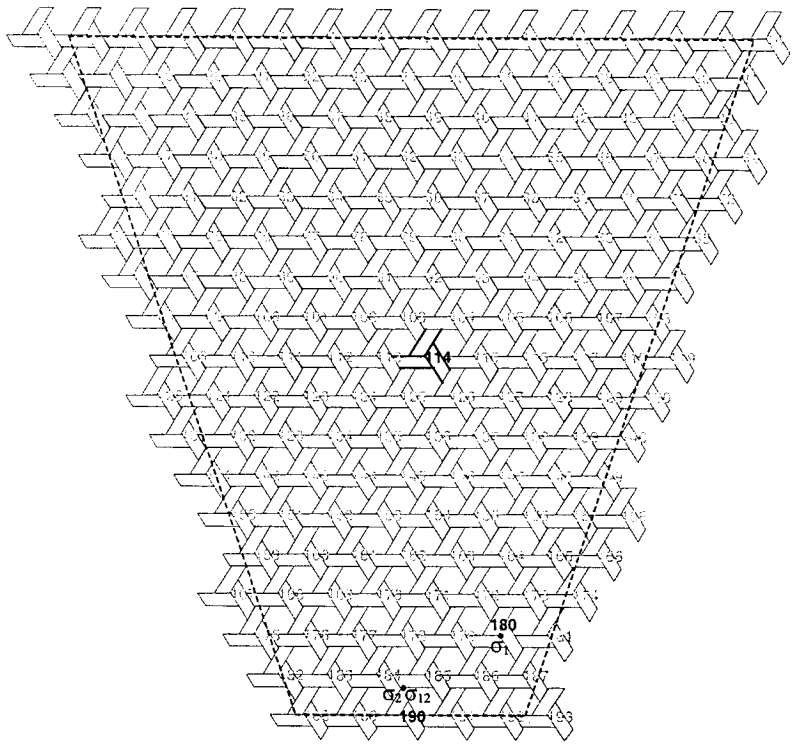

Figure 5.23: Locations of maximum stresses of 1/8 sector

5.4 Conclusions

In this chapter, the mechanical behavior of a sector of the reflector subjected to uniform pressure is studied by modeling several different-scale sectors using Super-finite elements. Using this approach, it is possible to determine the deflection along the centerline of the full-scale sector using the deflection of the reduced scale sectors. A special scale law was discovered for the deflection behavior of triax composites. This special scale law is very useful for the deflection determination of large panels made of triax. The scale law may be applicable to thin structures made of other types of textile

composites. This can be a subject of future research.

The stress distribution of yarns in central areas of the sector is presented. The maximum stresses are presented. The stress distributions are complex and it is not possible to derive a similitude rule even though some areas of constant stresses are observed.

Chapter 6

Progressive Failure of Triaxial Woven Fabric (TWF) Composites

In this chapter, progressive failure of Triaxial Woven Fabric (TWF) composite panels subjected to uni-axial extension is studied numerically and experimentally. In numerical study, TWF panel is discretized respectively using linear and nonlinear Super-Finite-Elements proposed here. Tensor polynomial progressive failure procedure is employed with maximum stress criterion, Hoffman criterion and Tsai-Wu criterion. Two displacement-loading cases are considered. The first and ultimate failure loads, maximum extension displacement, locations and modes of failure are estimated and compared with experimental data.

6.1 Introduction

Progressive failure analysis can predict the initiation and growth of damage and is essential for evaluating the performance and reliability of TWF composite structures. It is recognized from progressive failure simulation that TWF composite structure can develop local failures or exhibit such local damage as matrix cracks, fiber breakage,

fiber/matrix debonds, and delaminations under normal operating conditions, and that such damage can contribute to the ultimate failure of the structure. The ability to predict the initiation and growth of such damage is essential for predicting the performance of TWF composite structures and developing reliable, safe designs that exploit the advantages offered by TWF composites. Progressive failure simulations can reduce testing requirements in composite structures. Progressive failure analysis is a feasible tool for predicting failure in composite structures.

There are a lot of studies on plain-woven fabric composites. Most of the studies on such composites have focused on predicting their thermo-elastic properties as seen in Chapter 1. Studies relating to prediction of their strength and failure modes are relatively few [80-83].

In this chapter, progressive failure of TWF composites is studied numerically and experimentally. In numerical study, TWF panel is discretized respectively using linear and nonlinear Super-Finite-Elements proposed here. This nonlinear Super-Finite-Elements are actually Superelement 2 proposed previously but with consideration of large displacements. In analysis, lamina damage modes such as matrix cracking, fiber-matrix shear failure, and fiber failure are modeled by degrading the material properties. Tensor polynomial progressive failure procedure is employed with maximum stress criterion, Hoffman criterion and Tsai-Wu criterion. Two displacement-loading cases are considered. The first and ultimate failure loads, maximum extension displacement, locations and modes of failure are estimated and compared with experimental data.

6.2 Experimental Work

Tensile tests were performed for strength and Young's modulus of TWF composites. Details on this experiment were stated in Chapter 3.

Strengths were determined from the stresses when ultimate failure occurs. Tensile moduli were determined from the slope of the linear portion of the stress-strain curve. It should be noted that strain-stress curve is not linear. Figure 6.2 shows a typical strain-stress curve for the TWF composites when loading is along the longitudinal direction. This curve was obtained from specimen C4 (Table 3.4). The initial slope is smaller than the slope at larger stress. This can be explained by the straightening of the undulation of the yarns. The yarns become stiffer as they are more and more straightened.

Table 3.4 shows the longitudinal strength and Young's moduli of the TWF specimens. The measured strength values of various specimens distribute between 216.9 MPa and 261.0 MPa. Average modulus is 239.4 MPa.

Table 3.5 shows the results from the transverse tensile tests. Two types of specimens were used. Specimens of series B have width of 50 mm while specimens of series E have width of 43 mm. Specimens with larger width show larger strength (108.9 MPa) as compared to specimens with smaller width (100.6 MPa). This is because for a certain length, wider specimens would have more clamped yarns (a clamped yarn is a yarn that has both ends clamped by the grips) than narrower specimens. As such, wider specimens would tend to have larger strength.

6.3 Progressive Failure of TWF composites

Progressive failure analysis is based on the assumption that the damaged material could be replaced with an equivalent material having degraded properties. The effects of matrix and yarn failure are taken into account in accordance with state of stresses and failure criterion. The TWF composite is a plain single layer woven fabric, as shown in Figure 6.1. It can actually be obtained by assembling many unit cells. A unit cell consists of 6 yarn parts and 3 crossover parts, shown in Figure 6.3. A yarn part is a single curved lamina and a crossover part is constructed of three laminas (interlamina is a resin lamina). So a lamina can be considered as a primary failure unit. Since a yarn part (a single lamina) is very thin and does not have any traction on its top and bottom surfaces, stresses σ_{13}, σ_{23}, σ_3 in material principal axes are very small in comparison with stresses σ_1, σ_2, σ_{12}. Stresses σ_1, σ_2, σ_{12} are expected to play important role in the failure of a yarn part (a lamina). These three in-plane stresses are used in the selected failure criterion to predict the failure of a yarn part (a lamina). For a crossover part with 3 laminas, there is no traction on its top and bottom surfaces. For each lamina, stresses σ_{13}, σ_{23}, σ_3 in material principal axes are very small in comparison with stresses σ_1, σ_2, σ_{12}. Stresses σ_1, σ_2, and σ_{12} play important role in the failure of each lamina. They are used in the selected failure criterion to predict the failure of each lamina. The lamina failure is said to have occurred when the state of stress at any point within the lamina satisfies the selected failure criterion. In analysis, the calculation of stresses is done at the Gauss points. For element E1 (Figure 6.3), 4 by 4 by 2 Gauss points are applied for integration. Element E2 is integrated using 3 by 3 by 2 Gauss points for each lamina. When the state of stress at

any Gauss point on a lamina satisfies the selected failure criterion, that lamina has failed. The first failure refers to the situation at which one or more than one laminas fail first as the load is increased. After the first failure, the progressive failure analysis is carried out using tensor polynomial failure procedure [78,79,87]. In this study, for the development of the strength model it was assumed that the TWF panel is initially free of damage.

6.3.1 Tensor polynomial progressive failure procedure

At each load step, Gauss point stresses are used in the selected tensor polynomial failure criterion. If failure occurs at a Gauss point in a lamina, a reduction in the lamina stiffness is introduced in accordance with the mode of failure that causes the changes in the overall laminate stiffness. Following failure indices are used to determine failure modes.

$$\begin{aligned} H_1 &= F_1\sigma_1 + F_{11}\sigma_1^2 \\ H_2 &= F_2\sigma_2 + F_{22}\sigma_2^2 \\ H_6 &= F_{66}\sigma_6^2 \end{aligned} \tag{6.3.1}$$

Notations F_i and F_{ij} in above expressions are defined in tensor polynomial failure criterion. Failure indices (H_1, H_2, H_6) represent the weight of various principal stress terms in the tensor polynomial failure criterion and the largest H_i term is selected to represent the dominant failure causing stress and the corresponding mode of failure. For example, if H_1 is the largest then σ_1 is the failure causing stress and the corresponding failure mode is fiber failure. Similarly, H_2 corresponds to the transverse mode of failure (failure due to in-plane normal stresses transverse to the fiber direction) and H_6 corresponds to τ_{12} (in-plane shear) mode of failure. After the identification of the mode of

failure, the corresponding elastic modulus of the failed lamina is reduced to a negligible value. The fiber mode of failure corresponds to modulus E_1 and v_{12}; the transverse mode of failure corresponds to E_2, v_{21} and the in-plane shear mode of failure corresponds to G_{12}. An outline of the steps required is as follows:

(1) At each load step, calculate the stresses at the middle of each layer at each of the Gauss points.

(2) Transform the stresses to coordinates of the material property symmetry.

(3) Compute failure indices, H_1, H_2, H_6.

(4) If failure occurs reduce the appropriate lamina elastic constants to zero and recomputed laminate stiffness and restart analysis at the same load step.

(5) If no failure occurs, proceed to the next load step.

(6) Final failure is said to have occurred when the TWF panel is no longer able to carry any further increase in load.

6.3.2 Tensor polynomial failure criteria

The most general polynomial failure criterion, as proposed by Tsai (1984), contains linear, quadratic and higher order terms of stresses and is expressed in in-plane type as

$$F_1\sigma_1 + F_2\sigma_2 + 2F_{12}\sigma_1\sigma_2 + F_{11}\sigma_1^2 + F_{22}\sigma_2^2 + F_{66}\sigma_6^2 \le 1 \quad or \quad H_1 + H_2 + H_6 \le 1 \quad (6.3.2)$$

where F_i, F_{ij} (i, j=1,2,6) are the strength tensors of the second and fourth rank. σ_1, σ_2 are the normal stress components; σ_6 is the shear stress component in the principal material directions 1 and 2 (the subscript 1 referring to the fiber direction). It is a phenomenological failure criterion that predicts the imminence of failure but says nothing about the mode of failure. It is the simplest presentation of the failure criterion that can fit the data reasonably well. In view of the significant scatter of the failure test data, cubic of higher order approximation are not employed. Particular cases of the above criterion differ from one another by their strength tensors F_i and F_{ij} (i, j=1, 2, 6). There are various degenerate cases of this criterion such as maximum stress criterion, maximum strain criterion, Tsai-Hill criterion, Hoffman criterion, and Tsai-Wu criterion, etc. In this thesis, maximum stress criterion, Hoffman criterion, and Tsai-Wu criterion are applied in progressive failure analysis. These criteria are introduced in detail below.

(1) Maximum stress criterion:

Maximum stress criterion (PMSC) is an independent failure criterion. It is based on the fact that there is no interaction between modes of the failure. As for this criterion, the failure is said to have occurred when stresses in principal material directions are greater than or equal to the respective strengths. Tensor polynomial form of this criterion can be obtained by using following tensor strength factors

$$F_1 = \frac{1}{X_t} - \frac{1}{X_c}; \quad F_2 = \frac{1}{Y_t} - \frac{1}{Y_c};$$
$$F_{11} = \frac{1}{X_t X_c}; \quad F_{22} = \frac{1}{Y_t Y_c}; \tag{6.3.3}$$
$$F_{66} = \frac{1}{T^2}; \quad F_{12} = -\frac{F_1 F_2}{2}$$

The remaining strength tensor terms are zero.

In the above expressions, X_t, and Y_t are the tensile strengths of the lamina along and transverse to fiber directions. Xc and Yc are the corresponding compressive strengths. T is the shear strength of lamina in planes 1-2.

(2) Hoffman criterion:

$$F_1 = \frac{1}{X_t} - \frac{1}{X_c}; \quad F_2 = \frac{1}{Y_t} - \frac{1}{Y_c};$$
$$F_{11} = \frac{1}{X_t X_c}; \quad F_{22} = \frac{1}{Y_t Y_c}; \tag{6.3.4}$$
$$F_{66} = \frac{1}{T^2}; \quad F_{12} = -\frac{1}{2}\left(\frac{1}{X_t X_c} + \frac{1}{Y_t Y_c}\right)$$

The remaining strength tensor terms are zero.

(3) Tsai-Wu criterion:

$$F_1 = \frac{1}{X_t} - \frac{1}{X_c}; \quad F_2 = \frac{1}{Y_t} - \frac{1}{Y_c};$$
$$F_{11} = \frac{1}{X_t X_c}; \quad F_{22} = \frac{1}{Y_t Y_c}; \tag{6.3.5}$$
$$F_{66} = \frac{1}{T^2}; \quad F_{12} = -\frac{1}{2}\left(\frac{1}{\sqrt{X_t X_c Y_t Y_c}}\right)$$

The remaining strength tensor terms are zero.

6.4 Linear Progressive Failure

6.4.1 Linear Finite Element Model

In this study, Superelement 2 is first used to predict the progressive failure of TWF panels subjected to uni-axial extension. Linear progressive failure procedure flowchart is shown in Figure 6.4 (a). Two loading cases are considered. The first and ultimate failure loads, maximum extension displacement, locations and the modes of failure are estimated and compared with experimental data.

Loading cases 1 and 2

In progressive failure analysis, the two loading cases (case 1 and case 2) are considered. Case 1 is for longitudinal loading and case 2 is for transverse loading (Figure 6.5).

Figure 6.6 shows the FE model for the model in case 1. This FE model has 12 superelements along X direction and 6 superelements along Y direction. At region B of

the FE model, the deflection in Z direction w of all the nodes is fixed (w = 0) and the displacement u in X direction is assigned a value to simulate displacement tension load. At region D, displacements w and u of all nodes are fixed (w = u = 0). Displacement v in Y direction at node 1 is fixed (v = 0) so as to remove the rigid body motion of the FE model. Note that due to the jagged nature of the elements, there is no clear line where loads are applied or where the constraints are fixed. Rather, there is a region within which all nodes would be subjected to the same condition of loading or fixity. For example, within region B, all nodes that fall within this region would be subjected to the same uniform displacement as mentioned above. Young's modulus of the TWF were determined by

$$E_x = \frac{F/(Wh)}{\varepsilon_x} \tag{6.4.1}$$

where F is tension force loaded at region B of the panel in X direction, h is the nominal thickness, W is the nominal width of the TWF panel and ε_x is the strain along X direction. Force F is obtained by adding reaction forces in X direction at all nodes at region B. Strain ε_x = u (X direction displacement of node at region B) /L. L is distance between regions B and D, shown in Figure 6.6.

For case 2, the FE model is shown in Figure 6.7. The FE model has 6 superelements along X direction and 12 superelements along Y direction. As shown in Figure 6.5, at region A of the FE model, the deflection w of all the nodes is fixed (w = 0) and the displacement v in Y direction is assigned a value to simulate displacement tension load. At region C, displacements w and v of all nodes are fixed (w = v = 0). Displacement u in

X direction at node 1 is fixed (u = 0) so as to remove the rigid body motion of the FE model. Young's modulus of the TWF were determined by

$$E_y = \frac{F/(Lh)}{\varepsilon_y} \tag{6.4.2}$$

Where F is tension force loaded at region A of the panel in Y direction. Force F is obtained by adding reaction forces in Y direction at all nodes at region A. Strain ε_y = v (Y direction displacement of node at region A) /W.

Geometry and material properties of TWF composites

In analysis, the following geometry and material properties of TWF composites are used. Table 6.1 lists the geometric parameters of the unit cell measured by checking the microscopic photographs of TWF composites. Table 6.3 shows the effective elastic properties of the impregnated yarn obtained by using the Strength-Of-Materials model (SOM) and using fiber and matrix properties of Table 6.2 and the fiber volume fraction V_f = 0.695. Table 6.4 gives the strengths of fibers, matrix, and the impregnated yarns of TWF composites.

Table 6.1: Geometric Parameters

Geometric parameters	Measured values
Yarn thickness (mm)	0.07
w1 (mm)	0.85
w2 (mm)	1.10

Table 6.2: Elastic properties of fibers and matrix

Material	E_L (GPa)	E_T (GPa)	G_{LT} (GPa)	G_{TT} (GPa)	v_{LT}	ρ (gm/cm^3)
Carbon Fiber	500.0	40.0	24.0	14.3	0.26	2.10
Epoxy Resin	3.5	3.5	1.3	1.3	0.35	1.17

Table 6.3: Elastic properties of the impregnated yarn of TWF composites

Material	E_L (Gpa)	E_T (GPa)	G_{LT} (GPa)	v_{LT}	v_{TT}	V_f	ρ (gm/cm^3)
Carbon/epoxy	338.57	12.40	5.61	0.287	0.437	0.695	1.8164

Table 6.4: Strength properties of impregnated yarn of TWF composites

Strength roperties	Yarn (MPa)	Matrix (MPa)
X_t	3400	68.9
X_c	3400	68.9
Y_t	68.9	68.9
Y_c	68.9	68.9
S	86.9	86.9

In Table 6.4, X_t and Y_t are the tensile strengths of yarn along the fiber direction and the transverse to the fiber direction. X_c and Y_c are the corresponding compressive strengths. S is shear strength of yarn in plane 1-2.

6.4.2 Results and discussion of linear failure analysis

Figure 6.8 shows the curves of nominal stress σ_x and strain ε_x of 12 by 6 panel in loading case 1 and experimental data. These curves are calculated using maximum stress criterion, Hoffman criterion and Tsai-Wu criterion. Figure 6.9 shows the curves of nominal Young's modulus E_x and strain ε_x of 12 by 6 panel in loading case 1.

In Figure 6.8, it is observed that numerical results coincide well with the experimental data at low loads. As load increases, the difference between them becomes large because the experimental curve has a trend to be gradually stiffened. This situation can be

explained by the straightening of the undulation of the yarns. The yarns become stiffer as they are more and more straightened. This means that progressive failure of TWF panel is a typical structural nonlinear behavior. The current progressive failure procedure is unable to model this situation because the nonlinearity of the matrix and yarn is not taken into account in this study. The current finite element model (superelement 2) used in this study is linear element and do not allow for effects of large displacements and updating structure in analysis. It is not suited for largely deformed structural analysis. It is unable to describe this structural stiffening behavior of the TWF panel. That makes the numerical solution more and more different from the experimental data as load increases. Therefore, a nonlinear element model has to be developed to deal with TWF structural stiffening problems.

In Figure 6.9, as load increases and some failures occur, Young's modulus E_x reduces a little till ultimate failure occurs. At ultimate failure, Young's modulus E_x descends quickly.

Figure 6.10 shows the curves of nominal stress σ_y and strain ε_y of 6 by 12 panel in loading case 2, using three criteria. Figure 6.11 shows the curves of Young's modulus E_y and strain ε_y of 6 by 12 panel in loading case 2. In Figures 6.10 and 6.11, there is a small difference between the curves obtained using three failure criteria. The differences from case 1 are, first failure load and ultimate failure load in Y direction are much less than ones in X direction, and those are only about a third as much as ones in X direction. During loading after first failure, the modulus E_y has a decline at nominal strain ε_y $=1.6\times10^{-3}$ (see Figure 6.11). That is because there are more failures occurring at this load.

6.5 Nonlinear Progressive Failure

6.5.1 Nonlinear finite element model

There is an essential difference in mechanical behavior (strain-stress curves) given respectively by the linear results and experimental data (see Figure 6.8). The experimental curve has a trend to be gradually stiffened. As load increases, Young's modulus gradually increases. This situation results from the straightening of the undulation of the yarns. The yarns become stiffer as they are more and more straightened. However, the curve from the linear results does not have this situation. As such, as load increases, Young's modulus from FEM gradually decreases. This is because Superelement 2 is linear element and involves small displacement assumption. All displacements and stresses are calculated based on originally undeformed undulated yarns. As load increases, yarns are straightened more and more. But the displacements are still calculated based on originally undeformed undulated yarns rather than the updated structure. That results in the difference between the calculation and the experiment. So Superelement 2 can only model the small deformation deviating from the originally undulated yarns and cannot model the straightening of the undulation of the yarns. That indicates that Superelement 2 does not exactly model the failure procedure of TWF panels with effects of large displacements. Therefore, it is necessary to develop a nonlinear element model to deal with large displacement TWF problems.

In this section, a nonlinear superelement is developed for large deformation analysis of TWF composites. In this superelement, geometrical nonlinearity is considered. The

stress-strain relations of yarns and matrix include the components of squared derivatives of displacements. This superelement is applied on a unit cell. It is constructed of six 16-node nonlinear isoparametric elements and nine 8-node nonlinear isoparametric elements. A 16-node nonlinear isoparametric element is used to model a yarn part. Three 8-node nonlinear isoparametric elements are combined together to model a crossover part. The assembly is done by the pseudo element technique. After internal node DOF condensation, this superelement has 15-node and 12 DOFs at each node. Details on formula of 16-node nonlinear isoparametric element and 8-node nonlinear isoparametric element can be seen in section 6.5.2.

In this nonlinear superelement model, large displacements and small strains are taken into account. Total Lagrange description is applied. Newton iterative method is used to solve for nonlinear algebraic equations. It is an iterative procedure of geometry update and linear solution. In analysis, loading and boundary constraints are imposed by using Lagrange multiplier method. It is noted that this superelement is actually Superelement 2 with consideration of large displacements.

In nonlinear progressive failure analysis, two displacement-loading cases are considered (see Figure 6.5). The geometry, material properties and strength of TWF composites listed in Table 6.1, 6.2, 6.3 and 6.4 are used. The geometrical nonlinearity of the matrix and yarns is taken into account and the model updates the geometry of the TWF panel at each load step. Nonlinear progressive failure procedure flowchart is shown in Figure 6.4 (b).

6.5.2 16 node nonlinear isoparametric element for a yarn part

A total Lagrange formula is used. Large displacement and small strain are considered.

(1) Displacement fields

$$\begin{Bmatrix} u \\ v \\ w \end{Bmatrix} = \sum_{i=1}^{16} [N_i] \begin{Bmatrix} u_i \\ v_i \\ w_i \end{Bmatrix} = [N]\{d\}$$
$$\begin{Bmatrix} x \\ y \\ z \end{Bmatrix} = \sum_{i=1}^{16} [N_i] \begin{Bmatrix} x_i \\ y_i \\ z_i \end{Bmatrix} \qquad (6.5.1)$$

where

$$\{d\} = [u_1 \quad v_1 \quad w_1 \quad \cdots \quad u_{16} \quad v_{16} \quad w_{16}]^T$$

$$[N] = [[N_1] \quad [N_2] \quad \cdots \quad [N_{16}]]$$

$$[N_i] = \begin{bmatrix} N_i & 0 & 0 \\ 0 & N_i & 0 \\ 0 & 0 & N_i \end{bmatrix}$$

(2) Nonlinear strain-displacement relations

$$\{\varepsilon\}=\begin{Bmatrix}\varepsilon_x\\ \varepsilon_y\\ \varepsilon_z\\ \varepsilon_{yz}\\ \varepsilon_{xz}\\ \varepsilon_{xy}\end{Bmatrix}=\begin{Bmatrix}\dfrac{\partial u}{\partial x}+\dfrac{1}{2}\left[\left(\dfrac{\partial u}{\partial x}\right)^2+\left(\dfrac{\partial v}{\partial x}\right)^2+\left(\dfrac{\partial w}{\partial x}\right)^2\right]\\ \dfrac{\partial v}{\partial y}+\dfrac{1}{2}\left[\left(\dfrac{\partial u}{\partial y}\right)^2+\left(\dfrac{\partial v}{\partial y}\right)^2+\left(\dfrac{\partial w}{\partial y}\right)^2\right]\\ \dfrac{\partial w}{\partial z}+\dfrac{1}{2}\left[\left(\dfrac{\partial u}{\partial z}\right)^2+\left(\dfrac{\partial v}{\partial z}\right)^2+\left(\dfrac{\partial w}{\partial z}\right)^2\right]\\ \dfrac{\partial v}{\partial z}+\dfrac{\partial w}{\partial y}+\dfrac{\partial u}{\partial y}\dfrac{\partial u}{\partial z}+\dfrac{\partial v}{\partial y}\dfrac{\partial v}{\partial z}+\dfrac{\partial w}{\partial y}\dfrac{\partial w}{\partial z}\\ \dfrac{\partial u}{\partial z}+\dfrac{\partial w}{\partial x}+\dfrac{\partial u}{\partial x}\dfrac{\partial u}{\partial z}+\dfrac{\partial v}{\partial x}\dfrac{\partial v}{\partial z}+\dfrac{\partial w}{\partial x}\dfrac{\partial w}{\partial z}\\ \dfrac{\partial u}{\partial y}+\dfrac{\partial v}{\partial x}+\dfrac{\partial u}{\partial x}\dfrac{\partial u}{\partial y}+\dfrac{\partial v}{\partial x}\dfrac{\partial v}{\partial y}+\dfrac{\partial w}{\partial x}\dfrac{\partial w}{\partial y}\end{Bmatrix}=\{\varepsilon_L\}+\{\varepsilon_N\} \tag{6.5.2}$$

where $\{\varepsilon_L\}$ is linear part of strain. $\{\varepsilon_N\}$ is nonlinear part of strain.

$$\{\varepsilon_L\}=\sum_{i=1}^{16}[B_i]\{d_i\}=[B]\{d\} \tag{6.5.3}$$

where

$$[B_i]=\begin{bmatrix}\dfrac{\partial N_i}{\partial x} & 0 & 0\\ 0 & \dfrac{\partial N_i}{\partial y} & 0\\ 0 & 0 & \dfrac{\partial N_i}{\partial z}\\ 0 & \dfrac{\partial N_i}{\partial z} & \dfrac{\partial N_i}{\partial y}\\ \dfrac{\partial N_i}{\partial z} & 0 & \dfrac{\partial N_i}{\partial x}\\ \dfrac{\partial N_i}{\partial y} & \dfrac{\partial N_i}{\partial x} & 0\end{bmatrix},\quad \{d_i\}=\begin{Bmatrix}u_i\\ v_i\\ w_i\end{Bmatrix}$$

$$[B]=[[B_1]\ \ [B_2]\ \ \cdots\ \ [B_{16}]]$$

$$\{\varepsilon_N\} = \frac{1}{2}\begin{bmatrix} \frac{\partial u}{\partial x} & 0 & 0 & \frac{\partial v}{\partial x} & 0 & 0 & \frac{\partial w}{\partial x} & 0 & 0 \\ 0 & \frac{\partial u}{\partial y} & 0 & 0 & \frac{\partial v}{\partial y} & 0 & 0 & \frac{\partial w}{\partial y} & 0 \\ 0 & 0 & \frac{\partial u}{\partial z} & 0 & 0 & \frac{\partial v}{\partial z} & 0 & 0 & \frac{\partial w}{\partial z} \\ 0 & \frac{\partial u}{\partial z} & \frac{\partial u}{\partial y} & 0 & \frac{\partial v}{\partial z} & \frac{\partial v}{\partial y} & 0 & \frac{\partial w}{\partial z} & \frac{\partial w}{\partial y} \\ \frac{\partial u}{\partial z} & 0 & \frac{\partial u}{\partial x} & \frac{\partial v}{\partial z} & 0 & \frac{\partial v}{\partial x} & \frac{\partial w}{\partial z} & 0 & \frac{\partial w}{\partial x} \\ \frac{\partial u}{\partial y} & \frac{\partial u}{\partial x} & 0 & \frac{\partial v}{\partial y} & \frac{\partial v}{\partial x} & 0 & \frac{\partial w}{\partial y} & \frac{\partial w}{\partial x} & 0 \end{bmatrix} \begin{Bmatrix} \frac{\partial u}{\partial x} \\ \frac{\partial u}{\partial y} \\ \frac{\partial u}{\partial z} \\ \frac{\partial v}{\partial x} \\ \frac{\partial v}{\partial y} \\ \frac{\partial v}{\partial z} \\ \frac{\partial w}{\partial x} \\ \frac{\partial w}{\partial y} \\ \frac{\partial w}{\partial z} \end{Bmatrix} = \frac{1}{2}[H]\{g\} \tag{6.5.4}$$

First and second variations of the nonlinear part of strain are given by

$$\delta\{\varepsilon_N\} = [H]\delta\{g\} \tag{6.5.5}$$

$$\delta^2\{\varepsilon_N\} = \delta[H]\delta\{g\} \tag{6.5.6}$$

where

$$\{g\}=\begin{bmatrix} \frac{\partial N_1}{\partial x} & 0 & 0 & & \frac{\partial N_{16}}{\partial x} & 0 & 0 \\ \frac{\partial N_1}{\partial y} & 0 & 0 & & \frac{\partial N_{16}}{\partial y} & 0 & 0 \\ \frac{\partial N_1}{\partial z} & 0 & 0 & & \frac{\partial N_{16}}{\partial z} & 0 & 0 \\ 0 & \frac{\partial N_1}{\partial x} & 0 & & 0 & \frac{\partial N_{16}}{\partial x} & 0 \\ 0 & \frac{\partial N_1}{\partial y} & 0 & \cdots & 0 & \frac{\partial N_{16}}{\partial y} & 0 \\ 0 & \frac{\partial N_1}{\partial z} & 0 & & 0 & \frac{\partial N_{16}}{\partial z} & 0 \\ 0 & 0 & \frac{\partial N_1}{\partial x} & & 0 & 0 & \frac{\partial N_{16}}{\partial x} \\ 0 & 0 & \frac{\partial N_1}{\partial y} & & 0 & 0 & \frac{\partial N_{16}}{\partial y} \\ 0 & 0 & \frac{\partial N_1}{\partial z} & & 0 & 0 & \frac{\partial N_{16}}{\partial z} \end{bmatrix}\{d\}=[S]\{d\}$$

(3) Total potential energy:

$$\begin{aligned} \Pi &= \frac{1}{2}\int_v \{\varepsilon\}^T [Q]\{\varepsilon\}dv - W \\ &= \frac{1}{2}\int_v \left(\{\varepsilon_L\}^T + \{\varepsilon_N\}^T\right)[Q](\{\varepsilon_L\}+\{\varepsilon_N\})dv - W \\ &= \frac{1}{2}\int_v \{\varepsilon_L\}^T [Q]\{\varepsilon_L\}dv + \int_v \{\varepsilon_L\}^T [Q]\{\varepsilon_N\}dv + \frac{1}{2}\int_v \{\varepsilon_N\}^T [Q]\{\varepsilon_L\}dv - W \\ &= U_L + U_{N1} + U_{N2} - W \end{aligned} \tag{6.5.7}$$

(4) First and second variations of total potential energy:

(a) Linear part:

$$U_L = \frac{1}{2}\int_v \{\varepsilon_L\}^T [Q]\{\varepsilon_L\} dv = \{d\}^T \left(\frac{1}{2}\int_v [B]^T [Q][B] dv\right)\{d\} \tag{6.5.8}$$

$$\delta U_L = \delta\{d\}^T \left(\int_v [B]^T [Q][B] dv\right)\{d\} \tag{6.5.9}$$

$$\delta^2 U_L = \delta\{d\}^T \left(\int_v [B]^T [Q][B] dv\right)\delta\{d\} \tag{6.5.10}$$

(b) Nonlinear part 1:

$$U_{N1} = \int_v \{\varepsilon_L\}^T [Q]\{\varepsilon_N\} dv \tag{6.5.11}$$

$$\begin{aligned}\delta U_{N1} &= \int_v \delta\{\varepsilon_L\}^T [Q]\{\varepsilon_N\} dv + \int_v \delta\{\varepsilon_N\}^T [Q]\{\varepsilon_L\} dv \\ &= \delta\{d\}^T \left(\frac{1}{2}\int_v [B]^T [Q][H][S] dv\right)\{d\} + \delta\{d\}^T \left(\frac{1}{2}\int_v [S]^T [H]^T [Q][B] dv\right)\{d\}\end{aligned} \tag{6.5.12}$$

$$\begin{aligned}\delta^2 U_{N1} &= \int_v \delta\{\varepsilon_L\}^T [Q]\delta\{\varepsilon_N\} dv + \int_v \delta\{\varepsilon_N\}^T [Q]\delta\{\varepsilon_L\} dv + \int_v \delta^2\{\varepsilon_N\}^T [Q]\{\varepsilon_L\} dv \\ &= \delta\{d\}^T \left(\int_v [B]^T [Q][H][S] dv\right)\delta\{d\} + \delta\{d\}^T \left(\int_v [S]^T [H]^T [Q][B] dv\right)\delta\{d\} \\ &\quad + \delta\{d\}^T \left(\int_v [S]^T [\bar{\sigma}_L][Q][S] dv\right)\delta\{d\}\end{aligned} \tag{6.5.13}$$

where

$$\{\sigma_L\} = [Q]\{\varepsilon_L\}$$

$$[\bar{\sigma}_L]=\begin{bmatrix} \sigma_{L1} & \sigma_{L6} & \sigma_{L5} & & & & & & \\ \sigma_{L6} & \sigma_{L2} & \sigma_{L4} & & 0 & & & 0 & \\ \sigma_{L5} & \sigma_{L4} & \sigma_{L3} & & & & & & \\ & & & \sigma_{L1} & \sigma_{L6} & \sigma_{L5} & & & \\ & 0 & & \sigma_{L6} & \sigma_{L2} & \sigma_{L4} & & 0 & \\ & & & \sigma_{L5} & \sigma_{L4} & \sigma_{L3} & & & \\ & & & & & & \sigma_{L1} & \sigma_{L6} & \sigma_{L5} \\ & 0 & & & 0 & & \sigma_{L6} & \sigma_{L2} & \sigma_{L4} \\ & & & & & & \sigma_{L5} & \sigma_{L4} & \sigma_{L3} \end{bmatrix}$$

(c) Nonlinear part 2:

$$U_{N2}=\frac{1}{2}\int_v\{\varepsilon_N\}^T[Q]\{\varepsilon_N\}dv \tag{6.5.14}$$

$$\delta U_{N2}=\int_v\delta\{\varepsilon_N\}^T[Q]\{\varepsilon_N\}dv=\delta\{d\}^T\left(\frac{1}{2}\int_v[S]^T[H]^T[Q][H][S]dv\right)\{d\} \tag{6.5.15}$$

$$\begin{aligned}\delta^2U_{N2}&=\int_v\delta\{\varepsilon_N\}^T[Q]\delta\{\varepsilon_N\}dv+\int_v\delta^2\{\varepsilon_N\}^T[Q]\{\varepsilon_N\}dv\\&=\delta\{d\}^T\left(\int_v[S]^T[H]^T[Q][H][S]dv\right)\delta\{d\}+\delta\{d\}^T\left(\int_v[S]^T[\bar{\sigma}_N][Q][S]dv\right)\delta\{d\}\end{aligned} \tag{6.5.16}$$

where

$$\{\sigma_N\}=[Q]\{\varepsilon_N\}$$

$$[\bar{\sigma}_N]=\begin{bmatrix} \sigma_{N1} & \sigma_{N6} & \sigma_{N5} & & & & & & \\ \sigma_{N6} & \sigma_{N2} & \sigma_{N4} & & 0 & & & 0 & \\ \sigma_{N5} & \sigma_{N4} & \sigma_{N3} & & & & & & \\ & & & \sigma_{N1} & \sigma_{N6} & \sigma_{N5} & & & \\ & 0 & & \sigma_{N6} & \sigma_{N2} & \sigma_{N4} & & 0 & \\ & & & \sigma_{N5} & \sigma_{N4} & \sigma_{N3} & & & \\ & & & & & & \sigma_{N1} & \sigma_{N6} & \sigma_{N5} \\ & 0 & & & 0 & & \sigma_{N6} & \sigma_{N2} & \sigma_{N4} \\ & & & & & & \sigma_{N5} & \sigma_{N4} & \sigma_{N3} \end{bmatrix}$$

From first variation of total potential energy, stiffness matrix can be obtained as follows

$$[K]=\begin{bmatrix} \left(\int_v [B]^T[Q][B]dv\right)+ \\ \left(\frac{1}{2}\int_v [B]^T[Q][H][S]dv\right)+\left(\frac{1}{2}\int_v [S]^T[H]^T[Q][B]dv\right)+ \\ \left(\frac{1}{2}\int_v [S]^T[H]^T[Q][H][S]dv\right) \end{bmatrix} \tag{6.5.17}$$

From second variation of total potential energy, tangent stiffness matrix can be obtained as follows

$$[K_T]=\begin{bmatrix} \left(\int_v [B]^T[Q][B]dv\right)+ \\ \left(\int_v [B]^T[Q][H][S]dv\right)+\left(\int_v [S]^T[H]^T[Q][B]dv\right)+\left(\int_v [S]^T[\bar{\sigma}_L][Q][S]dv\right)+ \\ \left(\int_v [S]^T[H]^T[Q][H][S]dv\right)+\left(\int_v [S]^T[\bar{\sigma}_N][Q][S]dv\right) \end{bmatrix} \tag{6.5.18}$$

(5) Finite element equilibrium equations and Newton iterative formula

With element stiffness matrix and tangent matrix, finite element equilibrium equations and Newton iterative formula can be given as follows

(a) Finite element equilibrium equations:

$$[K]\{d\}=\{p\} \tag{6.5.19}$$

where load vector {p} is obtained from work variation $\delta W=\delta\{d\}^T\{p\}$.

(b) Newton iterative formula:

$$\left[K_T{}^m\right]\left\{\Delta d^{m+1}\right\}=\{p\}-\left[K^m\right] \tag{6.5.20}$$

$$\left\{d^{m+1}\right\}=\left\{d^m\right\}+\left\{\Delta d^{m+1}\right\} \tag{6.5.21}$$

Convergence criterion:

$$\left\{\Delta d^{m+1}\right\}^T\left\{\Delta d^{m+1}\right\}\le\varepsilon \tag{6.5.22}$$

where m is iterative number. E is a small positive value.

A cross part is constructed of three layers. Each layer can be modeled by 8 node nonlinear isoparametric element. Formulas of 8 node nonlinear isoparametric element are similar with ones of 16 node nonlinear isoparametric element. In above formulas, if number 16 is replaced with number 8, we will obtain 8 node nonlinear isoparametric element for any layer of a cross part.

6.5.3 Results and discussion of nonlinear failure analysis

Figure 6.12 shows nonlinear response curve (stress σ_x vs strain ε_x) of 12 by 6 panel in loading case 1 and experimental curve. This response curve is calculated using the nonlinear finite element (named NFE) without consideration of failure criteria. It is seen that the response curve has a stiffened trend like the experimental curve. As load increases, the panel is gradually stiffened and its Young's modulus increases gradually. The response curve coincides very well with the experimental curve. That shows the nonlinear FE suggested here can fully model the real deformation process of TWF panel.

Table 6.5 lists the progressive failure results of 12 by 6 panel in loading case 1 and experimental data. In Table 6.5, first failure load is load intensity (i.e., nominal stress σ_x) applied on the panel when the first failure of the panel takes place. Ultimate failure load is maximum load intensity the panel can bear. Location of first failure includes the number of three items: superelement (Se), element (El), and layer. Those indicate at which superelement, at which element, and at which layer first failure occurs. The elements of a superelement are numbered as shown in Figure 6.3. Mode of first failure is failure mode when first failure happens during loading. As stated before, there are three failure modes. Failure mode 1 is fiber failure because σ_1 is the failure causing stress. Failure mode 2 corresponds to the transverse mode of failure (failure due to in-plane normal stresses transverse to the fiber direction), failure model 6 to τ_{12} (in-plane shear) mode of failure.

Figure 6.13 shows the curves of nominal stress σ_x and strain ε_x of 12 by 6 panel in loading case 1 and experimental data. These curves are calculated using NFE with

maximum stress criterion, Hoffman criterion and Tsai-Wu criterion. It is observed that different from linear results (Figure 6.8), in entire loading procedure these curves have good agreement with the experiment curve. The ultimate failure loads obtained using three failure criteria are closer to the experimental failure load. For mode of first failure, they are all the transverse mode of failure. The first and ultimate failure loads using Hoffman and maximum stress criteria are less than the ones using Tsai-Wu criterion. The latter one is closer to the experiment.

Figure 6.14 shows the curves of nominal Young's modulus E_x and strain ε_x of 12 by 6 panel in loading case 1. It is observed that there is big difference between linear and nonlinear results. As load increases, Young's modulus E_x gradually increases to some value and then decreases. At ultimate failure, Young's modulus E_x begins descending quickly. In Figure 6.13, the TWF panel behaves almost linearly up to its maximum load carrying ability and then loses its load carrying ability quickly. That means before ultimate failure, the TWF panel can still work like before first failure occurs. The TWF panel strength should be decided by ultimate failure rather than first failure. From Table 6.5, it is estimated that ultimate failure load is about 2 times as much as first failure load. If ultimate failure load were considered to determine the strength in TWF structural design, great potential TWF load carrying ability would not be wasted.

Table 6.5: Nonlinear progressive failure results of 12 by 6 panel in case 1

Failure Criteria	First failure load (N/m^2)	Location of first failure (Se, El, Layer)	Mode of first failure	Ultimate failure load (N/m^2)
Hoffman	8.0227×10^7	(37, 5, 1)	σ_2	1.7718×10^8
PMSC	1.0376×10^8	(13, 4, 1)	σ_2	1.8996×10^8
Tsai-Wu	1.2837×10^8	(13, 4, 1)	σ_2	2.3609×10^8
Experiment	-	-	-	2.394×10^8

Table 6.6: Nonlinear progressive failure results of 12 by 6 panel in case 2

Failure Criteria	First failure load (N/m^2)	Location of first failure (Se, El, Layer)	Mode of first failure	Ultimate failure load (N/m^2)
Hoffman	3.3937×10^7	(7, 7, 1)	σ_2	7.4361×10^7
PMSC	3.3937×10^7	(7, 7, 1)	σ_2	7.4518×10^7
Tsai-Wu	3.3937×10^7	(7, 7, 1)	σ_2	7.4518×10^7
Experiment	-	-	-	10.89×10^7

Figure 6.15 shows the curves of nominal stress σ_y and strain ε_y of 6 by 12 panel in loading case 2, using three criteria. Figure 6.16 shows the curves of Young's modulus E_y and strain ε_y of 6 by 12 panel in loading case 2. Table 6.6 lists the nonlinear progressive failure results of 6 by 12 panel in loading case 2. In Figures 6.15 and 6.16, there is a small difference between the curves obtained using three failure criteria. For first failure, they are all transverse modes of failure. Initial load step shares the same value and ultimate load step has a little difference. The ultimate failure load is about 3.1 times as

much as the first failure load. Compared with experiment data, there is round 20% difference for ultimate failure load (See Table 6.6). After first failure load, the TWF panel still has great potential load carrying ability. The difference from case 1 is, whether first failure load or ultimate failure load in Y direction is much less than ones in X direction, only about a third as much as ones in X direction. During loading after first failure, the modulus E_y has a decline at nominal strain $\varepsilon_y = 1.5\times10^{-3}$ (see Figure 6.16). It is because there are more micro-cracks occurring at this load. That leads the modulus E_y to begin an obvious decline at this load.

6.6 Conclusions

Progressive failure of TWF panels subjected to extension loading is investigated numerically and experimentally. In numerical study, TWF panel is discretized respectively using linear superelement 2 and nonlinear Super-Finite-Elements proposed here. Hoffman, maximum stress and Tsai-Wu failure criteria are used to predict the failure load and failure mode. There are several conclusions that can be drawn from the analytical and experimental results.

(1) Numerical results from the nonlinear super-finite-element model coincide with the experimental data. It appears that the nonlinear super-finite-element model along with the progressive failure procedure suggested herein are feasible for the failure analysis of TWF composites.

(2) The curve of nominal stress vs. strain of TWF panel has a trend to be gradually

stiffened. Young's modulus changes during loading. As load increases, they gradually increase and then decrease quickly because of ultimate failure. This situation is proven by the experiment and the nonlinear failure procedure. This situation can be explained by the straightening of the undulation of the yarns. The yarns become stiffer as they are more and more straightened.

(3) The linear failure procedure is unable to model this situation because the geometrical nonlinearity of the matrix and yarn is not taken into account. It is not applicable for the failure analysis of TWF composites.

(4) In numerical study, it is found that there is a small difference between the curves obtained using three failure criteria. Tsai-Wu criteria may give better results than Hoffman and Maximum stress criteria.

(5) Before ultimate failure, the TWF panel can work like before first failure occurs. Ultimate failure load is about 2 to 3 times as much as first failure load. After first failure, the TWF panel still has great potential load carrying ability.

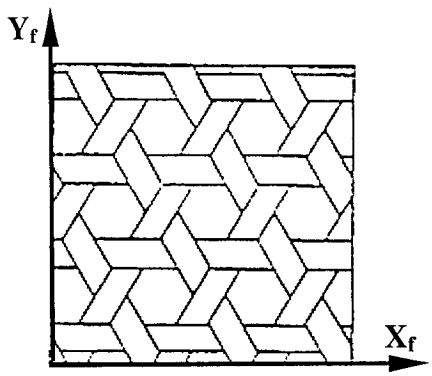

Figure 6.1: Triaxial woven fabric

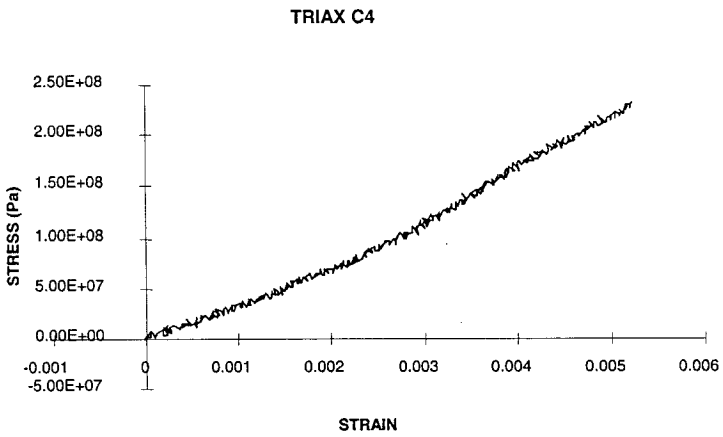

Figure 6.2: Stress-strain curve of the TWF in the longitudinal direction

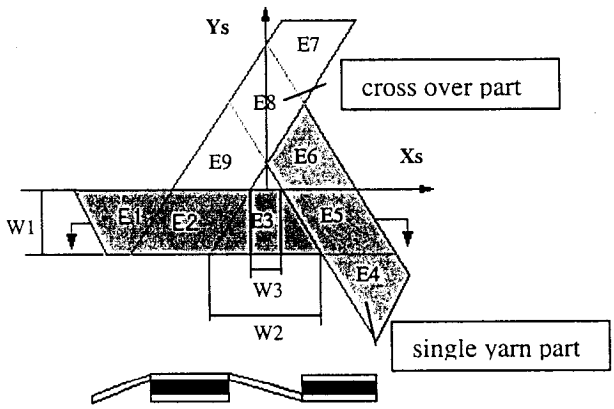

Figure 6.3: A unit cell (superelement)

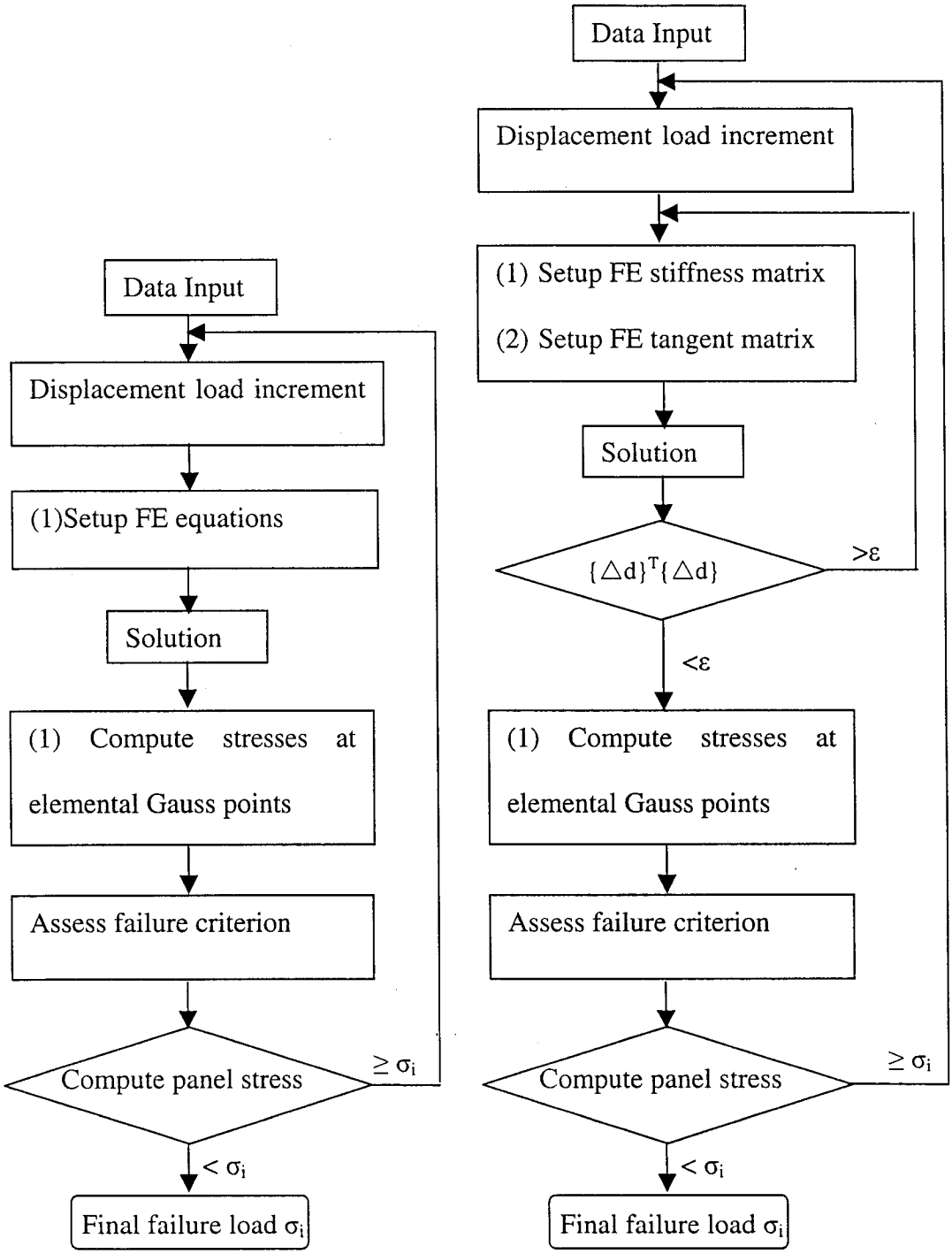

(a) Linear (b)Nonlinear

Figure 6.4: Program flowchart of linear and nonlinear failure procedures

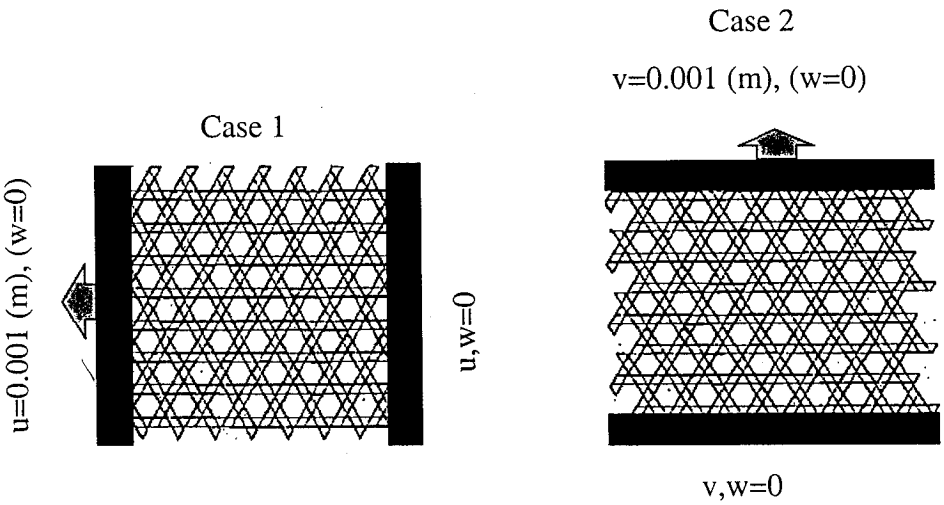

Figure 6.5: Two cases of loading

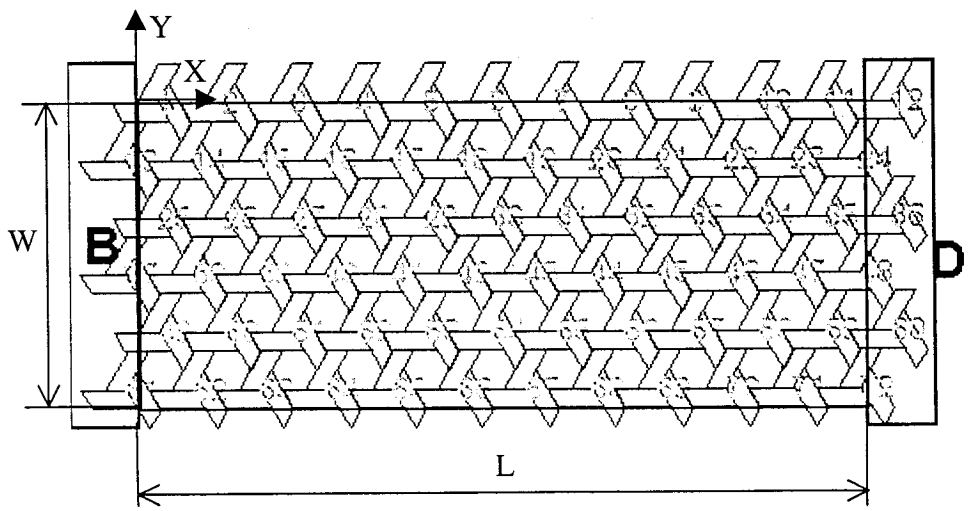

Figure 6.6: Finite element model for case 1

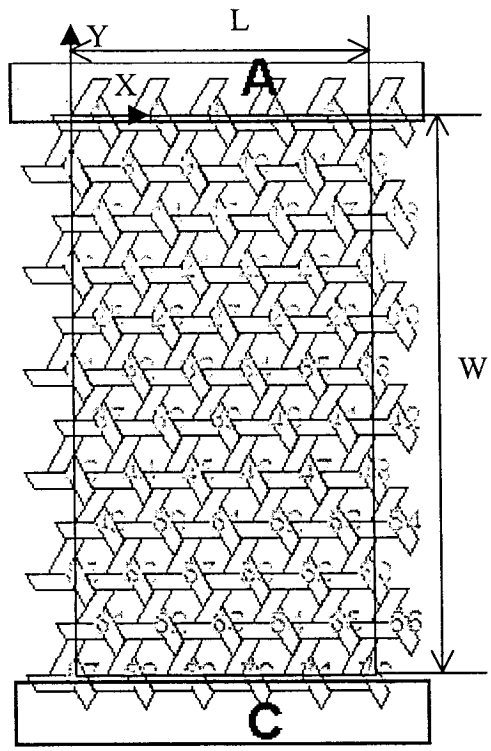

Figure 6.7: Finite element model for case 2

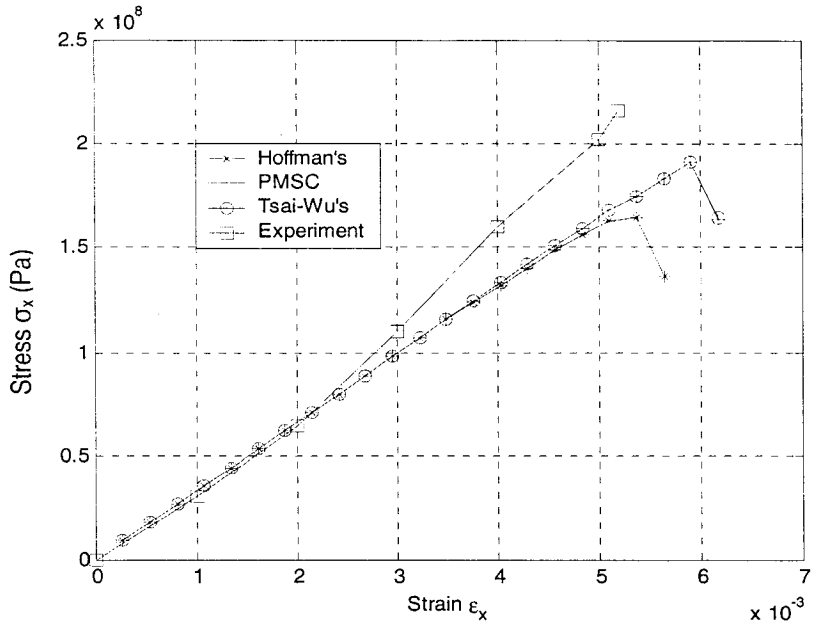

Figure 6.8: Stress-strain curves of 12 by 6 panel in case 1

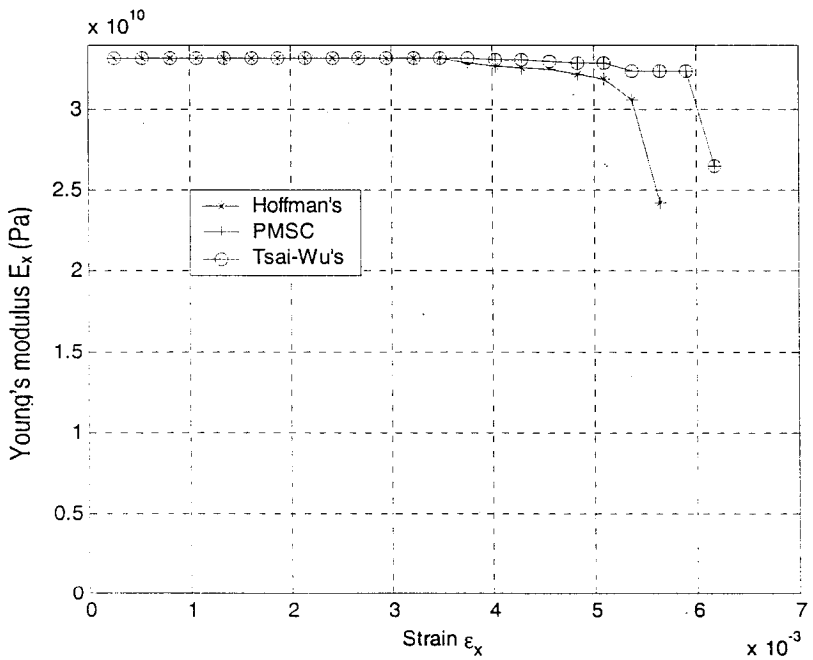

Figure 6.9: Young's modulus E_1 vs. strain ε_x of 12 by 6 panel in case 1

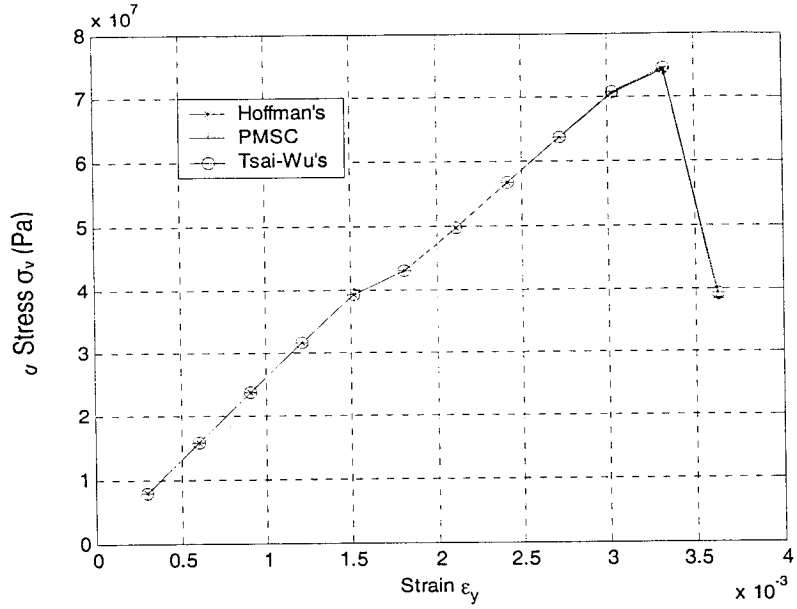

Figure 6.10: Stress σ_y vs. strain ε_y of 6 by 12 panel in case 2

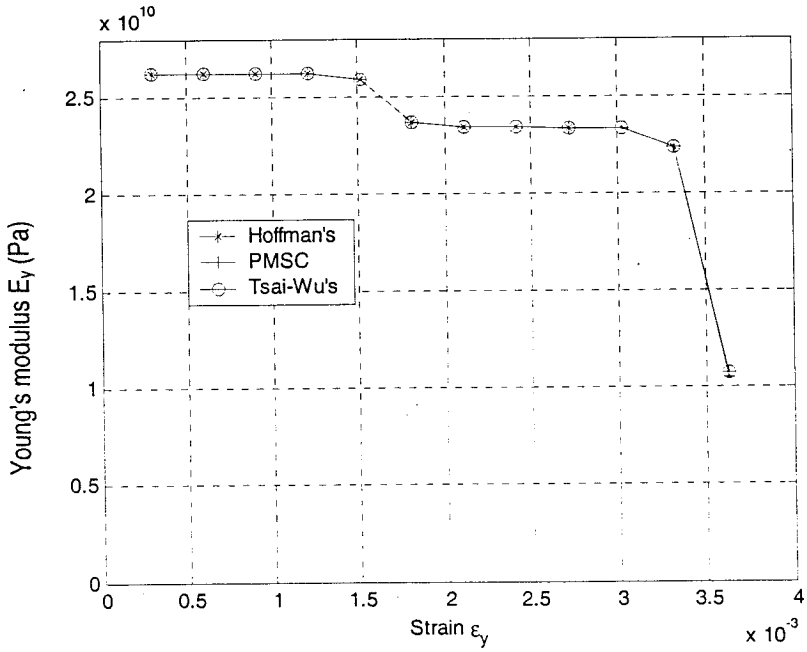

Figure 6.11: Young's modulus E_y vs. strain ε_y of 6 by 12 panel in case 2

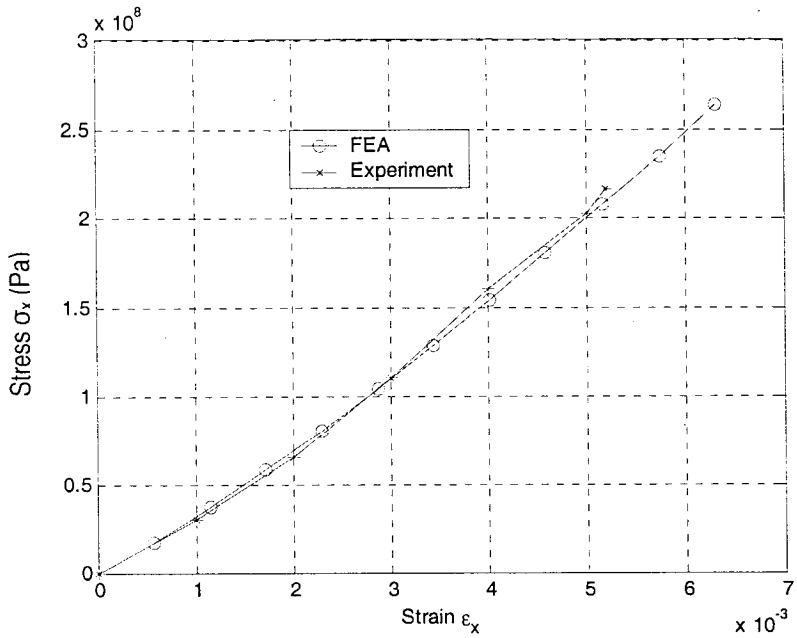

Figure 6.12: Comparison of NFEA results and experiment

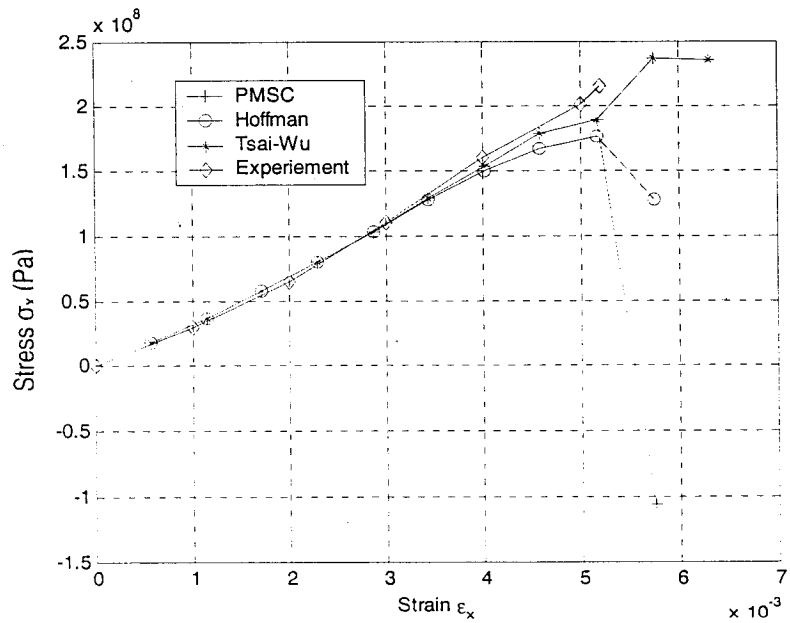

Figure 6.13: Stress σ_x vs. strain ε_x of 12 by 6 panel in case 1 using NFEA

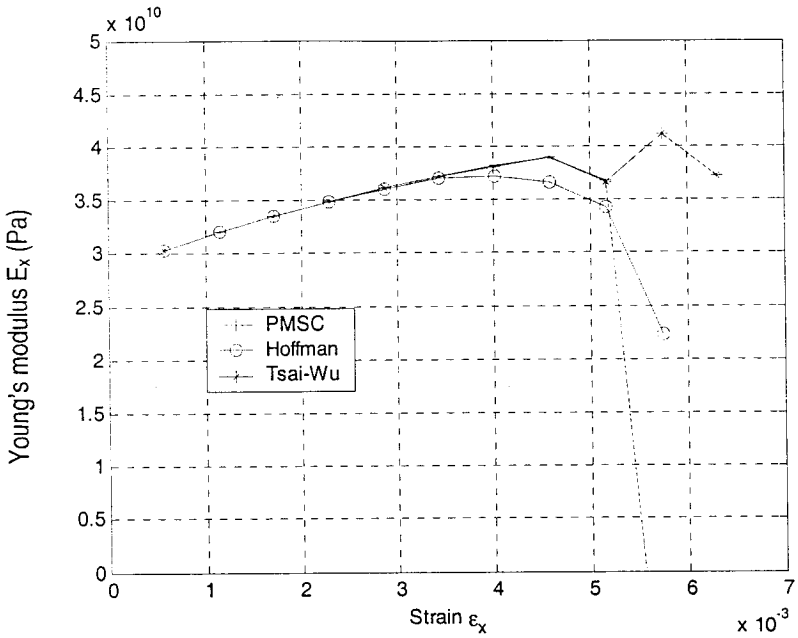

Figure 6.14: Young's modulus E_x vs. strain ε_x of 12 by 6 panel in case 1 using NFEA

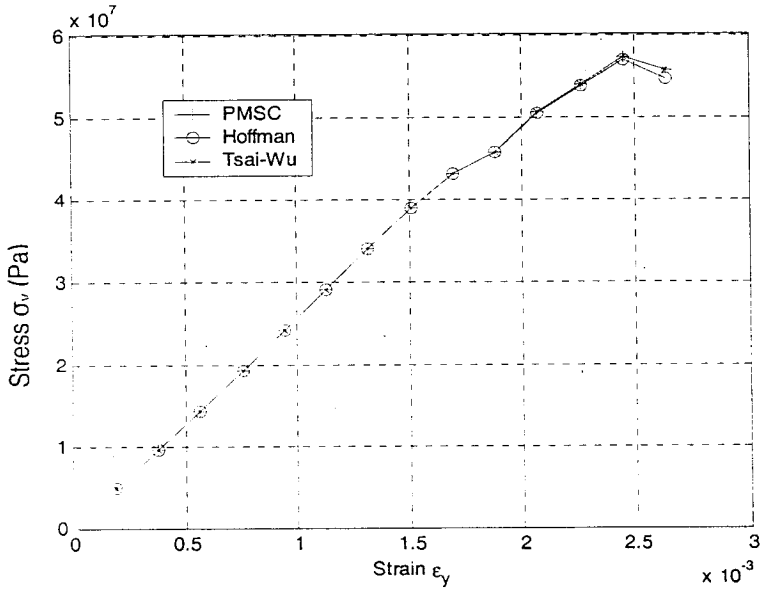

Figure 6.15: Stress σ_y vs. strain ε_y of 6 by12 panel in case 2 using NFEA

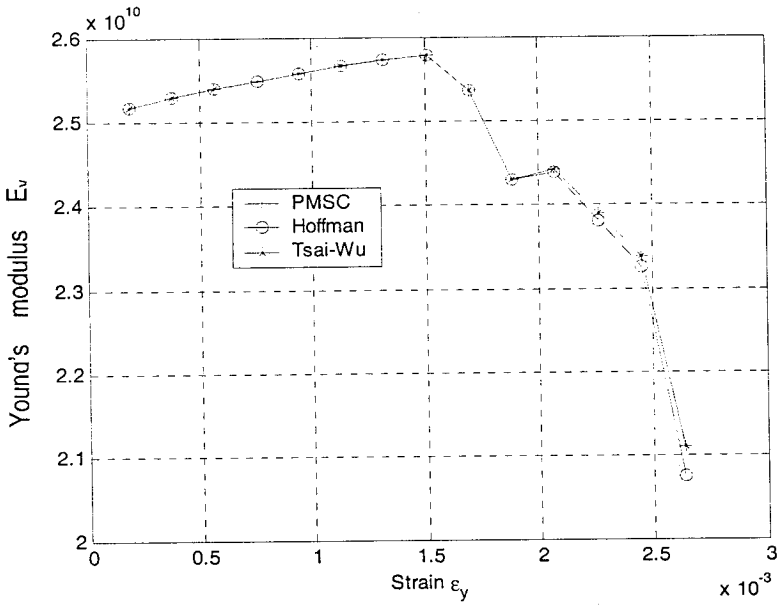

Figure 6.16: Young's modulus E_y vs. strain ε_y of 6 by12 panel in case 2 using NFEA

Chapter 7

Contributions and Suggestion for Future work

In this thesis, following have been developed:

- Two finite element models (Superelement 1 and Superelement 2) are developed for prediction of mechanical behavior of TWF composites. Nonlinear finite element model is also developed. Actually it is Superelement 2 with consideration of large displacements.

- Elastic constants of the TWF composites are evaluated using a series of experiments and finite element analysis. The effects of sizes and aspect ratios of TWF panels on their Young's modulus and Poisson's ratio are studied using finite element analysis.

- Thermal deformation behavior of TWF composites is modeled using Superelement 2. Thermal deformation behavior and Thermal Expansion Coefficients (TECs) of the TWF composites are evaluated. Effects of the aspect ratios and size of the panels on the TECs are studied.

- The mechanical behavior of a sector of the reflector subjected to uniform

pressure is approached by modeling several different-scale sectors using Super-finite elements.

- Progressive failure of the TWF composite panels subjected to uni-axial extension is studied numerically and experimentally. In numerical study, TWF panel is discretized respectively using linear and nonlinear Super-Finite-Elements proposed here. The first and ultimate failure loads, maximum extension displacement, locations and modes of failure are estimated and compared with experimental data.

This above-mentioned research work can also be checked in a few publications [88-99].

Following future works are suggested:

- Develop practical experiment schemes to verify thermal deformation behavior and to evaluate Thermal Expansion Coefficients (TECs) of the TWF composites.

- Develop hybrid superelements to give more accurate stress distribution of the TWF composites subjected to loads.

References

[1] Ko, F.K. and Chou, T.W. 1989. Composite Materials Series 3 – Textile Structural Composites, Elsevier Science, Amsterdam.

[2] Cox, B.N. and G. Flanagan. 1996. Handbook of analytical methods for textile composites, Rockwell Science Center, Thousand Oaks, CA.

[3] Ishikawa, T. 1980. "Anti-symmetric elastic properties of composite plates of satin weave cloth," Fiber Science Technology, 15:127-145

[4] Ishikawa, T. and T.W.Chou. 1982. "Elastic behavior of woven hybrid composites," Journal of Composite Materials, 16:2-9.

[5] Ishikawa, T. and T.W.Chou. 1983. "One dimensional micro-mechanical analysis of woven fabric composites," AIAA Journal, 21(12):2-9.

[6] Ishikawa, T. and T.W.Chou. 1982. "Stiffness and strength behavior of woven fabric composites," Journal of Material Science, 17:3211-3220.

[7] Ishikawa, T. and T.W.Chou. 1983. "In-plane thermal expansion and thermal bending coefficients of fabric composites," Journal of Composite Materials, 17:92-104.

[8] Ishikawa, T., M. Matsushima and Y. Hayashi. 1985. "Experimental confirmation of the theory of elastic moduli of fabric composites," Journal of Composite Materials,19:443-458.

[9] Tsai, S.W. and H.T. Hahn. 1980. Introduction to composite materials, Technomic Publishing, Lancaster, PA.

[10] Raju, I.S, R.L.Foye and V.S.Avva. 1990. "A review of the analytical methods for fabric and textile composites," in Proceedings of the Indo-U.S. workshop on composites for aerospace application, Part I, July 1990, Bangalor, pp.129-159.

[11] Naik, N.K. and P.S.Shembekar. 1992. "Elastic behavior of woven hybrid composites: I-laminate analysis," Journal of Composite Materials, 26(15): 2197-2225.

[12] Shembekar, P.S. and N.K.Naik. 1992. "Elastic behavior of woven hybrid composites: II-laminate analysis," Journal of Composite Materials, 26(15): 2226-2246.

[13] Naik, N.K. and V.K.Ganesh. 1992. "Prediction of on-axes elastic properties of plain weave fabric composites," Composite Science and Technology, 135-152.

[14] Walsh, T.J. and O.O.Ochoa. 1996. "Analytical and experimental mechanics of woven fabric composites," Journal of Composite Materials and Structures, 3: 133-152.

[15] Ganesh, V.K. and N.K. Naik. 1996. "Failure behavior of plain weave fabric composites under on-axis uniaxial tensile loading: I Laminate geometry," Journal of Composite Materials, 30(16):1748-1778.

[16] Naik, N.K. and V.K.Ganesh. 1996. "Failure behavior of plain weave fabric composites under on-axis uniaxial tensile loading: I Laminate geometry," Journal of Composite Materials, 30(16):1779-1822.

[17] Naik, R.A. 1995. "Failure analysis of woven and braided fabric reinforce composites," Journal of Composite Materials, 29(17): 2342-2363.

[18] Foye, R.L. 1992. "Finite element analysis of the stiffness of fabric reinforced composites," NASA contractor Report 189597,Contract NAS1-19000.

[19] Pastore, C.M. and F.K.Ko. 1990. "Modeling of textile structural composites, Part I: processing science model for three-dimension braiding," Journal of Textile Institute, 81(4): 480-490.

[20] Pastore, C.M., A.E.Bogdanovich and Y.A.Gowayed. 1993. "Application of a MESO-VOLUME-based analysis for textile composite structures," Composite Engineering, 32(4): 181-194.

[21] Hahn, H.T. and Pandy, R. 1994. "A micromechanics models for thermoelastic properties of plain weave fabric composites", Journal of Eng. Mater. Techno., 116:517-523.

[22] Vandeurzen, Ph., J. Ivens and I. Verpoest. 1996. "A critical comparison of analytical and numerical (FEM) models for the prediction of the mechanical properties of woven fabric composites", paper presented at New Textiles for Composites TEXCOMP-3, RWTH Aachen (G).

[23] Withcomb, J., J. Noh and C. Chapman. 1996. "Evaluation of various approximate analysis for plain weave composites", ASME J, 9 February.

[24] Norman, T., P. Allison, J.W. Baldwin, B.K. Gracias and D. Seesdorf. 1993. "Effect of tow alignment on the mechanical performance of 3D woven textile composites", Compos Manufacturing, 4(4): 209-215.

[25] Norman, T., C. Anglin and D. Gaskin. 1996. "Strength and damage mechanisms of notched two-dimensional triaxial braided textile composites and tape equivalent under tension", J. Compos. Technol. Res., 18(1): 38-46.

[26] Norman, T., C. Anglin, D. Gaskin and M. Patrick. 1996. "Normal stress distribution of notched 2D triaxial braided textile composites and tape equivalent under tension", J. Compos. Mater., 30(5): 589-601.

[27] Kalidindi, S.R. and A. Abusafieh. 1996. "Longitudinal and transverse moduli and strengths of low angle 3-D braided composites", Journal of Composite Materials, 30(8): 885-905.

[28] Kalidindi, S.R. and E. Franco. 1997. "Numerical evaluation od isostrain and weighted-average models for elastic moduli of three-dimensional composites", Compos. Sci. Technol., 57: 293-305.

[29] Pastore, C.M. and Y.A. Gowayed. 1994. "A self consistent fabric geometric model: modification and application of a fabric geometry model to predict the elastic properties of textile composites", J. Compos. Technol. Res., 16(1): 32-36.

[30] Gowayed, Y.A. and R. Vaidyanathan. 1996. "Optimization of elastic properties in the design of textile composites", Polym. Compos., 17(3): 1-7.

[31] Gowayed, Y.A. and J.C. Hwang. 1995. "Thermal conductivity of composite materials made from plain weave and 3-D weave", Compos. Eng., 5(9): 1177-1186.

[32] Bogdanovich, A.E. 1992. "On the structural analysis of textile composites", Topics in Composites structures, AD Vol. 26/AMD: 133-139.

[33] Pastore C.M., J.E. Masters, R.L. Foye and Y.E. Gowayed. 1993. "Mechanical properties of triaxially braided composites: experimental and analytical results", J. Compos. Mater. Res., 15(2): 112-122.

[34] Pastore C.M., Y.E. Gowayed and C. Howarth. 1996. "Modification and application of a unit cell continuun model to predict the elastic properties of textile composites", Composites Part a, 27: 149-155.

[35] Gowayed, Y.E. The graphite integrated numerical analysis (GINA). Workshop, 1997.

[36] Gowayed, Y.E. The effect of voids on the elastic properties of textile reinforced composites. Workshop, 1997.

[37] Gowayed, Y. J.C. Hwang and D. Chapman. 1995. "Thermo-conductivity of textile composites with arbitrary perform structures", J. Compos. Technol. Res., 17(1):56-62.

[38] Pastore C.M., A..E. Bogdanovich and A.B. Birger. 1992. "Analysis of composite shallow shell structures reinforced with textiles", Textile Composites in Building Construction Part 2: 35-44.

[39] Bogdanovich, A.E. 1993. "Three-dimensional analysis of anisotropic spatially reinforced structures", Compos. Manufacturing, 4(4):173-186.

[40] Pastore, C.M., A.E. Bogdanovich and A.B. Birger. A.E. 1993. "Three dimensional deformation and failure analysis of textile reinforced structures", Compos. Design, ICCM/9: 495-501.

[41] Pastore, C.M. and A.E. Bogdanovich. 1996. "Material smart analysis of textile reinforced structures", Compos. Sci. Technol., 56: 291-309.

[42] Withcomb, J., K. Woo and S. Gundapaneni. 1994. "Macro finite element for analysis of textile composites", J. Compos. Mater., 28(7): 607-608.

[43] Withcomb, J. and K. Woo. 1994. "Global/local finite element analysis for textile composites", J. Compos. Mater., 28(14): 1305-1321.

[44] Withcomb, J. and K. Woo. 1994. "Enhanced direct stiffness method for finite element analysis of textile composites", Compos. Struct., 28: 385-390.

[45] Withcomb, J., K. Woo and G. Kondagunta. 1995. "Boundary effect in woven composites", J. Compos. Mater., 29(4): 507-524.

[46] Withcomb, J., and C. Chapman. 1995. "Effect of assumed tow architecture on predicated moduli and stress in plain weave composites", J. Compos. Mater., 29(16): 2139-2159.

[47] Withcomb, J., C. Chapman and K. Srirengan. 1995. "Evaluation of homogenization for global/local stress analysis of textile composites", Compos. Struct., 31: 137-149.

[48] Withcomb, J. and K. Woo. 1996. "Three dimensional failure analysis of plain weave textile composites using a global/local finite element method", J. Compos. Mater., 30(9): 985-1003.

[49] Withcomb, J. and K. Srirengan. 1996. "Effect of various approximation on predicted progressive failure in plain weave composites", Compos. Struct., 34: 13-20.

[50] Paumelle, P., A. Hassim and F. Lene. 1990. "Composites with woven reinforcements: calculation and parametric analysis of the properties of the homogeneous equivalent", La recherché aerospatiale, 1: 1-12.

[51] Paumelle, P., A. Hassim and F. Lene. 1990. "Microstress analysis in woven composite structures", La recherché aerospatiale, 6: 47-62.

[52] Wood, J. 1994. "Finite element analysis of composite structures", Composite Structures, 29: 219-230.

[53] Hewitt, J.A., Brown, D. and Clarke, R.B. 1995. "Computer modeling of woven composite materials", Composites, 26: 134-140.

[54] Blackketter, D. M., D.E. Walrath and A.C.Hansen. 1993. "Modeling damage in a plain weave fabric reinforced composite material", Journal of Composites Technol. Res., 15(2): 136-142.

[55] Prodomou A., Vandeurzen Ph., Huysmans G., Ivens J. and Verpoest I. "Micromechanical modelling of textile composites using variational principles", Proc. Computer Methods in Composite Materials VI, eds. Hoa S.V., DeWilde W.P. and Blain W.R., Computational Mechanics Publications, WIT, 1998..

[56] Fujita, A., Z. Maekawa, H. Hamada and A. Yokoama. 1992. "Mechanical behavior and fracture mechanism in flat braided composites Part 1: Braided flat bar", J. Reinforced Plastics Compos., 11:600-617.

[57] Fujita, A., H. Hamada and Z. Maekawa. 1993. "Tensile Properties of Carbon Fiber Triaxial Woven Fabric Composites," Journal of Composite Materials, 27:1428-1442.

[58] Dano, M.L., G.Gendron and A.Picard. "Elastic properties of a carbon fiber triaxial woven fabric composite," Proceedings of the Canadian Conference of Applied Mechanics, Toronto, May 1999.

[59] Hoa, S.V. and S.Z.Sheng. "Three dimensional model for elastic properties of textile composites", Proc. 3rd Canadian International Conf. on Composites, Montreal, August 2001, published by Technomic.

[60] Sheng, S. Z. and S.V.Hoa. "Modelling of triaxial woven fabric composites", Proc. 2nd Taiwan Canada workshop on Aeronautics, Kaohsiung, Taiwan, May 2001.

[61] Yong, Y. and S.V.Hoa. "Energy approach for prediction of mechanical behavior of 2-D triaxially braided composites, Part I: Model development" J. of Composite Mateials, Vol. 36, No. 8, 2002, pp. 963-982.

[62] Yong Yan and S.V. Hoa. "Energy approach for prediction of mechanical behavior of 2-D triaxially braided composites, Part II: Parameter Analysis", J. of Composite Materials, Vol. 36, No. 10, 2002, pp. 1233-1254.

[63] Xu, D, R.Ganesan and S.V.Hoa. "Buckling analysis of triaxial woven fabric composite structures. Part I: nonlinear finite element formulation", Submitted, J. of Composite Structures.

[64] Robbins, D.H. and J.N. Reddy. 1993. "Modeling of thick composites using a layerwise laminate theory," Int. J. Numer. Methods Eng., 36:655-677.

[65] Reddy, J.N. 1987. "A generalization of two-dimensional theories of laminated composite plates," Communications in Applied Numerical Methods, 3:173-180.

[66] Reddy, J.N. 1989. "On the generalization of displacement-based laminate theories", Appl. Mech. Rev., 42(11) Part 2: 213-222.

[67] Reddy, J.N. 1989. "Generalization of two dimensional theories of laminated composite plates", Appl. Numer. Meth., 3: 173-180.

[68] Barbero, E.J. and J.N. Reddy. 1990. "An accurate determination of stresses in thick laminates using A generalized plate theory", Int. J. Numer. Methods Eng., 29: 1-14.

[69] Reddy, J.N., E.J. Barbero and J. Teply. 1989. "A plate bending element based on a generalized plate theory", Int. J. Numer. Methods Eng., 28: 2275-2292.

[70] Reddy, J.N., C.S. Krishnamoorthy and K.N. Seetharamu. 1988. Lecture Notes in Engineering (37): Finite element analysis for engineering design, Springer-Verlag Berlin Heidelberg New York.

[71] Cook, R.D., D.S. Malkus and M.E. Plesha. Concepts and applications of finite element analysis, (Third Edition), John Wiley & Sons, New York.

[72] Ouellette, P. and S.V. Hoa. 2001. CONCOM-EMS-3, Concordia University.

[73] Hyer, M. W. 1997. Stress analysis of fiber-reinforced composite materials, WCB/McGraw-Hill, New York.

[74] ART EM reflector, Part No. 832246-101, EMS internal report.

[75] Takano N., K. Terada, M.Zako and T. Yoshioka. "Microstructural analysis of three-dimensional permeability of textile composites by the homogenization theory", Proceedings of the Third Canada-Japan Workshop on Composites, Kyoto, Japan, March 2000, p381-386.

[76] Hoa S.V., Sheng S.Z. and Ouellette P. "Determination of elastic properties of triax composite materials", Journal of Composites Science and Technology, in press.

[77] Roark R.J. and Young W.C. Formulas for stress and strain, 5th edition, McGraw Hill, 1975.

[78] Singh, S.B., Kumar, A. and Iyengar, N.G.R. 1997. Progressive failure of symmetrically laminated plates under uni-axial compression, Structural Engineering and Mechanics, 5(4): 433-450

[79] Singh, S.B., A. Kumar and N.G.R. Iyengar. 1998. "Progressive failure of symmetric laminates under in-plane shear: I-positive shear", Structural Engineering and Mechanics, 6(2): 143-159.

[80] Blackketter, D. M., Walrath, D. E., and Hansen, A. C. (1993). "Modeling damage in a plain weave fabric-reinforced composite material", Journal of Composites Technology and Research, 15(2): 136-142.

[81] Dasgupta A. and Bhandarkar S. M. 1994. "Effective thermo-mechanical behavior of plain-weave fabric reinforced composites using homogenization theory", *Journal of Engineering Materials and Technology*, Transactions of the ASME, 116: 99-105.

[82] Makoto, I. and Chou, T. W. 1998. "An analytical and experimental study of strength and failure behavior of plain weave composites", *Journal of Composite Materials*, 32(1): 2-30.

[83] Naik, A. R. 1994. "Failure analysis of woven and braided fabric reinforced composites", NASACR-194981, NASA, Hampton, Virginia.

[84] Tsai, S.W. 1984. "A survey of macroscopic failure criteria for composite materials", Journal of Reinforced plastics and composites, 3: 40-62.

[85] Hoffman, O. 1967. "The brittle strength of orthotropic materials", Journal of Composite materials, 1: 200-211.

[86] Tsai, S.W. and Wu, E.M. 1971. "A general theory of strength for anisotropic materials", Journal of Composite materials, 5: 58-80.

[87] Engelstad, S.P., J.N. Reddy and N.F. Knight Jr. 1992. "Post-buckling response and failure prediction of graphite epoxy plates loaded in compression", AIAA Journal, 30: 2106-2113.

[88] Zhao Q. and S.V. Hoa. 2003. "Triaxial Woven Fabric (TWF) composites with open holes (Part I): Finite element models for analysis", Journal of Composite Materials, 37(9): 763-789.

[89] Zhao Q., S.V. Hoa and P. Ouellette. 2003. "Triaxial Woven Fabric (TWF) composites with open holes (Part II): Verification of the finite element models", Journal of Composite Materials, 37(10): 849-874.

[90] Zhao Q., S.V. Hoa and R. Moudrik. "Finite element modeling of a membrane sector of an art em reflector", accepted, Journal of Composite Materials, November 2002.

[91] Zhao Q. and S.V. Hoa. "Thermal deformation behavior of Triaxial Woven Fabric (TWF) composites with open holes", accepted, Journal of Composite Materials, March 2003.

[92] Zhao Q., S.V. Hoa and P. Ouellette. "Progressive failure of Triaxial Woven Fabric (TWF) composites with open holes", submitted, Journal of Composite Structures, September 2003.

[93] Zhao Q. and S.V. Hoa. "Thermal Deformation Behavior of Triaxial Woven Fabric (TWF) Composites with Open Holes", The Fourth Canadian-International Composites Conference (CANCOM 2003), Ottawa, Canada, August19-22, 2003.

[94] S.V. Hoa, Q. Zhao & P. Ouellette. "Analysis of triax composites for satellite applications", 34th International SAMPE Technical Conference, Long Beach, CA, May 11-15, 2003.

[95] S.V. Hoa, Q. Zhao and P. Ouellette, "Mechanical behavior of triax composites using special finite elements", American Society for Composites (ASC) 17th Annual Technical Conference, Purdue University, West Lafayette, Indiana, October 21-23, 2002.

[96] Zhao Q., S.V. Hoa, P. Ouellette and R. Moudrik. "Finite element modeling of a triax composite membrane sector", Canada-Japan Workshops on Composites, Vancouver, September 19, 2002.

[97] S.V. Hoa, Q. Zhao, P. Ouellette and R. Moudrik. "Application of triax composites in satellite", International Conference in Aerospace Sciences (ICAS), Ottawa, May 2002.

[98] S.V. Hoa, Q. Zhao, P. Ouellette and R. Moudrik. "Behavior of triax composites for satellite applications", 3rd Annual Aerospace Industries Association of Canada (AIAC) Aerospace Technology Collaboration Forum, Montreal, 1-2 May 2002.

[99] S.V. Hoa, S.Z. Sheng, Q. Zhao and P. Ouellette. "Determination of elastic properties of triax composite materials", International Conference on Materials for Advanced Technologies, Singapore, June 2001.